IMAGE PROCESSING FOR STRATOSPHERIC BASED SPACE SITUATIONAL AWARENESS (SSA)

VITHURSHAN SUTHAKAR

A THESIS SUBMITTED TO
THE FACULTY OF GRADUATE STUDIES
IN PARTIAL FULFILLMENT OF THE REQUIREMENTS
FOR THE DEGREE OF MASTER OF SCIENCE

GRADUATE PROGRAM IN EARTH AND SPACE SCIENCE
YORK UNIVERSITY
TORONTO, ONTARIO

November 2024

Abstract

This research explores the use of a stratospheric platform imager for advancing Space Situational Awareness (SSA). The primary goal was to develop and validate Resident Space Objects (RSO) detection algorithms using the RSONAR dataset, consisting of wide field-of-view imagery. RSO Detection methods were tested on 429 images, achieving F1 scores between 68% and 88%. Additionally, the potential of a dual-purpose star tracker for SSA was validated, analyzing over 27,000 images to assess astrometric and photometric properties of RSOs. Further, 544 RSO streaks were characterized based on parameters such as length, signal-to-noise ratio, and orientation. The development of RSONAR II, a next-generation camera system, allowed for capturing over 65,000 images at varying resolutions, and its optical performance was compared across two imaging systems. This study provides a comprehensive evaluation of wide field-of-view imagery for SSA and presents advancements in dual-purpose star tracker systems for future missions.

Acknowledgment

I want to thank my supervisor, Dr. Regina S.K. Lee. I will forever be deeply indebted to her for her guidance and commitment to my personal and academic growth over the past few years. She has always provided me with countless opportunities, allowing me to learn at my own pace. I will be forever grateful for her support and look forward to the upcoming years. I want to thank my committee member, Dr. Franz Newland. His space pilot program was a pivotal point in my life, rejuvenating my interest in space as a whole.

I would like to extend my gratitude to Dr. Siddharth Dave and soon-to-be Dr. Akash Chauhan for being amazing mentors and allowing me to pick their brains on various aspects of life. I would like to thank the RPG, Randa (Ben 10 fanatic), Perushan (Lab's Sage), and Gabe (Mall Santa). Timmins would have been just potholes without your presence. I would also like to thank all my lab mates, Aiden, Andrea, David, Emilee, Ian, Luca, Marissa, Michael, Mishal, Tom and Vidhushi. I would like to thank my friends, Jimmy (a classmate from Ms.Mac), Aaranan (Alden), and Pruthvi (Mars lover), for listening to my crazy ideas and sharing theirs. I want to thank my parents who have dedicated their entire lives to providing support for me and my siblings. I wouldn't be who I am today without their daily presence. Thank you for being my anchor and keeping me grounded. I also want to thank my siblings and my cousin for being my biggest cheerleaders and providing emotional support in times of need. Lastly, I want to thank my partner for constantly pushing me to improve daily.

Contents

List of Tables

List of Figures

List of Abbreviations

Abbreviation	Description
AD	Attitude Determination
ADU	Analog Digital Unit
AFD	Adjacent Frame Differencing
ARO	Australia Remote Observatory
ASTRiDE	Automated Streak Detection for Astronomical Images
BOPPS	Balloon Observation Platform for Planetary Science
BRRISON	Balloon Rapid Response for ISON
BT	Blue Tycho Magnitude
CASSIOPE	Cascade, Smallsat and Ionospheric Polar Explorer
CCTV	Closed-Circuit Television
CNNs	Convolutional Neural Networks
CNES	Centre National d'Etudes Spatiales
CSA	Canadian Space Agency
Dec	Declination
DRDC	Defence Research and Development Canada
ECI	Earth-Centered Inertial
ESA	European Space Agency
ESBO	European Stratospheric Balloon Observatory
FAI	Fast Auroral Imager
FNs	False Negatives
FPGA	Field Programmable Gate Arrays
FPs	False Positives
FOV	Field of View

Abbreviation	Description
FOVs	Fields of View
FWHM	Full Width Half Maximum
GHAPS	Gondola for High Altitude Planetary Science
GEO	Geosynchronous Equatorial Orbit
IOD	Initial Orbit Determination
ISON	International Scientific Optical Network
IQR	Interquartile Range
LEO	Low Earth Orbit
LiDAR	Light Detection and Ranging
LM	Levenberg-Marquardt
LPSIS	Learned Perceptual Image Patch Similarity
MASTER	Meteoroid and Space Debris Terrestrial Environment Reference
MEO	Medium Earth Orbit
MFD	Median Frame Differencing
MSE	Mean Squared Error
PDU	Power Distribution Unit
PFT	Proximity Filtering and Tracking
PSNR	Peak Signal-to-Noise Ratio
RADAR	Radio Detection and Ranging
RA	Right Ascension
RBs	Rocket Bodies
RHR	Right-Hand Rule
ROI	Region of Interest
RSONAR	Resident Space Object Near-Space Astrometric Research

Abbreviation	Description
RSONAR II	Resident Space Object Near Space Astrometric Research II
SBR	Signal-to-Background Ratio
SBSS	Space-Based Space Surveillance
SD	Streak Detection
SDGs	Sustainable Development Goals
SCMOS	Scientific Complementary Metal-Oxide Semiconductor
SH	Secure Shell
SNR	Signal to Noise Ratio
SPP	Stabilized Pointing Period
SSH	Secure Shell
SST	Space Surveillance and Tracking
SSIM	Structural Similarity Index Metric
SSM	Star-Stare Mode
STARDUST	Star Tracker Attitude and RSO Detection for Unified Space Technologies
STARE	Space-Based Telescopes for Actionable Refinement of Ephemeris
STs	Star Trackers
TRM	Track Rate Mode
TLE	Two Line Elements
TPs	True Positives
UBV	Ultraviolet, Blue, Visual
UHS	Ultra-High Speed
UNOOSA	United Nations Office for Outer Space Affairs
USD	United States Dollar

Abbreviation	**Description**
VT	Visual Tycho Magnitude
WCS	World Coordinate System
WFOV	Wide Field-Of-View

1 Introduction

1.1 Problem Statement

Since the launch of Sputnik 1, the first artificial satellite, in October 1957, space has become a domain for nations to demonstrate their technological prowess. This competition, famously embodied in the Space Race between the United States and the Soviet Union, drove nations to make rapid advancements in satellite design, exploration of Earth's neighboring celestial bodies, and ultimately human spaceflight, culminating in the moon landing.

Amid this competition, other countries, including Canada, have also made significant contributions. Canada became the third country in the world to operate a satellite with the launch of Alouette 1 in 1962, designed to study the ionosphere. Over time, satellites have played a pivotal role in social and sustainable developments worldwide. They provide navigation, communication, and networking services and monitor vegetation and natural disasters. For example, Earth observation satellites like the RADARSAT Constellation Mission monitor ice and water quality in northern Canada, providing crucial advisories for remote communities. Moreover, satellites have even contributed to fields such as medication production in orbit, which has shown advantages over Earth-based production [2]. In numerous ways, satellites have supported the 17 Sustainable Development Goals (SDGs), improving human life and sustainability on a global scale.

However, space has also become increasingly congested and contested. As of August 2024, nearly 19,000 satellites have been launched since Sputnik 1, with around 13,000 satellites still in orbit, of which only 10,000 are functional [3]. The miniaturization and commercialization of satellite design have revolutionized the space industry. Modern MicroSats and Cubesats can perform science and technological functions at a fraction of the cost and size of their predecessor. Launch providers namely, SpaceX and Rocket Labs have drastically reduced launch costs. According [4, 5], SpaceX alone was responsible for 86% of all satellite launches up to September 2024, with 48% of those launches being its Starlink satellites. The year 2024 is expected to set a new global record for

successful orbital launches, continuing the trend of record-setting years. Companies like Starlink, OneWeb, Telesat and Project Kuiper are committed to launching mega-constellations, and the QianFan (the G60 project), which aims to launch 13,904 satellites by 2030 [6].

The objects in Earth's near space, collectively referred to as Resident Space Objects (RSOs), are not limited to functional satellites. They include rocket bodies (RBs) from initial deployments, components from deteriorating satellites, debris from accidental collisions, and defunct satellites. RBs, in particular, can remain in orbit for decades before deorbiting. In 2022, nearly 500 RBs, each weighing around 2,000 kg, were left abandoned in Low Earth Orbit (LEO) [7]. The LEO altitude range of 800–900 km is particularly crowded with RBs, posing a high risk of future fragmentation events due to their sheer mass and size.

The first recorded fragmentation event occurred in 1961 when an RB exploded, creating a debris cloud [8]. In 1996, the Pegasus vehicle's upper stage exploded, resulting in 753 RSOs due to an over-pressurized propellant tank [9]. On January 11, 2007, the destruction of the Fengyun 1C satellite during an anti-satellite missile (ASAT) test generated 3,431 RSOs, with 2,809 still in orbit today [10]. A major unintentional collision occurred on February 10, 2009, when the Iridium 33 and Cosmos-2251 satellites collided, producing 2,294 RSOs in near-Earth space, 1,396 of which remain in orbit [10]. In 2015, the decommissioned NOAA 16 satellite fragmented, releasing 458 RSOs [10]. Another significant ASAT test occurred in 2021 with the destruction of COSMOS-1408, creating 560 debris fragments, which posed a threat to astronauts aboard the International Space Station (ISS)[11]. More recently, on August 6, 2024, an RB associated with the Qianfan satellite launch fragmented, producing over 300 RSOs. On September 6, 2024, over 40 additional RSOs were identified following the breakup of an ATLAS 5 Centaur RB, these numbers are expected to increase with more observations. Notably, ATLAS 5 Centaur RB model has been already part of three fragmentation events [12].

Historically, the space industry operated on the "Big Sky" mentality, assuming that the vastness of space, compared to the relatively small amount of debris, would minimize the likelihood of collisions. However, the exponential increase in satellites and debris fragments has made this as-

sumption obsolete. The number of RSOs has increased significantly in recent years, as shown in Figure 1 [1]. This rising population of RSOs heightens the risk of triggering the Kessler Syndrome—a scenario in which collisions between space objects lead to cascading collisions, further cluttering near-Earth space. Figure 2 illustrates the long-term evolution of objects in LEO based on simulated scenarios [1]. Even in a hypothetical scenario with no further satellite launches, the number of objects in space is still projected to increase, indicating that the Kessler Syndrome may already be in effect. Consequently, the growing number of RSOs underscores the urgent need for comprehensive tracking, identification, and cataloging of all objects in space, known as space situational awareness (SSA), which plays a crucial role in preventing collisions and safeguarding the longevity of space missions from premature termination.

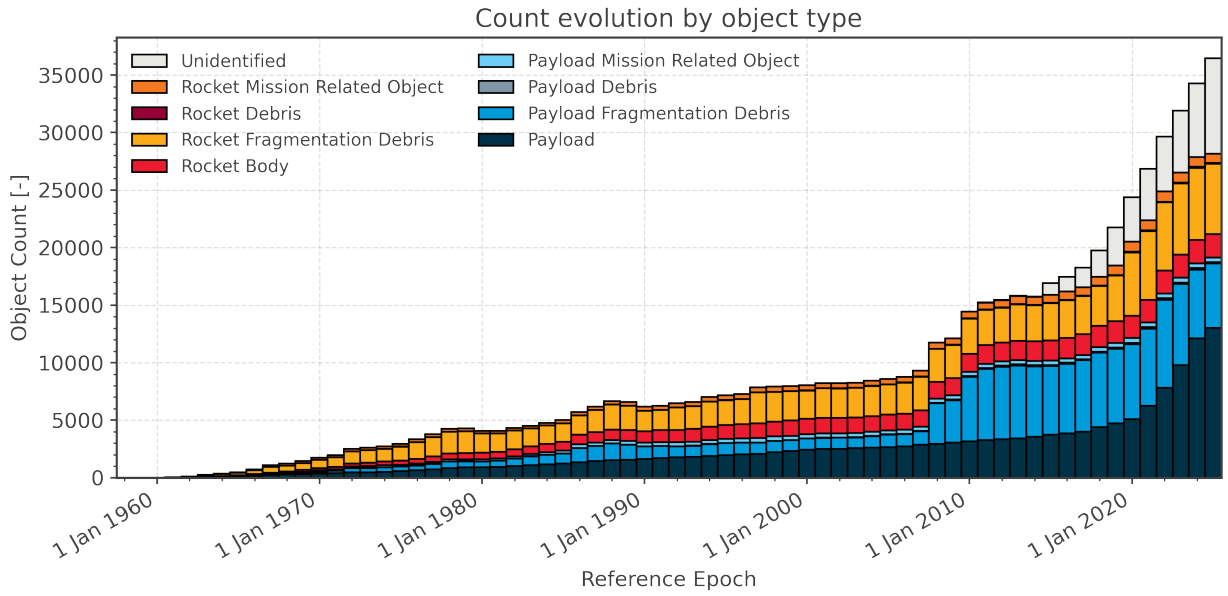

Figure 1: Count Evolution by Object Type [1]

Several organizations actively monitor and catalog RSOs using a global network of Radio Detection and Ranging (RADAR), Light Detection and Ranging (LiDAR), and optical sensor stations. For instance, the European Space Agency's (ESA) Space Surveillance and Tracking (SST) system provides conjunction assessments to avoid potential collisions, monitors fragmentation events, and predicts the re-entry trajectories of RSOs. The International Scientific Optical Network (ISON) focuses on tracking RSOs in Geostationary Orbits (GEO), while the U.S. Space Surveillance Net-

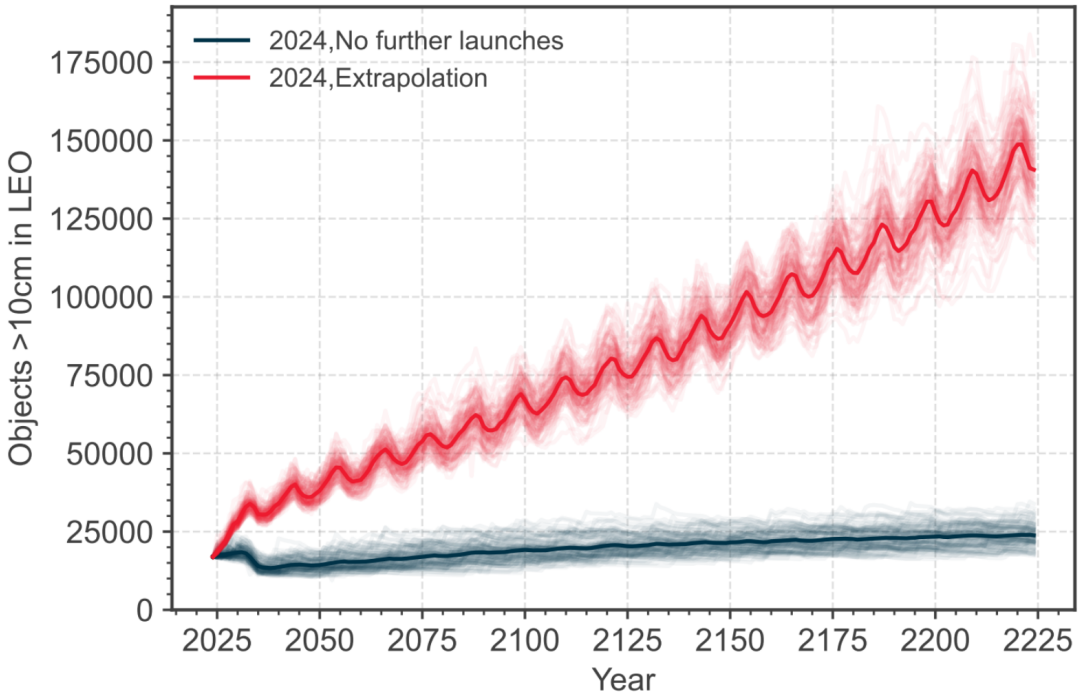

Figure 2: Projection of objects larger than 10 cm in LEO (2024 Extrapolation vs. No Further Launches) [1]

work (SSN) maintains a catalog of 36,500 debris fragments larger than 10 cm. However, there remains a significant observational gap for RSOs in the 1 cm to 1 m range.

Hence, modelling tools like ESA's MASTER (Meteoroid and Space Debris Terrestrial Environment Reference) are employed to estimate the number of smaller debris objects [13]. According to MASTER, approximately 131 billion objects between 1 mm and 10 cm in size exist in Earth's orbital environment. Even debris as small as 1 cm poses a serious threat to spacecraft, as demonstrated by the Sentinel-1A anomaly on August 23, 2016, when a collision with debris impacted the satellite's orientation and orbit [14].

The overcrowding of RSOs also poses a cultural threat. For example, the indigenous Australian constellation Emu, plays a significant role in the timekeeping and cultural practices of the Gamilaraay and Wiradjuri peoples of New South Wales, which is now being overshadowed by bright RSOs [15]. The intrusion of RSOs into the night sky are threatening traditional practices worldwide. The sheer number of RSOs is also interfering with astronomical observations affecting dark skies. According to [16], artificial light from RSOs has increased brightness in the sky by 10%,

well beyond the tolerable threshold for scientific observations.

The focus of this thesis is on utilizing novel datasets for SSA from stratospheric platforms. The optical dataset presented here will be made publicly available to support future research. The SSA processing pipeline, as shown in Figure 3, involves several key steps: data acquisition, detection, transformation, and cataloging. This thesis examines Resident Space Objects (RSOs) within the dataset, both as objects and streaks. Various algorithms capable of distinguishing RSOs within the dataset will be developed and validated. Additionally, the spatial locations of RSOs are transformed into celestial coordinates to aid in RSO identification and cataloging.

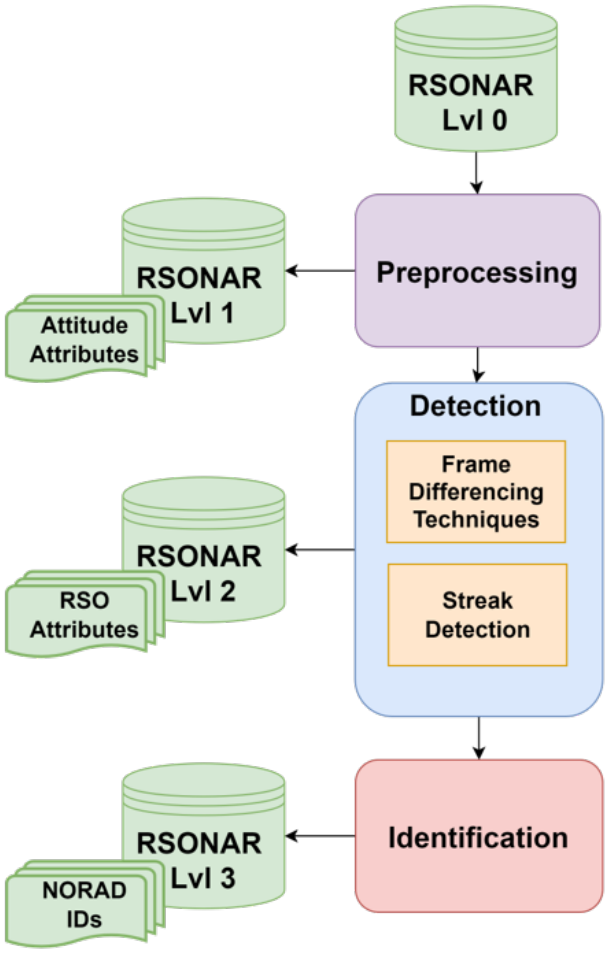

Figure 3: Resident Space Objects (RSOs), including both objects and streaks, and culminates in the correlation of these detections with an existing RSO catalog. RSONAR Lvl 0 collects raw data, while Lvl 1 refines it and identifies celestial sources. Lvl 2 extracts pixel and celestial coordinates for detected RSOs. Finally, Lvl 3 matches the detected RSOs with the catalog to assign NORAD IDs, completing the identification process.

The United Nations Office for Outer Space Affairs (UNOOSA) has outlined guidelines for long-term space sustainability [17]. In alignment with these guidelines, this dissertation also addresses several key aspects, including:

- Improving the accuracy of orbital data and enhancing information sharing,
- Promoting the sharing of space debris monitoring data,
- Sharing experiences and developing new procedures for information exchange,
- Raising awareness of space activities,
- Supporting research and development for sustainable space exploration, including measures to manage space debris in the long term.

1.2 Thesis Objectives

The primary objective of this research is to assess the effectiveness of the SSA dataset acquired from a stratospheric platform imager (RSONAR). This dataset aims to address limitations in the availability of SSA data and establish a baseline for future development and validation efforts.
The specific objectives of this study are as follows:

- **SSA Detection Algorithm Development:** To develop and validate detection algorithms using the RSONAR dataset, with potential applications in real-time onboard SSA platforms. The methods and outcomes of this objective are detailed in Chapter 2.
- **Dual-Purpose Star Tracker Validation:** To validate the concept of using a dual-purpose star tracker for SSA by extracting payload attitude and detecting Resident Space Objects (RSOs) within the RSONAR images. This approach leverages the wide field of view of star trackers, commonly found on satellites, to potentially establish a network of SSA sensors in space without relying on expensive, dedicated systems. Detailed findings are presented in Chapter 3.

- **Performance Quantification of the Star Tracker:** To evaluate the performance of a low-cost, commercial off-the-shelf dual-purpose star tracker in both attitude determination and RSO imaging. This involves photometric and astrometric assessments, focusing on metrics such as Full Width Half Maximum (FWHM), Signal to Noise Ratio (SNR), and the use of Astrometry.net for celestial transformations of stars and RSOs. Chapter 3 covers these evaluations in detail.

- **RSO Characterization:** To analyze and characterize RSO streaks within the RSONAR dataset, enhancing RSO identification and contributing to the development and validation of SSA algorithms. This analysis is presented in Chapter 4.

- **Implementation of Enhanced Image Acquisition:** To improve the image acquisition system for subsequent stratospheric flights, informed by findings from the RSONAR dataset. This enhancement, discussed in Chapter 5, allowing to further assess the feasibility of using stratospheric flights as an intermediate platform between ground-based and space-based SSA systems.

Each research objective has been meticulously examined and published in peer-reviewed papers, with results detailed in the corresponding chapters. Notes on copyright and contributions are provided at the beginning of each chapter for reference.

1.3 Contributions

This thesis makes significant contributions to advancing SSA) through the analysis and development of imaging and detection techniques for RSOs. The main contributions are summarized as follows:

- Conducted comprehensive analysis and annotation of the RSONAR dataset, providing new insights into RSO detection and characterization, including the identification of over 500 unique RSOs.

- Developed robust RSO streak detection methods, benchmarked against existing algorithms, which will aid in future SSA algorithm development.
- Contributed an extensive ground truth dataset of RSO streaks and object annotations, which will be made publicly available to support the SSA community.
- Designed and validated an advanced imaging acquisition system for the RSONAR II mission, optimizing imaging and streak detection capabilities for future missions.

The following publications and presentations have been produced as part of this research: *Comparative Analysis of Resident Space Object (RSO) Detection Methods* was published in *Sensors* (MDPI, 2023), and is available at `https://doi.org/10.3390/s23249668`. Additionally, *Stratospheric Balloon-Based Observation of Resident Space Objects for Enhanced Space Situational Awareness* was presented at the Canadian Aeronautics and Space Institute (CASI) ASTRO conference in 2024.

1.4 Thesis Outline

Chapter 1 provides an overview of the increasing challenges posed by Resident Space Objects (RSOs), emphasizing the need for Space Situational Awareness (SSA). Chapter 2 compares four RSO detection techniques—Adjacent Frame Differencing (AFD), Median Frame Differencing (MFD), Proximity Filtering and Tracking (PFT), and Streak Detection—using 429 images from the RSONAR mission, highlighting the strengths of each method. Chapter 3 validates the concept of a dual-purpose Star Tracker for SSA, evaluating the performance of a low-cost commercial Star Tracker (RSONAR) for both attitude determination and RSO imaging using 27,027 images. Chapter 4 analyzes 544 RSO streaks identified in 6,939 images from the RSONAR dataset, detailing the streak annotation process, characterizing the streaks, and comparing the performance of a newly developed streak detection method with an established open-source alternative. Chapter 5 introduces the 2023 Resident Space Object Near-space Astrometric Research II (RSONAR II) mission, showcasing advancements in dual-purpose star trackers on a CubeSat-inspired platform and comparing the

performance of two imaging systems.

2 Comparative Analysis of Resident Space Object (RSO) Detection Methods

This chapter is based on 2023 paper titled, "Comparative Analysis of Resident Space Object (RSO) Detection Method" [18] that addresses the challenges and methods for detecting Resident Space Objects (RSOs). The study utilizes an internally curated dataset from the RSONAR mission, a stratospheric balloon-based platform that captured images for RSO detection. The dataset was then manually annotated to create a benchmark for the evaluation of detection algorithms.This chapter presents a comparative analysis of four RSO detection methods: The methods under consideration are: Adjacent Frame Differencing (AFD), Median Frame Differencing (MFD), Proximity Filtering and Tracking (PFT), and Streak Detection. AFD detects RSO movement by subtracting adjacent frames, identifying RSOs as moving objects. MFD improves RSO detection accuracy by using the median of multiple frames subtracted from the current frame. PFT tracks objects across frames, filtering out static objects such as stars. The Streak Detection method identifies RSO streaks from stacked short-exposure images. Among the methods, PFT demonstrated the most optimal performance overall, offering an effective balance between precision and recall. While the Streak Detection method demonstrated satisfactory accuracy, its efficacy was diminished when applied to faint RSOs. The algorithms achieved precision scores ranging from 73% to 100%, with F1 scores between 68% and 82%. These results provide a comprehensive comparison of non-AI-based RSO detection techniques, indicating that proximity filtering and tracking are the most suitable for real-time onboard processing.

I developed and validated the Streak Detection algorithm presented in this chapter and selected the image sequences for analysis based on their complexity after a thorough examination of the RSONAR dataset. I also performed the preprocessing of the RSONAR dataset and implemented the evaluation metrics—such as precision, recall, and F1 scores—to ensure a fair comparison of the detection methods. Aiden Alexander Sanvido developed and validated the frame differencing techniques (AFD, MFD, PFT) under my supervision. He drafted the initial versions of sections

2.3.1, 2.3.2, 2.3.3, and 2.5.2. I prepared all figures and tables in this chapter, except those produced by Aiden (Figures 7, 9, and 11, and Table 4), which I further modified based on the reviewers' comments. I wrote the majority of the chapter's content and revised the sections on frame differencing techniques before publication. Randa Qashoa provided feedback on this study, leveraging her expertise in SSA. Regina Lee supervised the project and contributed her expertise in SSA. All co-authors contributed feedback and revisions to the manuscript.

2.1 Introduction

Space situational awareness (SSA) has been a growing concern around the world, as space is being reevaluated as a domain that needs protection to sustain a nation's sovereignty and monitor its assets in space. The number of resident space objects (RSOs) has remarkably increased in recent years. This occurrence is related to the Kessler Syndrome, which describes the probability of a collision between RSOs cascading into further collisions. Due to the substantial surge in satellite launches and trends towards mega-constellations, there are now numerous manufactured elements orbiting in near-Earth space. Among these objects are fragments of detonated bolts from separated upper stages of rockets, as well as entire satellites without an end-of-life plan.

In the past, the space industry operated on the "Big Sky" mentality, which presupposes that the volume of space—compared to debris fragments—is so vast that it is unlikely two objects will ever collide. However, the Department of Defense's global Space Surveillance Network (SSN) sensors currently track 34,810 debris fragments [3]. Furthermore, the European Space Agency (ESA) estimated that there were 640 past collisions and fragmentation events [3]. Therefore, it is crucial to further develop SSA to prevent collisions involving hypervelocity objects such as rocket bodies, which can lead to debris clouds that endanger the near-Earth ecosystem.

With the sudden and rapid increase in RSOs, there has also been a substantial push to advance SSA technologies in recent years. Much effort has been made for the development and demonstration of sensor technologies ranging from optical imagers with various wavelengths to technologies such as light detection and ranging (LiDAR), lasers and other sensing techniques.

2.1.1 Overview of RSO Imaging Technologies

LiDAR and RADAR Systems

LiDAR, a remote sensing technology that employs lasers to measure distances and create detailed three-dimensional maps of objects and environments, has been crucial in tracking and monitoring RSOs. These data can be used for collision threat assessment or to provide detailed information for mitigation plans. In [19], the researchers suggested an SSA mission that utilized LiDAR technology for a low-Earth-orbit spacecraft. Additionally, References [19, 20, 21] are relevant studies that explored LiDAR in SSA. Radio detection and ranging (RADAR) has also been considered for SSA applications [22, 23, 24, 25]. Radio waves are emitted to estimate the distance, speed, and trajectory of RSOs in a similar fashion to that used with LiDAR sensors. Space-borne radar has been used to track both active satellites and inactive RSOs in a way that resembles the approach used in LiDAR systems. In [26], RADAR systems (space-borne sensors) were categorized as "active" sensors that emit energy and measure the returned signal to calculate the difference between the emitted and the returned signal. In contrast, optical sensors (including infrared and visible-range sensors) were considered "passive" sensors.

Optical Systems

Our efforts in SSA imaging primarily focus on optical imaging using both space-based and ground-based imagers—specifically, optical telescopes. In the active tracking mode, an imager moves to track an object of interest. In contrast, the passive mode involves the camera imaging a star field in its field of view without any motion being imposed on the imager itself. Traditionally, star trackers installed on satellites have imaged star fields within their fields of view in a manner similar to this imaging process to ascertain their altitude. These telescopes, whether in space or on the ground, are the primary tools for tracking and observing objects in space. They collect photometric and astrometric data by capturing reflected light from RSOs, thus aiding in object identification and characterization. Space-based optical sensors offer distinct advantages, such as uninterrupted, high-quality observations that are unaffected by Earth's atmosphere. When positioned in low Earth orbit, they provide global coverage with predictable revisit times and are immune to weather and

lighting conditions, including day/night cycles and light pollution. Recent SSA missions using optical telescopes included the Cosmos series (Russia), Tiangong Space Station (China), the Sentinel series (European Union), and the BRITE constellation [27]. Notable Canadian SSA missions, such as Sapphire and NEOSSat, which were launched in 2013, relied on passive optical payloads for imaging, detecting, and monitoring RSOs in Earth orbits. Another microsatellite space surveillance mission is currently under development and will continue using this optical approach.

Space-borne optical sensors have a critical drawback compared to their ground-based counterparts, namely, their limited field of view (FOV), making continuous monitoring of a satellite's surroundings challenging. While the costs of sensors are similar, the overall cost of satellites, operations, and launches far exceeds that of ground-based observations. These sensors are placed on satellites with strict constraints on their mass, data, power, volume, and scheduling, which complicates the achievement of continuous coverage. In contrast, ground-based optical sensors offer a low-cost, extensive, and flexible observation solution compared to space-borne sensors. However, they are limited to nighttime operation, and their effectiveness is affected by atmospheric turbulence, geographic location, and weather conditions, making them less suitable for advanced SSA missions.

2.1.2 Research Objectives

Once an RSO is imaged, regardless of the wavelength or FOV of the imager, the next step in the imaging process is to detect, identify, and characterize the RSOs. Depending on the mode of observation (passive mode vs. active tracking mode), an RSO may appear as a moving object—a dot across the FOV or a streak. Object detection and streak detection are related concepts in the context of RSO observation and imaging, but they refer to slightly distinct aspects of detecting objects in motion. Object detection involves identifying and locating objects within an observed scene. In the context of RSO observation, this refers to identifying moving objects against the background of the dark sky with stars (often seen as stationary objects relative to the RSO's movement). Streak detection, on the other hand, refers to the process of identifying streak-like patterns in images that are caused by fast-moving objects. In RSO observation, these streaks are usually caused by objects

in orbit passing through the field of view of a sensor during the time in which the image is being captured with a relatively long exposure time. Streak detection involves recognizing these trails in images and associating them with RSOs, such as satellites or space debris. Streak detection is commonly used in space surveillance to identify objects that might otherwise be too faint or fast-moving to be easily discerned. In this chapter contains object and streak detection with images taken with a short exposure time. Streaks are created by stacking multiple images instead of using long-exposure observations. Examples of images containing RSOs, taken with short and long exposure times, are shown below in Figure 4 for reference.

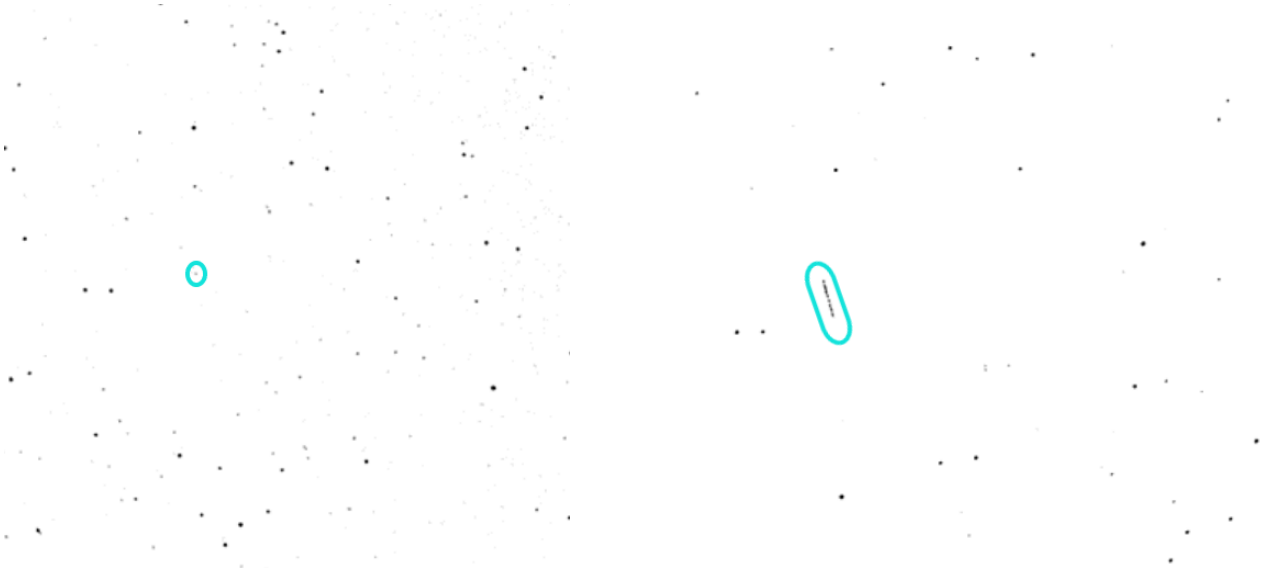

(a) (b)

Figure 4: RSO images, shown in cyan enclosement (a) Short exposure (b) Long exposure

Note that object detection and object tracking are two distinct processes that involve observing and monitoring objects in space in the context of space situational awareness (SSA). In the current chapter, object detection only focused on identifying an RSO present within optical images. Once an RSO is detected, its position and attitude within the observed scene are determined with its photometric and/or astrometric information. Based on these data, the RSO's characteristics, such as its orbit, size, shape, optical properties, and potentially its identity, are estimated. This last step is often referred to as identification and characterization. In this process, object detection is crucial for identifying new objects with the accurate and precise location of their centroids within the

frame. Object tracking, on the other hand, is the process of continuously monitoring the movement and trajectory of an RSO over time. Once an RSO has been detected and located within the FOV, the sensor is programmed to track its trajectory based on the predicted patterns of movement. Particularly, in both ground- and space-based photometric observation of an RSO for the estimation of the attitude and optical properties according to a light curve analysis, tracking is a critical step.

This chapter is dedicated to the examination of passive-mode observation techniques utilising wide-field of view (FOV) imagers with a relatively brief exposure time, with the objective of acquiring images of moving objects. It should be noted that the present study did not incorporate the aspect of tracking.

The images analyzed in this study were captured as "observations of opportunity", in which the imager was not tasked with observing planned targets. Similar examples include the study of RSO image analysis using the Fast Auroral Imager (FAI) described in [28] and the operation of dual-purpose star trackers discussed in [29, 30, 31]. Figure 5 illustrates the images captured by RSONAR and FAI, with the RSOs highlighted in red circles for reference.Further details on the mode of operation in similar scenarios can be also found [32]. In Section 2.2, we present a survey on the object detection algorithms used in SSA applications. Section 2.3 provides a detailed description of the detection algorithms that we tested and implemented in the current study, namely, adjacent frame differencing (AFD), median frame differencing (MFD), proximity filtering and tracking (PFT), and streak detection. Before the results are described in Section 2.5,the datasets used in this chapter are outlined in Section 2.4. The conclusion and future work are discussed in the final section.

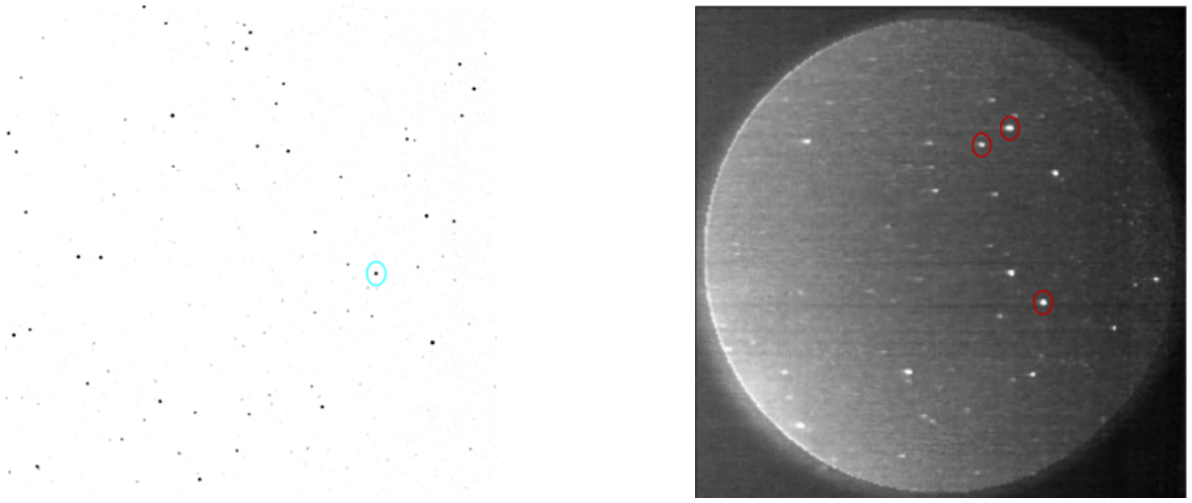

(a) (b)

Figure 5: Sample images where RSOs are visible (shown in circles); (a) RSONAR; (b) FAI.

2.2 Survey of Object Detection Algorithms in SSA Applications

Object detection methods are continuously evolving, with numerous algorithms emerging annually, making it challenging to compile an all-encompassing survey. Instead, several survey articles have provided insights into this rapidly changing field. Ragland and Tharcis [33] focused on traditional (non-AI-based) methods, including frame differencing, optical flow, and background subtraction. Meanwhile, the authors of [34] offered a comprehensive review of deep learning techniques for object detection, and they addressed datasets, assessment metrics, context modeling, and detection proposal methods. The evolution of object detection elements, from detectors to optimization techniques, from 1998 to 2021 was covered in [35]. A holistic view of deep learning systems, methods, benchmark datasets, and real-world applications can be found in [36].

Beyond detection, object tracking and streak detection are both widely studied fields in vision science, with a wide range of applications in autonomous vehicles, transportation management, and health monitoring. Several techniques have been developed and applied to these fields with varying levels of success. As AI-based techniques have been successfully implemented, they have led to the emergence of many algorithms, which are supported by readily available datasets for training and validation. However, these topics are outside the scope of the current study and will

be considered later.

The application of most of the methods described above to RSO detection has not been extensively studied, and no conclusive results are available. A recent paper by Massimi et al. offered the most comprehensive survey on the subject [37]. The authors classified methods into non-AI- and AI-based methods. Among the AI-based methods, YOLO, CNN, and other branches of deep learning were also described. Additionally, they presented preliminary results from a case study on SSA applications. The case study presented in the referenced literature primarily focused on simulated environments and radar processing. While AI-based methods, which are primarily deep-learning approaches, do show promising results, a significant technological gap persists in the implementation of these methods in real-time scenarios. Implementing AI-based object detection methods can be a complicated task that requires the integration of various technologies and for several challenges to be addressed. The primary challenge in an AI application is the collection, annotation, and validation of data to ensure their quality and quantity. Deep learning models necessitate significant volumes of high-quality labeled data for training. Acquiring, curating, and annotating such data can be expensive and time-consuming. Ensuring the precision and diversity of the training dataset is fundamental for a model's performance. In SSA applications, there are no publicly available annotated datasets for evaluating newly developed algorithms.

For RSO images, we examined various datasets composed of ground- or space-borne images of star fields that contained RSOs, such as NEOSSat images [38], FAI images from onboard CASSIOPE [39], and ground observations from various telescopes and observatories around the world [40]. However, creating accurate annotations for object detection tasks is time-consuming, challenging (given the complex nature of the images), and expensive (as it requires trained personnel who can recognize a moving object as an RSO in star field images). Secondly, defining bounding boxes or segmentation masks for objects in images also requires expertise and meticulous attention to detail. Errors in annotations can lead to biased or incorrect model predictions. Third, choosing the right object detection architecture and configuration is also difficult, and the performance relies heavily on the nature of the images with which the algorithms are trained. Dif-

ferent models have varying trade-offs between accuracy and speed. Tuning hyperparameters and architecture choices requires extensive experiments, testing, and experience. Lastly, most AI-based methods require extensive computational resources and powerful hardware such as GPUs or TPUs for training and inference. Implementing and scaling such models can be costly and can require careful resource management, making it nearly impossible to implement them onboard spacecraft in real time.

Given these difficulties with AI-based methods, the current study is intended to gain an understanding of the applicability of the popular non-AI-based detection methods specifically in SSA applications and aims to provide a baseline for future development. We also provide an annotated dataset that was collected and pre-processed from a stratospheric balloon-borne platform on which the current study was based. The accompanying dataset can be used as a training and validation set to develop AI-based methods and to improve RSO detection algorithms.

2.3 RSO Detection Methods

Detecting RSOs in star field images is a challenging task for various reasons. RSOs are smaller and less intense than stars, which largely dominate star field imaging. Consequently, RSOs appear relatively faint compared to stars, which are luminous objects. The brightness of a Resident Space Object (RSO) stems from the phase angle, which is the angle between the Sun and the observer, as measured at the RSO itself. However, the brightness of RSOs is not consistent during an observed transit. Significant differences in brightness are evident between various RSOs, such as active satellites, tumbling satellites, and rocket bodies [41]. In addition, the inherent image noise due to elements such as sensor noise and cosmic rays can also suppress the photometric value of RSOs, which further complicates detection. Especially for images acquired using ground-based systems, additional noise, such as light pollution, atmospheric effects, and changing lighting conditions, presents hindrances to the task of RSO detection due to the varying background. Furthermore, most RSOs lack distinctive features and are subject to environmental degradation in space, making it hard to differentiate between them and stars. The spatial resolution of the imaging system can

heavily influence the distinction process, although higher-resolution images are scarce. RSOs travel at varying velocities, thereby making it difficult to identify multiple RSOs that are present in a singular image sequence.

Hence, all factors must be considered in RSO detection amidst star fields to differentiate RSOs from the background stars. The detection can be made easier with preprocessing that accounts for the characteristics of the imaging system, intrinsic and extrinsic calibration, and an understanding of the orbital parameters of RSOs that are likely to be observed. While a multitude of object detection methods are reliable, efficient, and effective methods in other applications, not all of them would be sufficient for RSO images.

The optical flow method is employed to identify objects, whereby the analysis of ”motion flow fields” serves to effectively reduce the occurrence of jitter and motion artifacts in captured images [6]. However, this approach is not suitable for real-time applications due to its high computational intensity. The method is based on the assumption of constant pixel intensities and similar motion patterns among neighboring pixels, which can be a limitation for RSO detection, particularly when dealing with RSOs that exhibit changes in brightness and varying speeds relative to the background.

The Fast R-CNN approach presents both advantages and challenges in the context of object detection. In contrast to traditional convolutional networks, it is capable of adapting to a variable number of outputs due to the presence of objects entering and exiting frames, thereby facilitating the calculation of dynamic object counts. The image is partitioned into 2,000 region proposals through the implementation of a search algorithm, with the potential for these regions to encompass objects [7]. A convolutional neural network is employed to extract features from the aforementioned proposals and to perform object classification based on the features generated through contour assessment within bounding boxes. While Fast R-CNN employs a structured edge detector for this purpose, OpenCV’s contour detection can be utilized, albeit potentially at a slower rate. It is noteworthy that it demonstrates proficiency in fine-tuning feature detection, thereby facilitating object classification that extends beyond motion detection. Nevertheless, the training process requires a considerable investment of time and data, and its detection procedure is slower due to the algorithmic complex-

ity, which presents challenges for real-time applications and poses implementation challenges due to the use of a convolutional neural network for feature extraction.

We acknowledge that there is a plethora of object detection and tracking methods. It is to be noted that we intentionally excluded AI-based approaches from this comparison, as our aim was to explore detection capabilities through implicit methods, which are deemed more appropriate for our dataset. An AI-based approach for RSO detection will be explored with this dataset in future research.

In this chapter, we largely evaluated four algorithms for comparison purposes. We chose three frame differencing techniques, namely, adjacent frame differencing (AFD), median frame differencing (MFD), and proximity filtering and tracking (PFT), for object detection. We also briefly considered the optical flow and nearest neighbor methods, but based on the literature review, they were insufficient for RSO detection. Instead, we implemented streak detection with the aid of plate solving. A comparison among these detection methods is summarized in Table 2. The detection methods are fully automatic and designed for autonomous real-time processing onboard satellites. The only manual intervention occurred during the initial annotation phase of the dataset, where experts performed hand-labeling to create accurate validation data. The frame differencing methods proposed in this chapter have been extensively researched in various areas of computer vision. These methods are predominantly used for motion detection in videos from surveillance cameras (also known as CCTV (closed-circuit television)). Adjacent frame differencing is employed in enclosed environments, such as shopping complexes and theaters, where a comparison between current and previous images is utilized to isolate objects of interest. When monitoring traffic on highways, median frame differencing has been used to detect objects in motion by subtracting a background frame from the current frame. However, further exploration is necessary for their application in space situational awareness (SSA). Hence, this chapter aims to apply these well-established methods to a novel SSA dataset. The results of this study will be used for implementation onboard a satellite for real-time resident space object (RSO) detection in the long term. The non-AI-based methods outlined in [37] have not been evaluated with space situational

awareness (SSA) images. Given the current limitations, a direct comparison among the existing algorithms is not feasible at this time. Future research could focus on a more direct comparison of the proposed algorithms while using similar datasets to further validate the findings of our study.

2.3.1 Adjacent Frame Differencing (AFD)

The AFD algorithm relies on subtracting adjacent frames within an image sequence to isolate moving objects. During the preprocessing stage, each frame in the sequence is first normalized to reduce the range of pixel intensity values. Normalization is necessary for the OpenCV software library to further modify the sequence, as images must be converted to an 8-bit format before processing occurs. After normalization, the algorithm iterates through the sequence and calculates the absolute difference in pixel intensities between the current and subsequent frames. The resulting differences in intensities are used to generate a new frame, with white pixels representing motion. Overlapping stars between adjacent frames result in black pixels, as subtracting identical pixel intensities results in a difference of zero. Following subtraction, size filtering is applied to remove remaining hot pixels and visual artifacts with an area smaller than a predefined threshold. The resulting frame is processed using OpenCV's contour detection function, and groupings of white pixels are identified as RSOs. Bounding boxes are then fitted to each contour to encapsulate the detected RSOs. Finally, the center coordinates of each bounding box are tabulated. A flowchart of the detection process with the adjacent frame differencing method is presented in Figure 6. Various frames are visualized in Figure 7. In the presence of a significant frame time, RSOs do not overlap between adjacent frames and, thus, are detected twice after subtraction. To mitigate double detections, overlapping bounding boxes in adjacent frames are combined, resulting in a single detection.

Table 2: Comparison of the detection methods.

Algorithm	**Description**	**Pros**	**Cons**
Frame differencing and background subtraction	Models the background using a running average. The background is subtracted from frames in sequence, and leftover pixels are in motion.	Simple implementation. Computationally inexpensive. Adapts to changing backgrounds.	Does not account for uninteresting motion (i.e., motion due to background objects moving). Limited to a fixed camera; relies on frames aligning with background.
Optical flow	The 2D motion vector for each pixel of an image is computed by comparing it with the next image.	Accurate; measures motion at pixel level.	Requires detailed features for effective use; RSOs may not be detailed enough.
Nearest neighbor	Objects are associated between images by finding the objects closest to them in the next image.	Can perform further analysis to differentiate the movements of RSOs and stars using position/velocity.	Not robust to overlapping RSOs/stars, illumination changes, or fast-moving RSOs.
Streak detection	Models use the plate solver for star removal for streak detection.	Avoids additional blurring. Accounts for uncalibrated images.	Needs a star catalogue.However, one of the potential applications involves utilizing a star camera, which inherently relies on a star catalog for its functionality. The observer's motion can heavily influence the output.

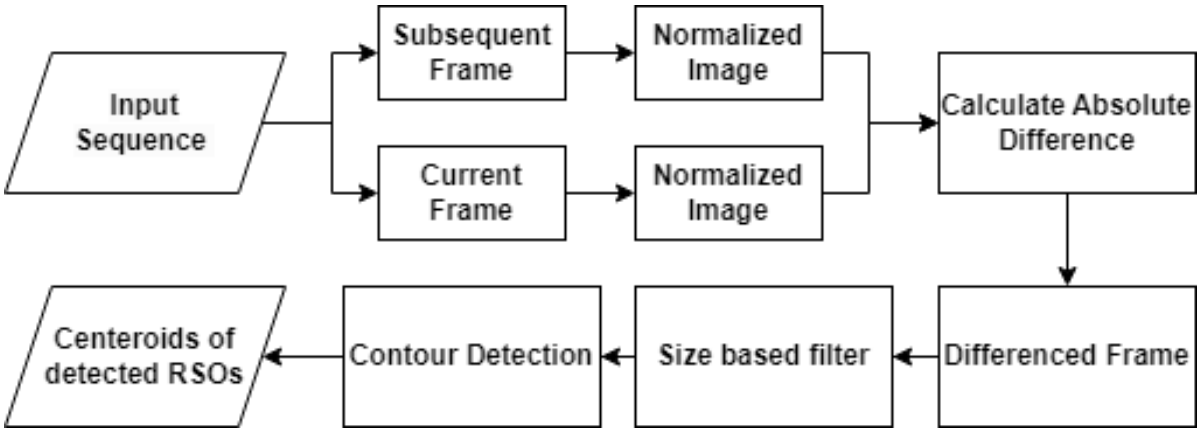

Figure 6: Flow diagram of adjacent frame differencing.

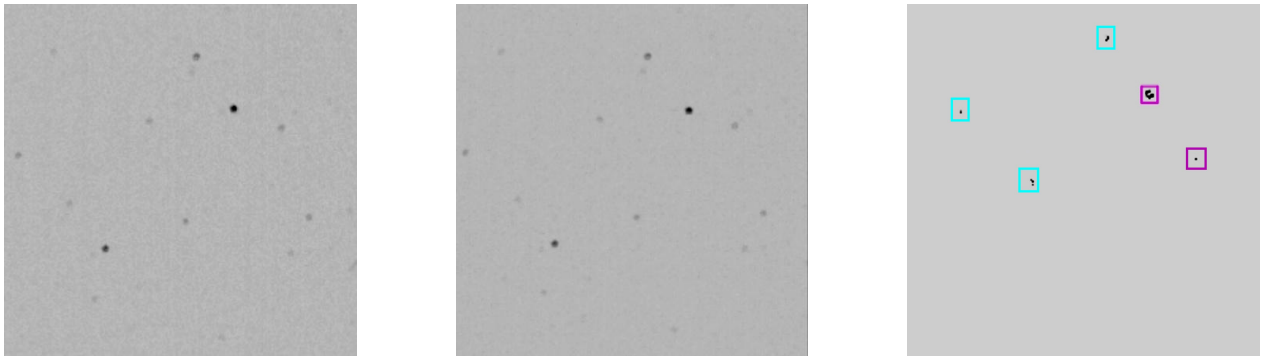

(a) (b) (c)

Figure 7: Visualization of AFD processing: (**a**) current frame, (**b**) subsequent frame, and (**c**) differenced frame; the RSOs are highlighted with a purple bounding box, and visual artifacts that are to be filtered are highlighted with cyan boxes.

2.3.2 Median Frame Differencing (MFD)

MFD involves subtracting each frame in an image sequence from a median frame in order to isolate moving objects. During preprocessing, each frame in the sequence is normalized and thresholded, similarly to the process in AFD. The operational flow diagram for the median frame differencing (MFD) algorithm is shown in Figure 8. The input sequence is then divided into equal segments of an arbitrary length, with a unique median frame being generated for each segment. Median frames are constructed by averaging the intensity of pixels in each frame throughout a segment. Frames within a segment are then subtracted from their corresponding median frames, revealing moving objects as white pixels, as illustrated in Figure 9 Visual artifacts and hot pixels are eliminated using size

filtering, and contours with a greater concentration of black pixels near their center are discarded. This filtering technique is effective in MFD as it does not capture moving objects in the median frame. As a result, RSOs retain their shape after subtraction due to the lack of overlap between the current frame and the median frame. Thus, stars are distinguished from RSOs by white pixels surrounding a dark centroid, while RSOs appear as tight groupings of white pixels. By leveraging this visual distinction, MFD accurately differentiates stars from RSOs. The resulting frame is then processed using OpenCV's contour detection, which identifies groupings of white pixels as RSOs. As in AFD, bounding boxes are subsequently fitted to each contour, and the center coordinates of each bounding box are then recorded.

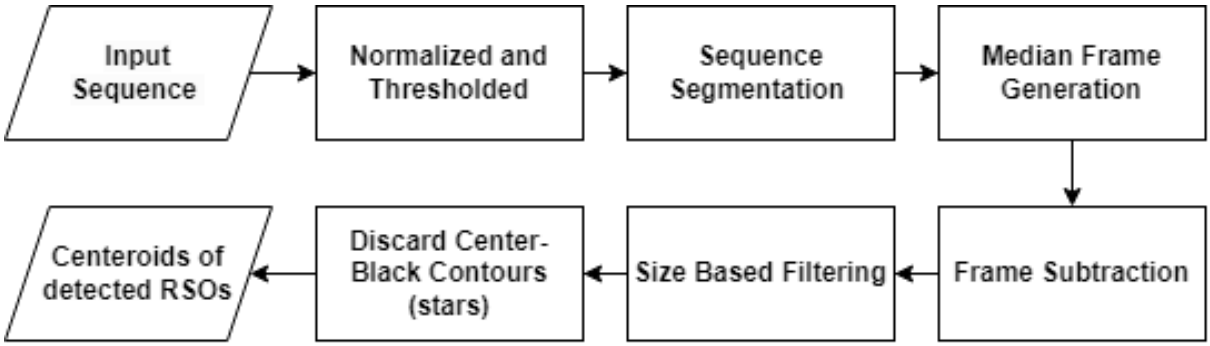

Figure 8: Flow diagram of median frame differencing.

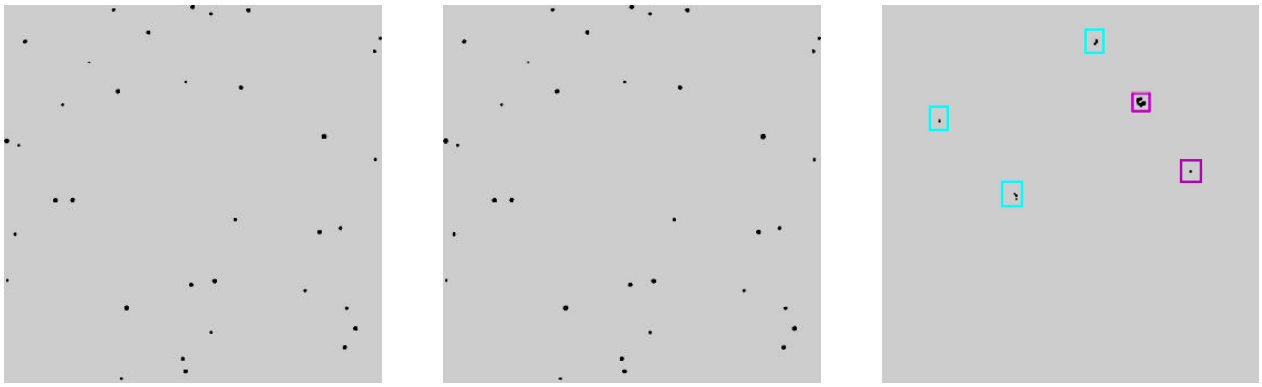

(a) (b) (c)

Figure 9: Various frames used in MFD processing: (**a**) the current frame, (**b**) median frame, and (**c**) differenced frame, in which the visual distinction between RSOs and stars can be observed. RSOs maintain their shapes and are highlighted with purple bounding boxes, whereas stars and artifacts, which display irregular shapes, are contained within cyan bounding boxes.

2.3.3 Proximity Filtering and Tracking (PFT)

PFT operates by generating a median frame, detecting all contours present, and fitting bounding boxes to each contour. The center coordinates of each bounding box are then stored in a list for later use.Figure 10 provides a functional flow diagram of PFT. The algorithm subsequently scans through each frame in the sequence to identify objects using OpenCV's contour detection, as presented in Figure 11 Any objects observed to be in close proximity to the previously saved coordinates are labeled as stars and promptly discarded. The remaining objects are tracked using a unique numerical ID that persists throughout the sequence. Also, moving objects that travel an insignificant distance between their initial and final appearances in the sequence are discarded. This prevents the detection of hot pixels, which appear in a single frame. Finally, bounding boxes are fitted to each remaining object, and the center coordinates of each bounding box are stored.

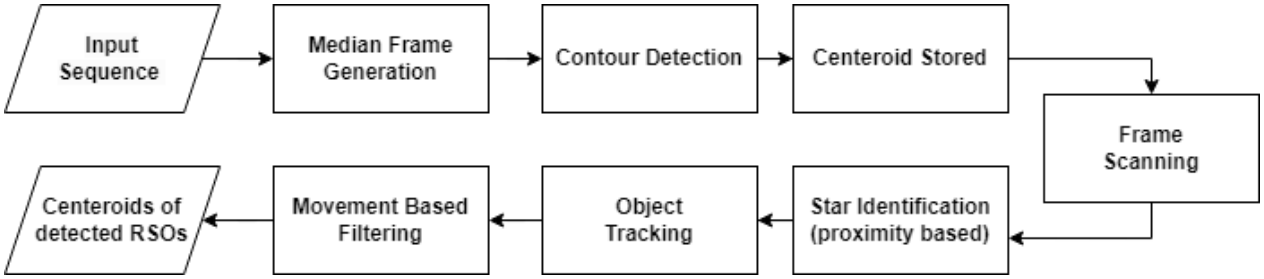

Figure 10: Flow diagram of proximity filtering and tracking.

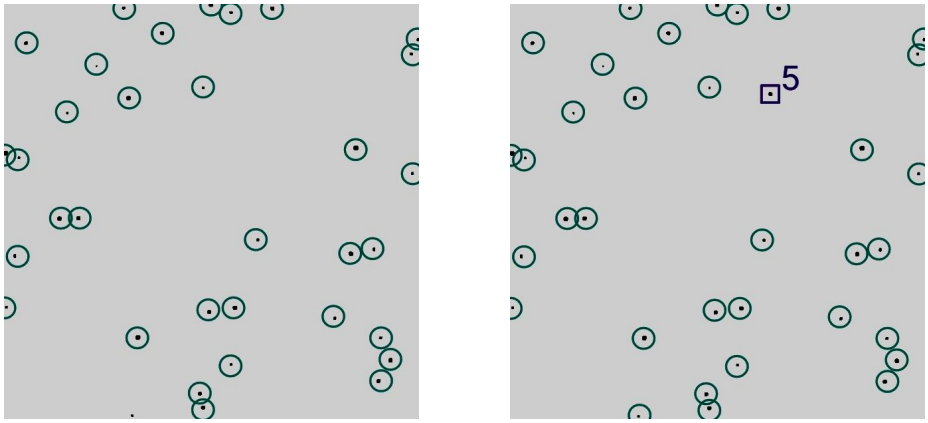

(a) (b)

Figure 11: Various frames used in PFT processing: (**a**) the median frame, where all contours present within the images are highlighted with bounding circles, and (**b**) the current frame, where an RSO is tracked with a unique ID and enclosed in a bounding box.

2.3.4 Streak Detection from Stacked Short-Exposure RSO Images

As an alternative to the frame differencing techniques described above, we deployed streak detection utilizing plate solving to prevent additional blurring from stacked images. As previously discussed, a series of short-exposure images can be stacked to create an image with RSOs in a line, resembling a streak.

One commonly used technique for streak detection is achieved with the use of edge detection, an image processing technique, which identifies abrupt changes in image intensity—typically at region boundaries—and defines these changes as edges. The Canny edge method stands out as a preferred choice due to its superior performance [42]. The Canny method involves several steps: An initial Gaussian filter is applied to reduce image noise, then the image gradient is evaluated using amplitude and angle calculations, thus refining the outlines. The final step includes a hysteresis-based thresholding process to preserve the desired edges while removing undesired ones. Subsequently, the Hough transform complements Canny edge detection by verifying the linearity of the edge and accurately estimating streaks. However, despite the denoising in the Canny method, the Hough transform may generate multiple lines for the identification of a single streak. Consequently, clustering is employed to isolate the specific streak, though this process can be time-consuming and susceptible to image noise.

In the current study, a stacking process was used to generate streaks from a set of twenty-seven individual images (more details on the data acquisition will be provided in Section 2.4.1). In the resulting stacked images, the stars appeared stationary, while RSOs were rendered as streaks. The stacking method provides numerous benefits, including decreased processing time, less of a need for computational resources, and an enhanced signal-to-background ratio for streak detection. However, the quality of the stacked images can be significantly impacted by the observer's motion, with the balloon's stability having a direct impact on the outcome.

Identifying "streaks" from star field images requires a step to remove stars. The stacked images underwent plate solving via Astrometry.net. This was chosen for its robustness, as it eliminated the need for additional information regarding calibration. Astrometry.net employs various image

processing techniques to precisely detect hundreds of stars, achieving sub-pixel accuracy. Each quad, which consists of four stars, is analyzed to assign a geometric hash based on the relative positions [43]. A Bayesian decision problem is employed to validate this alignment assessment, resulting in rare occurrences of false-positive matches [43]. For wide-angle images, the Tycho-2 catalog was utilized [43]. Once processed, the output files contained World Coordinate System (WCS) transformations, which provided correspondences between the pixel locations in the images and reference stars.

The WCS information was used to ascertain the pixel positions of all identified stars. For each of these located stars, a circular mask was created by calculating the squared distance between each detected star pixel in the image and the circle's center by utilizing the square of the circle's radius. Pixels residing in the inner regions of masks were then set to zero, effectively mitigating false positives caused by the presence of stars within these regions. Figure 12 provides a visual representation of an image before and after the removal of stars, with the scales indicating pixel intensity. The left side depicts the original image, while the right side shows the same image with the stars removed. The names of the stars and their BT and VT magnitudes (blue and visual magnitudes) were identified using the right ascension (RA) and declination (Dec) values from the header information. Additionally, the Euclidean distance between the stars' positions in the images and those in the index was calculated.

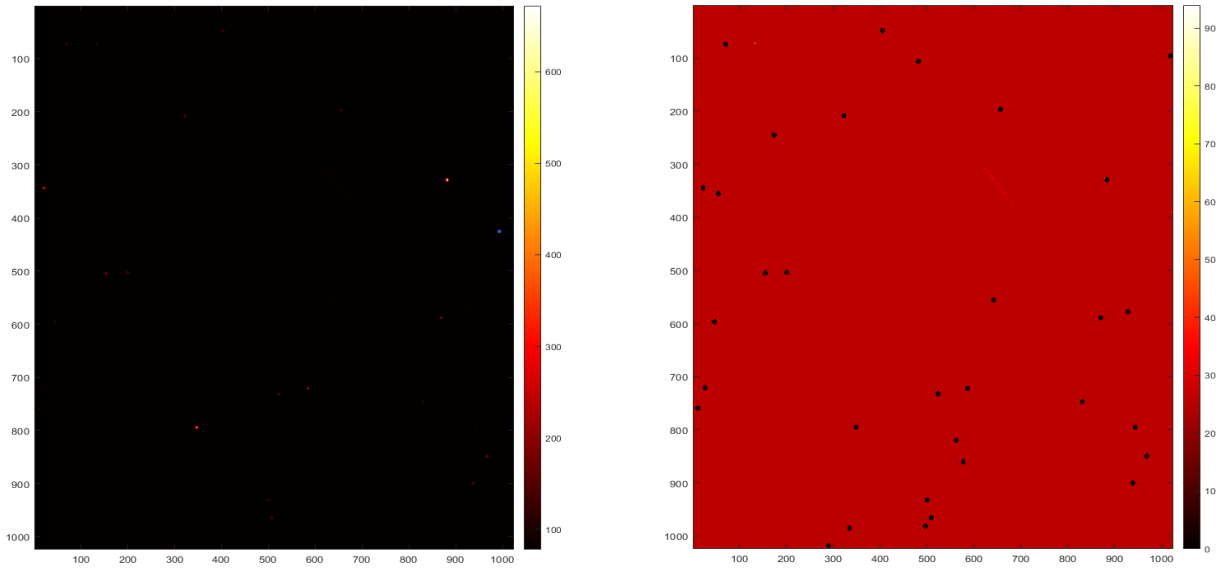

(a) (b)

Figure 12: Before star removal and after star removal; the pixel intensity scales are displayed as follows: (**a**) the original image before star removal, where the red dots indicate stars with high pixel values; (**b**) the same image after the stars were removed, with black dots indicating regions where stars were previously present, corresponding to the red dots from (**a**).

Dynamic thresholding was used to set regions with pixel intensities below the background brightness values to zero. Subsequently, the images were binarized to enable the use of OpenCV's "find contour" function. To minimize false detection, the area of the detected contours was evaluated, and an area-based threshold was applied. The area of the contours needed to exceed that of the largest contour in the image minus three times the standard deviation of the detected contours. This allowed for the removal of image artifacts. For each remaining contour, a mask was formed to isolate pixels situated above the background within the contour. The mask's minimum and maximum values identified the pixel coordinate of the streaks' endpoint. The distance between these coordinates was calculated to determine the streak's length. The streak length needed to exceed the radius used during star removal. The signal-to-background ratio (SBR) of the streaks was evaluated using the formula mentioned in [44]. A functional flow diagram of the algorithm is presented in Figure 13.

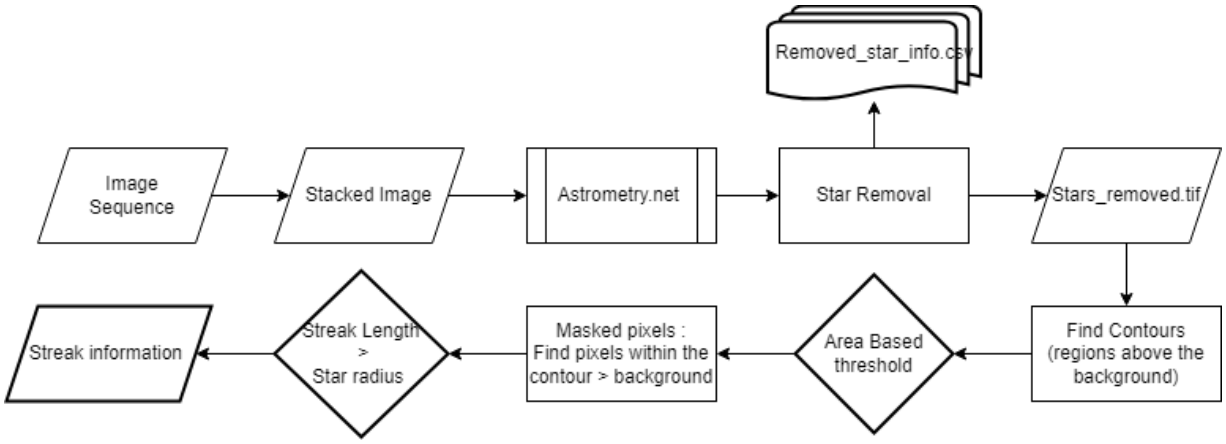

Figure 13: Flow diagram of streak detection.

2.4 Dataset Used in the Current Study

The scarcity of labeled data presents the greatest challenge in many applications in which true data are needed for training and verification. RSO images encounter a similar issue due to the absence of publicly accessible labeled data for algorithm design. Due to the shortage of labeled data, the researchers opted to use a simulated dataset containing synthetic streaks and RSOs. The simulated dataset primarily utilized BUAA-SID 1.0 and SPARK [45, 46]. BUAA-SID 1.0 comprises over 4000 images that were created by uniformly sampling around a satellite model with a single external light source. This dataset includes 20 distinct satellite models, featuring a variety of types, shapes, and functionalities, and they were all imported into the 3dsMax software. However, it lacks a simulation of the space environment. The SPARK dataset employs real models of 10 different satellites and spacecraft, in addition to five types of space debris. Nonetheless, it does not feature a comprehensive range of space debris models. Several other simulated SSA datasets focusing specifically on the estimation of the poses of spacecraft have been developed. Nevertheless, these datasets lack several elements found in the actual space environment. The only publicly accessible event-based space imaging dataset is provided by Western Sydney University [47]. Nonetheless, their sensors were ground-based telescopes, and there are inherent limitations of ground-based observations and challenges associated with the use of event-based sensors.

Numerous studies have successfully demonstrated the accuracy and precision of RSO detection in

simulated environments [48, 49, 50]. In contrast, implementing the proposed methods when using real-world images presents several challenges, including the presence of dead pixels, hot pixels, and cosmic rays, the unknown point spread functions of imagers, various effects that radiation imposes on the imager, and substantial stray light from sources such as Earth's albedo, the Moon, and the Sun. In particular, with space-borne images such as FAI, we have observed numerous scenarios in which the background lighting conditions (e.g., the south anomaly) make RSO detection extremely difficult. Therefore, for the purposes of this study, we tested the RSO detection algorithms with the dataset that we collected from the stratosphere and manually annotated for accuracy.

As noted earlier, manual labeling is considerably challenging due to the nature of these images. Annotating medical images, for example, is equally challenging and requires skilled experts. Similarly, the Cityscapes dataset explores the intricacies of real-world urban scenes and the complexity behind annotating them for applications in autonomous vehicles [51]. All of these challenges exist with RSO images. Distinguishing RSOs (moving dots) from stars (non-moving dots) in monochromatic images proves to be extremely challenging when relying solely on the naked eye. Additionally, the limited stability of an imaging platform that is also in motion presents an additional difficulty in annotation. The difficulties with RSO detection outlined in Section 2.3 were also hurdles that the annotators had to overcome.

2.4.1 RSONAR Mission Overview

The SSA dataset utilized in this paper was derived from the Resident Space Object Near-Space Astrometric Research (RSONAR) mission, which was launched in August 2022 on a stratospheric balloon platform as shown in 14. The payload of RSONAR provided a distinctive vantage point in the stratosphere to effectively observe RSOs, especially during dawn and dusk, when the phase angles were favorable for RSO observation. The payload RSONAR featured the pco.panda 4.2 from PCO Imaging based in Kelheim, Germany, which is a scientific complementary metal-oxide semiconductor (sCMOS) camera [52], complemented by a Zeiss 2229-998 C-Mount Industrial Lens obtained from Carl Zeiss Industrielle Messtechnik GmbH in Oberkochen, Germany [53]. The

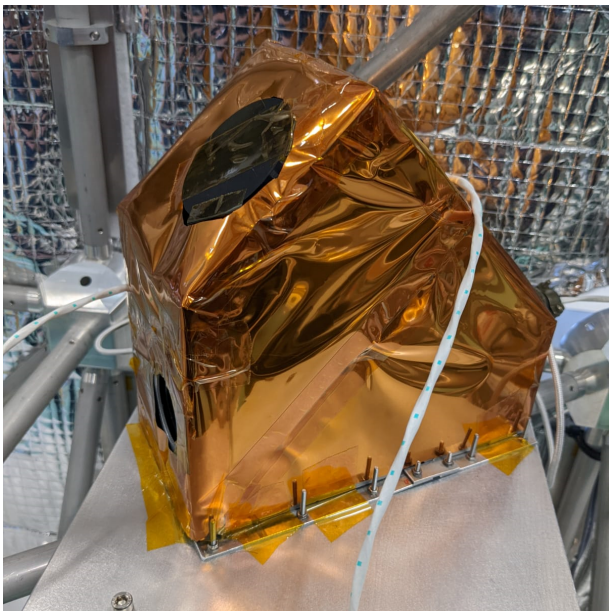

Figure 14: RSONAR Payload, flown on Stratos Balloon in August 2022

key specifications for the PCO camera used during the flight are detailed in Table 3. Comprehensive details regarding the hardware, operations, and payload development can be found in [54]. The mission, which was conducted as part of the Canadian Space Agency's STRATOS program in collaboration with the Centre National d'Études Spatiales [55], saw the payload operate for nearly 9 of the 13.73-hour day–night flights, from 3:27 to 12:24 UTC, while utilizing a strategic ballast release and pointing adjustments to maintain stability at altitudes between 30 and 45 km amidst minimal atmospheric turbulence.

Table 3: Imaging parameters used by RSONAR during flight.

Characteristic	**Values**
Aperture	12.5 mm
Bit depth	16 bits
Chromaticity	Monochrome
Exposure time	100 ms
Field of View	29.7°
Focal length	25 mm
Pixel size	6.5 μm / pixel
Pixel scale	104 arcsec/pixel
Quantum efficiency	82%
Resolution	1024^2 pixels

The main payload of RSONAR (with a PCO sCMOS camera) obtained 95,046 images through passive-mode observations. The dataset encompassed various elements, including star streaking as the balloon ascended, ballast deployment, and the intrusion of sunlight into the sensor at the end of the flight. The stability of the gondola played a critical role in minimizing the camera jitter due to the nature of the platform. To ensure continuous data acquisition throughout the operational period, twenty-seven images were collected in bursts, with a 4 s delay between each burst.

For this chapter, 429 images from this dataset were annotated. The images were categorized into three sequences containing 188, 134, and 107 images, respectively. These images contained parts of the Pegasus, Equuleus, and Aquarius constellations. The annotation process for RSOs was manually conducted using Astro ImageJ, a specialized image display environment with tools designed for the calibration and reduction of astronomy-specific images [56]. Using the graphical user in-

terface, the pixel coordinates of RSOs were annotated throughout the sequences. Astrometry.net was used for star annotation. The annotated data served as the ground truth for validating the algorithms' findings.

To the best of the authors' knowledge, this dataset is the first of its kind, offering images with a wide field of view that were passively acquired from a near-space environment. Consequently, the identification of resident space objects (RSOs) within the dataset, as well as any metadata that could enable the linkage of detected objects to verifiable resident space objects, will not be disclosed due to the sensitivity associated with them. The primary purpose of the dataset is to facilitate algorithm development. Additional research is currently being conducted to address the sensitivity concerns associated with this dataset.

2.5 Results

2.5.1 Metrics Used

The accuracy of the detection algorithms was gauged using three primary metrics: the precision, recall, and F1 score. The F1 score, which is the harmonic mean of the precision and recall, is a weighted average that favors the lowest-scoring metric. It serves as a general indicator of an algorithm's performance and is a better-suited metric due to its ability to account for class discrepancies. Additional secondary metrics, including true positives (TPs), false positives (FPs), and false negatives (FNs), were used to compute these primary metrics.

In object detection, TPs denote correctly identified RSOs, FPs represent stars misidentified as RSOs, and FNs are RSOs that the algorithms failed to identify. In streak detection, FPs indicate detected regions that exist outside the annotated values. TPs correspond to annotated values within detected regions. FNs pertain to annotated values that are situated outside the detected regions. Performance metrics are evaluated in Equations 1, 2, and 3, where we calculate precision, recall, and the F1 score, respectively.

$$\text{Precision} = \frac{TP}{TP+FP} \tag{1}$$

$$\text{Recall} = \frac{TP}{TP+FN} \tag{2}$$

$$F1 \text{ Score} = \frac{2 \times TP}{2 \times TP+FP+FN} \tag{3}$$

2.5.2 Results of Object Detection

AFD performed optimally when there was camera movement because the displacement of stars between successive frames was typically minimal. This was an advantage over MFD, which subtracted non-consecutive frames that were taken at different times, resulting in a potential misalignment of stars during differencing. Thus, for longer sequences or those containing camera jitter, AFD is the recommended algorithm. The ability to retain the shape of RSOs after differencing gave MFD an edge over AFD. AFD contained overlapping stars and RSOs in adjacent frames before subtraction, resulting in reduced distinctions between static and moving objects in the resulting differenced frame. Because MFD resulted in fewer misidentifications of stars as RSOs, it is the preferred algorithm when higher precision is desired. PFT offered a significant advantage over the other techniques by substituting size filtering with tracking, which was more effective at filtering out small hot pixels that existed in a singular frame. Moreover, because PFT omitted frame differencing techniques, it avoided the visual artifacts that arose from the subtraction processes found in both AFD and MFD. These artifacts in the latter algorithms necessitate additional filtering layers for removal. Hence, PFT is the preferred algorithm for greater recall, as the use of fewer filtering techniques minimizes the loss of true RSOs after preprocessing. The overall performance of these techniques is tabulated in Table 4.

Table 4: Overall performance metrics for object detection.

Method	Precision	Recall	F1 Score	TP	FP	FN
AFD	73%	63%	68%	387	143	226
MFD	95%	65%	77%	397	22	216
PFT	95%	73%	82%	447	25	166

In terms of overall performance, PFT outperformed both AFD and MFD, with an F1 score of 82%, while AFD had the lowest performance at 68%, which was primarily due to its lower precision of 73% compared to MFD and PFT, which were both at 95%. Recall presented challenges for all three algorithms, regardless of their processing techniques. Testing without any filtering during processing yielded maximum recall scores of 71%, 75%, and 87% for the respective sequences. These results highlight that the preprocessing phase significantly impacted the recall, as even without constraints during processing, the recall did not approach 100%. This suggests that preprocessing that involves thresholding and normalization filters out faint RSOs along with noise, resulting in a lower recall.

In the three sequences analyzed, which each presented distinct challenges, the performance of the detection algorithms varied. In the first sequence, which featured a mix of faint and prominent RSOs, MFD excelled in precision but struggled with recall due to its extensive filtering layers. Conversely, in the second sequence, which was primarily composed of faint RSOs, all algorithms faced recall issues because the preprocessing thresholding filtered out many faint RSOs, necessitating a trade-off between recall and filtering. In the third sequence, which was dominated by prominent RSOs, MFD marginally outperformed PFT due to its aggressive filtering, achieving higher precision and a somewhat unexpected higher recall rate, which was possibly attributed to PFT's tracking inconsistencies with RSOs covering substantial distances between successive frames.

AFD performed the worst in all three sequences, which was primarily due to its poor precision relative to the other algorithms. This was a result of RSOs and stars appearing nearly identical after the subtraction process, which caused difficulties in differentiating between static and moving

objects. Additionally, intermittent periods of long frame times resulted in RSOs being detected twice, as objects were too far apart in adjacent frames to combine bounding boxes. This variability in frame time is difficult to account for during processing, as it is a problem inherent to the dataset. PFT emerged as the best-performing method overall, as it relied on proximity filtering to detect RSOs rather than frame differencing. This proved useful in improving its recall rate, as fewer true RSOs were filtered out during processing. Frame differencing algorithms such as AFD and MFD rely heavily on filtering to account for visual artifacts that remain after subtraction, resulting in their comparably poor recall rates. In addition, rudimentary tracking proved useful for filtering out objects with limited movement, rather than relying on shape, size, and brightness for filtering, as in AFD and MFD; this is a characteristic of unreliable RSO identification.

2.5.3 Results of Streak Detection

In Figure 15, we present the streaks detected in all three image sequences, totaling twenty streaks. These images resulted from stacking the output from each set within its respective sequence. Table 5 presents the mean streak length in pixels and the signal-to-background ratio (SBR) for each sequence. A streak caused by the release of the ballast is visible and highlighted in the green box located on the left side in the first sequence. Although this streak is relatively narrow, it meets the area-based threshold for detection. The precision, recall, F1 score, and accuracy values for the sequences are tabulated in Table 6.

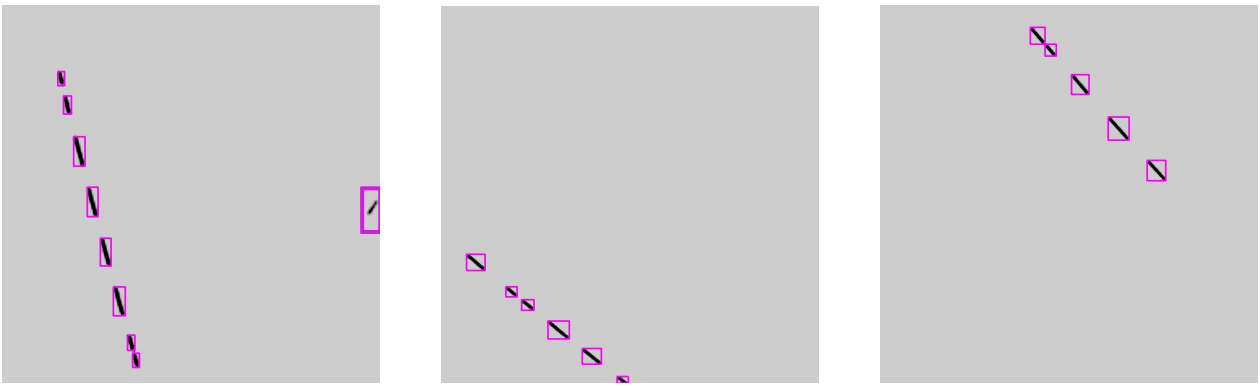

(a) (b) (c)

Figure 15: All detected streaks are highlighted with green bounding boxes: (**a**) first sequence, (**b**) second sequence, and (**c**) third sequence. The figures were enhanced using the ZScale algorithm to provide visual clarity.

Table 5: Sequence of images and their respective mean streak lengths (in pixels) and signal-to-background ratios (in dB) for the first, second, and third sequences.

Sequence Order	**Mean Streak Length (Pixels)**	**SBR (dB)**
First	56.51	27.32
Second	49.8	27.67
Third	61.04	26.64

Table 6: Precision, recall, F1 score, and accuracy values for each sequence.

Sequence Order	**Precision**	**Recall**	**F-1 Score**	**TP**	**FP**	**FN**
First	100%	48%	65%	158	0	169
Second	100%	71%	83%	117	0	47
Third	100%	79%	88%	99	0	27

Overall, the algorithm exhibited its poorest performance in the first sequence, where it achieved an F1 score of 65%. This deficiency in performance can be attributed to the low recall, especially

in sequences featuring ballast streaks and faint RSOs. It is important to note that a precision of 100% was achieved. This might have been a result of the specific definitions of TPs and FPs, which were customized for streak detection with manual annotations made for object detection. There is a possibility that the algorithm might have overperformed since it was designed to perform optimally with stable data from RSONAR, thus prioritizing the simplification of complex image processing and emphasizing detection accuracy. The relatively low recall values further suggest that the algorithm encountered challenges in identifying RSO streaks that fell below the noise threshold.

2.6 Conclusions

In this chapter, we demonstrated three accessible and effective RSO detection methods that used frame differencing and are capable of enhancing space situational awareness. Combining both conventional tracking and proximity filtering techniques proved to be most effective in identifying moving objects under a variety of conditions. We also implemented streak detection using low-resolution wide-field-of-view optical imagery, with a focus on minimal image processing. With the positional data collected from each algorithm, the trajectory of potentially harmful space debris can be predicted and used to mitigate future collisions, thus ensuring that important communication, navigation, and space observation satellites remain unharmed. As the amount of space debris increases at an unprecedented rate, the democratization of detection techniques becomes necessary for protecting the Earth's orbital environment for decades to come. Table 7 summarizes the optimal detection methods for various applications according to the results described in the previous section.

Table 7: Summary of the performance of the detection methods with various parameters.

Parameters	Optimal Algorithms
Onboard Processing	MFD
Real-time Processing	PFT
Least False Negatives	Streak Detection
FPGA Implementation	MFD
Changing Light Conditions	Streak Detection
Best Accuracy	Streak Detection
Most Flexible	MFD

2.6.1 Future Work

To enhance the performance of the algorithms, several key adjustments should be considered. First, in the case of AFD, it is essential to reduce and stabilize the frame time during processing. This modification would bring RSOs closer together in consecutive frames, thus mitigating double detections and, ultimately, improving the precision of AFD. Additionally, minimizing camera jitter within the dataset would have a positive impact on precision across all three algorithms, particularly when distinguishing stars with motion patterns resembling those of RSOs. An alternative approach involves analyzing object trajectories and separating camera motion from object motion to reduce overlap between stars and RSOs. Furthermore, for both AFD and MFD, replacing size filtering with tracking is recommended, as it can significantly increase the recall rates by allowing faint RSOs to be detected while also reducing the filtering of hot pixels and visual artifacts. Although this may slightly affect the precision, especially in MFD, the impact can be effectively mitigated with a consistent frame time. Finally, it is advisable to avoid overly aggressive thresholding during preprocessing, as it can lead to a significant drop in recall rates by filtering out faint RSOs and background noise. Instead, relying on OpenCV's contour detection can provide better recall,

but it is essential to consider additional post-processing filtering to maintain precision when handling the increased number of detected objects, thereby reducing the risk of misidentifying stars as RSOs.Traditionally, frame differencing techniques were employed during the development of such algorithms, which necessitated the reduction of the image bit depth. However, retaining images at 16 bits could potentially improve the detection metrics, albeit with consideration for the hardware limitations that this may impose.

Currently, streak detection identifies streaklets separately because of the data themselves. The next step is to add margins to the end of each streak to see if streaklet merging occurs in subsequent subsets. Additionally, the RA and Dec values of streaks can be used for correlation and identification with known catalogs, while the streak magnitude can be evaluated using the visual magnitudes of reference stars present in an image.

To further validate these methods, ground-based observation campaigns were conducted using the same imaging system. These observations established the effectiveness of the algorithms with images obtained from the ground, indicating their potential applicability across various observational platforms. Future studies will comprehensively compare ground-based and stratospheric RSO detection while utilizing the same imaging system. Additionally, future research will explore the adaptability and effectiveness of these algorithms under various observational conditions.

3 High-Altitude Optical Imaging of Resident Space Objects (RSOs) from Stratosphere

This chapter is based on a study that explores the use of a stratospheric platform for Space Situational Awareness (SSA) through high-altitude imaging of Resident Space Objects (RSOs). The findings of this study were submitted for publication on May 2, 2024, and the article is currently under review at the time of writing. The study addresses limitations of traditional ground- and space-based observations, such as atmospheric interference and limited access to public datasets, by validating the use of dual-purpose Star Trackers (STs) for SSA. These STs leverage their wide field of view for RSO imaging while maintaining their primary function in satellite attitude determination. Data from the RSONAR mission, which involved capturing over 95,000 images at an altitude of 36 km in star-stare mode (SSM), is used to detect RSOs transiting the field of view. Photometric and astrometric evaluations—including Full Width Half Maximum (FWHM), Signal-to-Noise Ratio (SNR) with Astrometry.net—were conducted to analyze stars and RSOs. The study applies detection techniques from chapter 2 with the addition of an RSO image classifier. Among the methods evaluated, the Proximity Filtering and Tracking (PFT) technique detected the most RSOs (22,036), followed by Adjacent Frame Differencing (AFD) with 18,566, and Median Frame Differencing (MFD) with 9,194. Additionally, 387 RSO streaks were identified, primarily near dawn. Over 500 unique RSOs were manually annotated and analyzed based on SNR, FWHM, angular velocity, and magnitude. The results demonstrate that dual-purpose STs can be an effective, low-cost alternative for SSA. This chapter confirms the feasibility of using dual-purpose STs in stratospheric balloon platforms for SSA, highlighting their potential to complement existing ground- and space-based systems.

I analyzed the RSONAR dataset to assess its effectiveness in capturing RSOs while simultaneously retrieving attitude information. I preprocessed and extended the annotations for RSOs from chapter 2 with diverse characteristics under varying lighting conditions and characterized them based on Signal-to-Noise Ratio (SNR), Full Width Half Maximum (FWHM), angular velocity, and

magnitude. Additionally, I evaluated the performance of a dual-purpose Star Tracker for Space Situational Awareness (SSA) during stratospheric flights, focusing on both attitude determination and RSO imaging, successfully identifying over 500 unique RSOs within a 157-minute imaging period. Aiden Alexander Sanvido developed the frame differencing techniques (AFD, MFD, PFT) under my supervision. Andrea Vallecillo Baires developed the RSO image classifier. Marissa Myhre provided the initial draft for figure 22, which I later modified before submission. Regina Lee supervised the project, secured funding, and contributed her expertise in SSA. All co-authors provided feedback and revisions to the manuscript. I performed all calculations, prepared all figures (except those provided by Marissa), and wrote the manuscript with revisions from my co-authors.

3.1 Introduction

Since the launch of Sputnik on October 4, 1957, satellites have become an integral part of our daily lives. As of March 2024, approximately 119 space agencies and countries operate nearly 8,000 active satellites in orbit. With companies like Starlink deploying mega-constellations, these figures are expected to rise. In addition to active satellites, various man-made elements also orbit in near-Earth space. These include fragments from rocket bodies, dislodged components from decaying satellites, debris from collisions and anti-satellite weapons tests that travel at hypervelocities which pose a significant threat to operational satellites. Consequently, it is increasingly necessary to identify, track, and catalog all RSOs to prevent collisions and safeguard space missions from premature termination.

3.1.1 Overview of Ground and Space-Based SSA Architecture

Traditionally, the SSA has been conducted using ground-based radars and optical sensors. The sensors may be classified as either ‘active’ or ‘passive’ with the observational periods and operations constrained by the instrumental setup. However, SSA from ground-based sensors is limited by their geographic locations as there are inherent variations in sensor distribution between the northern and southern hemispheres. Consequently, previously tracked objects may move out of the

sensors' reach for months when their orbits shift, thereby affecting trackability. The ability to track an object is determined by its cross-sectional area and requires tracking by two or more sensors. Ground-based radars are only capable of detecting objects in Low Earth Orbit (LEO) and Medium Earth Orbit (MEO) [57]. In contrast, ground-based telescopes can detect objects in higher orbits such as Geosynchronous Equatorial Orbit (GEO). However, the operational period of these telescopes is limited by cloud coverage, and they are only functional during the night. Furthermore, the efficacy of telescopes is constrained by the phase angle of RSOs, which is the measurement of sunlight reflecting off RSOs. Additionally, images captured by these telescopes are significantly influenced by atmospheric turbulence and light pollution. Sensors in low-elevation regions experience diminished observational capabilities due to the additional atmospheric presence. Currently, ground-based optical sensors serve as the primary source of optical data for RSO identification and characterization. The detection of RSOs in LEO using ground-based images presents a significant challenge due to the telescopes' limited field of view (FOV) as the RSOs transit at hypervelocities. Nevertheless, the observation in GEO is possible due to the stationary nature of the sensors. This necessitates the operation of the sensors in Track Rate Mode (TRM) on a precision motorized platform.

A key advantage of space-based sensors is their ability to observe objects without interference from Earth's atmosphere. Additionally, they are capable of observing objects closer to the sun compared to ground-based sensors. Furthermore, they have less latency for targeted observation, which can be accomplished within a few hours. Despite these advantages, space-based systems often incur higher costs and reduced sensitivity compared to ground-based systems. According to Ackermann, Mark R., et al[58], the cost (USD) of ground-based sensors ranges from $0.76 to $1.59 per observation, while that of space-based sensors ranges from $ 21.92 to $ 24.35 per observation. However, the ORS-5 satellite, observing the GEO belt, is an outlier among space-based sensors, costing $ 3.07 per observation.

3.1.2 Dual-Purpose of SSA Sensor

Given the sensitivity of SSA and the constraints on data acquisition by dedicated SSA sensors, access to data is limited and rarely available to the public. A study has been conducted on the utilization of existing space-borne sensors for SSA purposes [28]. Additionally, Star Trackers (ST), which are traditionally employed for attitude determination, have been investigated for RSO imaging[32, 31, 59, 29]. ST offer a more cost-effective alternative to dedicated SSA sensors. Their wide FOV enables increased coverage, facilitating earlier detection and warning of potential conjunctions. However, it should be noted that STs have inferior imaging capabilities compared to dedicated SSA sensors. Nevertheless, their imaging is sufficient for astrometric and photometric analysis, thus providing additional information about RSOs.

3.1.3 Overview of Stratospheric Ballooning for Scientific Observations

Since the early 19th century, scientific ballooning has evolved into a significant venue for conducting cost-effective research [60]. The platform provides stable photometry, the potential for diffraction-limited imaging, and a very low sky background, enabling observations that cannot be ground-based. Additionally, due to its suborbital nature, it has been utilized for prototyping satellite designs and space experiments. High-altitude stratospheric balloons operate within atmospheric regions of 30-40 km, above 99.3% of the atmosphere, thus being free from atmospheric turbulence. According to [61], balloon-borne optical systems can produce images of comparable quality to those from spaceborne optical systems.

The Balloon Rapid Response for ISON (BRRISON) was constructed to meet the observation window required to study the ISON comet. The Balloon Observation Platform for Planetary Science (BOPPS) was the successor of BRRISON and addressed the anomalies endured by BRRISON. In addition to making scientific observations of Oort cloud comets during its flight, the results from these missions further emphasized the significance of balloon-borne observatories [62]. The Gondola for High Altitude Planetary Science (GHAPS) is a balloon-borne observatory with an optical telescope assembly that has a pointing accuracy of 1 arcsecond or better [63]. The Euro-

pean Stratospheric Balloon Observatory (ESBO) is currently being developed to provide regular observations in the far infrared and parts of the UV using stratospheric balloon observatories [64]. Smaller high-altitude balloons, referred to as meteorological balloons, have also been utilized for low-cost prototyping and rapid testing. They are capable of reaching high altitudes but are limited to payloads of a few kilograms and short observation periods [65].

To fulfill the scientific requirements, various types of flights and balloons have been developed. Turn-around period flights capitalize on the cessation of high-altitude winds that prevail in late spring and summer to maintain the platform's relative stability. These flights are relatively brief, lasting a few days after launch, and payloads are retrieved in close proximity to the launch station. In contrast, transoceanic flights are long-duration flights that can last for weeks and cover vast distances. An example of such a flight is the transatlantic flight, which traverses the Atlantic Ocean from Europe to the United States [60]. Ultra-long duration balloon flights are equipped with super-pressure balloons that can remain aloft for approximately 100 days [66]. Smaller high-altitude balloons, referred to as meteorological balloons, have also been utilized for low-cost prototyping and rapid testing. While they can reach high altitudes, their payload capacity is limited to a few kilograms with short observation periods. Additionally, the flexibility of ballooning allows for payload retrieval and rapid validation of findings and performance before reflight or a space launch. Despite the advantages of ballooning, it is constrained by the risk of payload damage upon landing, which must be considered.

3.1.4 Resident Space Object Near-space Astrometric Research (RSONAR) Overview

The scientific objectives of the Resident Space Object Near-space Astrometric Research (RSONAR) mission were threefold: firstly, to demonstrate the concept of a dual-purpose ST for SSA; secondly, to acquire data with different sky backgrounds in the suborbital environment for SSA research; and thirdly, to evaluate the stratosphere as an alternative platform for SSA. Hence, a low-cost CubeSat-scale payload was developed. RSONAR was a 2U CubeSat equipped with a commercial-grade ST, a scientific Complementary Metal–Oxide–Semiconductor (sCMOS) imager, and a Field Pro-

grammable Gate Arrays (FPGA) - based onboard computer. The RSONAR was launched as part of the STRATOS 2022 program, a joint venture between the CSA and the Centre National d'Études Spatiales (CNES) that uses stratospheric balloons with stabilized, precise pointing period flights. Additional information on hardware design concepts, operations and payload development can be found at [54]. The dataset obtained from the flight significantly aided in the development of robust RSO detection algorithms, as it contained RSOs with different characteristics, posed challenges associated with a moving observer, and included varying illumination conditions [18]. Ongoing studies are using this dataset for AI-based RSO detection, identification, and tracking.

The objective of this chapter is to validate the concept of dual-purpose ST for SSA through a comparative analysis of the astrometric and photometric properties of the observed stars and RSOs during the flight. Based on these results, we discuss the feasibility of using stratospheric flights as an alternative platform for SSA data acquisition. Section 3.2 outlines the RSONAR flight profile. Section 3.3 summarizes the astrometric and photometric evaluation methods to analyze the ST's dual purpose of RSO detection and attitude determination. Section 3.4 presents the results and discussion. Finally, section 3.5 provides a conclusion and explores areas for future research and improvement.

3.2 Dataset from RSONAR

RSONAR focuses on imaging RSOs with optical cross-sections of 20 cm and larger, which includes CubeSats, operational satellites, and larger debris fragments. Networks such as LEOLABS, which specializes in SSA, provide full orbital information for debris 10 cm and above. However, practical limitations in observational coverage, signal-to-noise ratio, and sensor restrictions often make objects that scale challenging to detect consistently in all environments. By selecting a 20 cm threshold, this study leverages a more reliable subset of RSOs that aligns with the detection capabilities of our imaging system. This size range also reflects a balance between observing critical debris and operational satellites while ensuring robust detection and characterization accuracy.

Passive observation and imaging, without accounting for the motion of the observer and RSOs,

can be referred to as Star Stare Mode (SSM). SSM employs lower exposure rates, which are often found in STs. In this mode, RSOs transiting within the imager's FOV may appear similar to stars. Although the higher exposure rates for RSO imaging offer significant improvements in observing dimmer RSOs [67], rendering them as streaks, this technique is often utilized in TRM. Due to the nature of the stratospheric platform and RSONAR's mission concept, TRM operation is not feasible. Consequently, imaging during the flight was conducted using SSM, which further validated the concept of dual-purpose STs for SSA.

On August 21, 2022, during a day-night turnaround flight, RSONAR acquired 95,046 images with an exposure rate of 0.1 seconds. The images were collected in bursts, with a 4-second delay between each burst, ensuring continuous data acquisition throughout the entire operation period. The satellite was powered off after 537 minutes of operation.

Upon reaching an altitude of 36 km at 01:56 am local time (UTC -4), the gondola commenced a coasting phase, with ballasts being released intermittently throughout the mission to maintain stability. The optimal period for SSA imaging occurred between astronomical dawn (4:02 am) and sunrise (06:03 am). During this period, the sun's geometric center rose from 18 degrees below the horizon, providing sufficient illumination of RSOs without saturating the imager. This overlapped with the stabilized pointing period (SPP), which lasted from 2:56 am to 5:33 am. The images captured shortly after the SSP were susceptible to stray light stemming from the earth's albedo, with complete saturation occurring at 6:34 am. Consequently, the data obtained during the 157-minute SSP represents the primary focus of analysis in this paper.

3.3 Methodology

In this chapter, image stacking was employed to combine images from each sequence into a singular image. Initially appearing as dots, the RSOs will now render as streaks while the stars remain relatively stationary. The stacking process offers several computational benefits, including reduced processing time and resource allocation. Additionally, it improves photometry by increasing the SNR and was used for the photometric residual analysis of stars. However, the observer's motion

during acquisition can affect stacked images' quality. Consequently, the RSO object detection algorithms employed the acquired images, whereas the RSO image classifier and RSO streak detection algorithms analyzed the resulting stacked images from the dataset. In [18], the performance of the algorithms was evaluated with this dataset using the performance metrics of precision, recall, and F1-score.

3.3.1 Full Width Half Maximum (FWHM)

The starlight is distributed across a number of pixels. The width, described by the full width at half maximum (FWHM), varies across the image plane as a consequence of the optical configuration. The accuracy of centroiding is contingent upon the width in question and is inversely proportional to it, exhibiting a decline as the width increases. The full width at half maximum (FWHM) is a commonly utilized metric for assessing image quality, as it provides a means of evaluating the image's spatial resolution. The star detector algorithm DAOStarFinder [68] was utilized with an initial guess value and a threshold value to locate all potential sources. The Levenberg-Marquardt (LM) least squares fitting algorithm [69] was used to apply a 2D Gaussian to each detected source, allowing for the measurement of the FWHM of each source. LM selects either gradient descent or the Gauss-Newton iterative algorithm to identify a solution based on the initial guess value.
Another method of evaluating the FWHM is through radial profiles of stars. A radial profile consists of Analog Digital Unit (ADU), which is a numerical count of the analog voltage corresponding to each pixel, as a function of radial distance from the center of the target object. Radial profiles enhance the extraction of spatial information of stellar sources, as they provide insights into aperture radii. Therefore, radial profiles of Epsilon and Alpha Pegasi were generated. The two stars were selected because of their luminosity, which ranked them as the brightest and third brightest stars in the Pegasus constellation. Furthermore, they were present throughout the entire dataset.

3.3.2 Astrometric Residuals

In wide-field astronomical imaging, distortion can significantly affect positional accuracy. In addition to intrinsic and extrinsic calibration using Zhang's calibration method [70], a plate-solving technique was utilized on the imaged field to map pixel coordinates to celestial coordinates within a World Coordinate System (WCS) [71]. This was achieved using known reference stars as benchmarks.

3.3.3 Photometric Residuals

Astrometry.net [43] identified 31,759 stars from the dataset. Figure 16 shows the distribution of observed stars as seen from Earth, using an Aitoff projection. The BT and VT magnitudes representing the colour bands were extracted from the TYCHO-2 catalogue using the celestial coordinates of the observed stars. These magnitudes can be used to approximate the Johnson photometry V magnitude, as demonstrated in Equation 4.

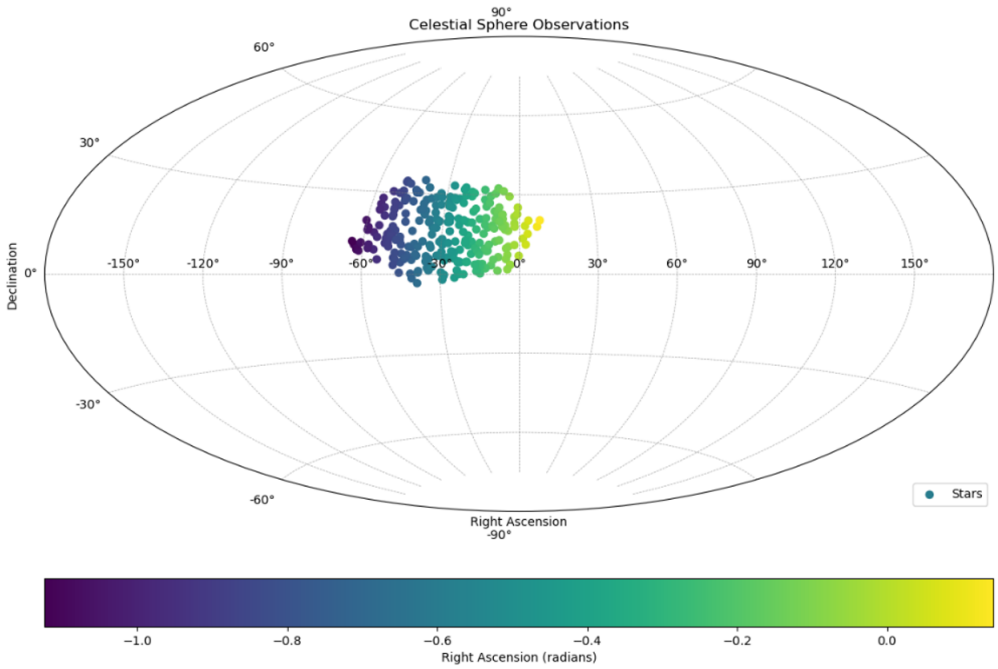

Figure 16: illustrates a projection of celestial sphere observations, plotting the positions of stars in terms of Right Ascension (RA) and Declination (Dec).

$$V \text{ magnitude} = VT - 0.090 \times (BT - VT) \tag{4}$$

The instrumental magnitude was evaluated using aperture photometry [68]. The flux of the stars within the images was calculated by summing the pixel values within the zone of concentrated starlight. The pixel values in the surrounding zones were evaluated to account for the sky background value. Consequently, the instrumental magnitude can be calculated using the Equation 5. The discrepancy between the instrumental and catalogue magnitudes is used to perform photometric correction.

$$\text{Instrumental Magnitude} = -2.5 \times \log_{10}(\text{Flux}) \tag{5}$$

ST cameras are subjected to various types of noise, including shot noise, which is dependent on observations, and read or dark noise, which is independent of observations. The power in a star signal can be calculated approximately by summing the pixel values of the window that was chosen around the star. For the purpose of this study, we only account for noise that is independent of observations. The signal-to-noise ratio (SNR) of the stars can be expressed as:

$$\text{SNR} = \frac{S}{\sqrt{S + (N_d t) + N_r^2 + \text{SB}}} \tag{6}$$

where S represents the signal, the instrumental flux of the observed star. N_d refers to the dark current (e^-). N_r represents the read noise (e^-), the exposure time (t) used for imaging, SB refers to the sky background of the stars.

Furthermore, we manually identified and annotated 500 RSOs present in our dataset, utilizing AstroImageJ[56]. This software enabled the precise annotation of pixel coordinates and the extraction of key properties such as SNR and FWHM for each transiting RSO. These values were employed to evaluate the magnitude of the RSO using the equation 7 [72].

$$\text{Magnitude of RSO} = -2.5 \log \left(\frac{(SNR^2)hc}{1.78 \times 10^{-8} Q_e A \lambda T} \right) \tag{7}$$

In Equation 7, h represents Planck's constant, while c denotes the speed of light. The term Q_e denotes the sensor's quantum efficiency. The variable A refers to the effective area of the aperture through which light enters the system, while λ signifies the wavelength of light, which for this study is fixed at 551nm. Finally, T is the integration time, represents the integration time, which is the duration over which the sensor collects light.

3.3.4 Attitude Determination

Astrometry.net was utilized to determine the attitude of the payload due to its 99.9% success rate [43]. The robust nature of Astrometry.net eliminates the need for image-pointing orientation and scale and renders optimal for passive observation on moving observer datasets, such as that of RSONAR. The application generates a list of calibration values, including Right Ascension (RA), Declination (DEC), and orientation east of north with respect to the boresight of the optical sensor. In accordance with our convention, yaw is defined as the RA, pitch as the negative of the DEC, and roll as the orientation east of north.

3.3.5 RSO Detection

The 157-minute SSP was critical for the RSO detection analysis. A total of 1,000 image sequences, comprising 27,027 images from this phase, were processed through RSO detection algorithms. To facilitate a thorough analysis, the observation period was systematically segmented into 30-minute intervals, except for the final segment, which extended for approximately seven minutes.

RSO image classifier

The image classification algorithm is utilized to categorize stacked sequences into groups of potential objects of interest. This includes a category of star field images devoid of RSOs, sequences with one or more RSOs, and sequences with obstructions. Initially, a Wiener filter is applied to these stacked images with the objective of reducing noise. This is followed by a thresholding technique to mitigate the noise floor, thereby enhancing the detectability of dimmer RSOs. Subsequently, the Canny edge detection algorithm isolates potential objects of interest. During this phase, smaller

objects, such as stars, are systematically excluded. The final step involves distinguishing between RSO streaks and obstructions, such as stray light.

RSO Streak Detection

This algorithm is designed to detect streaks in star field images. It begins with the elimination of stars that are susceptible to image noise. The process begins with plate solving [43]. Circular masks based on identified stellar radii are then applied around each star. This effectively nullifies pixels within these masks. Subsequently, dynamic thresholding and OpenCV's "find contour" function are employed to identify potential streaks [73]. An area-based threshold is applied to these contours to filter out artifacts, and additional masks are generated around the remaining contours to ascertain the endpoints of each streak. The algorithm then calculates the length of these streaks, ensuring that they were not created due to obstruction. It also evaluates their SNR and celestial coordinates.

RSO Object Detection

In [18], three frame differencing methods were developed and assessed for RSO detection: Adjacent Frame Differencing (AFD), Median Frame Differencing (MFD), and Proximity Filtering and Tracking (PFT). AFD subtracts adjacent frames in an image sequence to isolate moving objects. Median Frame Differencing (MFD) isolates moving objects by subtracting each frame in an image sequence from a median frame. MFD accurately differentiates stars from RSOs after differencing. Proximity filtering and tracking (PFT) relies on generating a median frame, detecting all contours present, and fitting bounding boxes to each contour. PFT replaces size filtering with tracking, which is more effective at filtering out small artifacts that exist for a single frame.

3.4 Results and Discussion

3.4.1 Full Width Half Maximum (FWHM)

Figure 17 depicts the distribution of FWHM values, a metric that indicates the apparent size of stars in a flight image and is a determinant of image resolution quality. FWHM is particularly relevant under the payload's orientation at a 45-degree elevation angle relative to the gondola, as it reflects

the sensor's seeing conditions, which impact image resolution. The mean and median FWHM are 3.67 and 4.06, respectively, delineated by dashed red and dashed green lines. Generally, lower FWHM values signify sharper images with more point-like sources, which is a desirable quality for attitude determination. The histogram exhibits a skewness of approximately -1.04, indicating that most sources are dimmer stars with relatively small FWHM values. The presence of larger FWHM values can be attributed to the observation of brighter stars such as Epsilon and Alpha Pegasi. The radial profiles of Epsilon derived from the non-stacked images themselves, yield FWHM of 5.84 and 4.39, respectively. Although Alpha Pegasi exhibits a smaller FWHM value, the inner and outer radii of the sky-background annulus are larger by 0.09 pixels and 0.2 pixels, respectively. This discrepancy is primarily attributed to the presence of distortion, as Alpha Pegasi is situated further from the boresight of the camera. Nevertheless, the FWHM values derived from these stars further corroborate our findings presented in Figure 17.

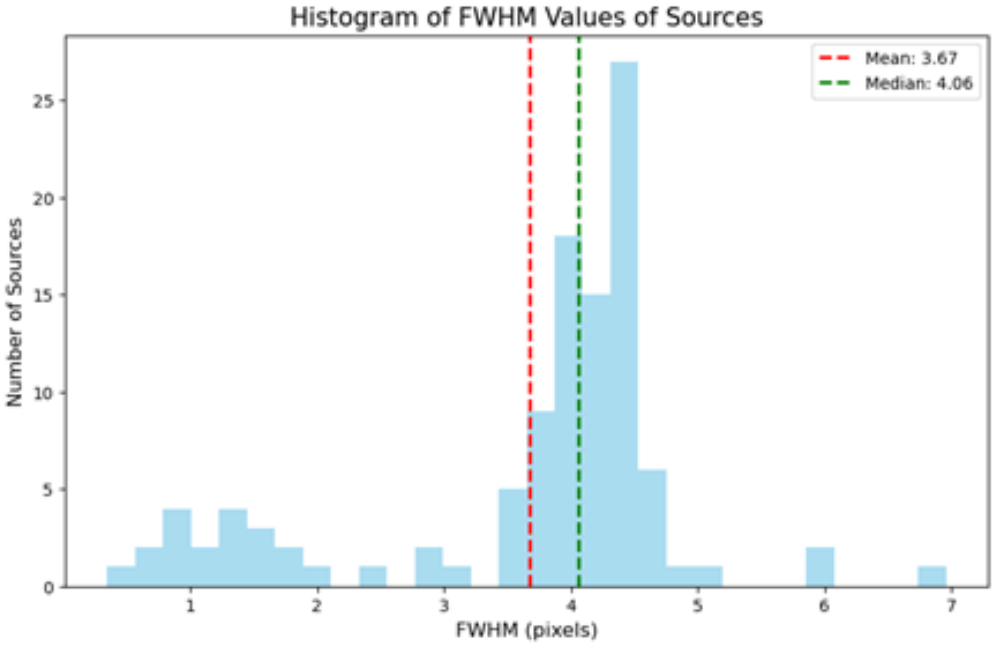

Figure 17: Illustrates the full width at half maximum (FWHM) of sources within an image from the dataset

3.4.2 Astrometric Residuals

Figures 18 and 19 present the distribution of residual errors in RA and DEC after distortion corrections. The histograms represent the frequency of residuals, thereby providing insight into the precision of the distortion correction method relative to the known positions of reference stars. The histogram of RA residuals in Figure 18 indicates that the distortion correction for RA is relatively precise, with most values concentrated within a range of -15 to +15 arcseconds. Only a few residuals extend beyond this range. The DEC residuals in Figure 19 display a similar concentration of around 0 arcseconds; however, they exhibit a broader range of up to +/- 20 arcseconds. In particular, a few outliers are observed at the extremes, especially around 30 and 40 arcseconds, as some sources exhibited astrometric distortion post-correction. It is anticipated that the residual distortion observed in the images is a consequence of a wide FOV imager, which is known to result in more substantial distortion at the image periphery.

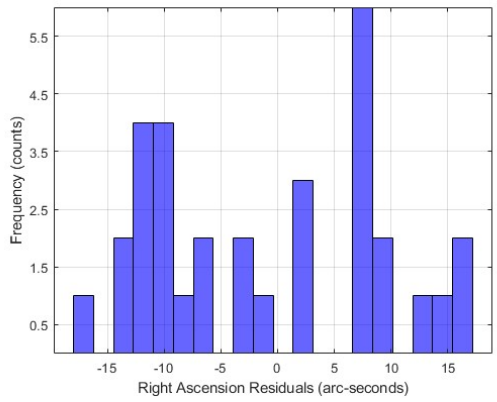

Figure 18: Residual errors in Right Ascension (RA)

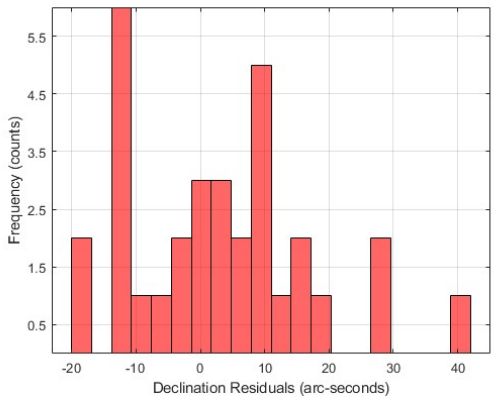

Figure 19: Residual errors in Declination (Dec)

3.4.3 Photometric Residuals

Figure 21 illustrates the regression analysis performed on the observed stars, displaying a best-fit line with a slope of 0.7160. This value signifies the rate at which instrumental magnitudes correlate relative to the catalogue magnitudes throughout the mission. At zero instrumental magnitude, the catalogue magnitude is approximated to 7.94, as indicated by the y-intercept. The root mean square

(RMS) error of 0.5796 quantifies the average magnitude deviation between the instrumental and catalogue values. These variations could be attributed to a number of factors, including a gradual increase in sky brightness during the mission, instrumental sensitivity, and fluctuations in gondola movement. Consequently, the best-fit line serves as a tool for photometric calibration, within an uncertainty of 0.58 magnitudes.

Figure 20 provides a comprehensive survey covering a broad range of stellar magnitudes, with the majority of stars having low SNR during their first observation using Equation 6. Stars with higher initial SNR values are likely more detectable and analyzable in subsequent observations, making them candidates for prioritized study as it was in our case, where the neighbouring mission's objective during the flight was to image bright stars. The mean SNR is relatively low at 2.14, indicating that many observations are close to the noise level. Some observations with very high SNRs (up to 21) suggest the presence of particularly bright stars or optimal observation conditions. The majority of SNR values are below 2.17, as shown by the 75th percentile.

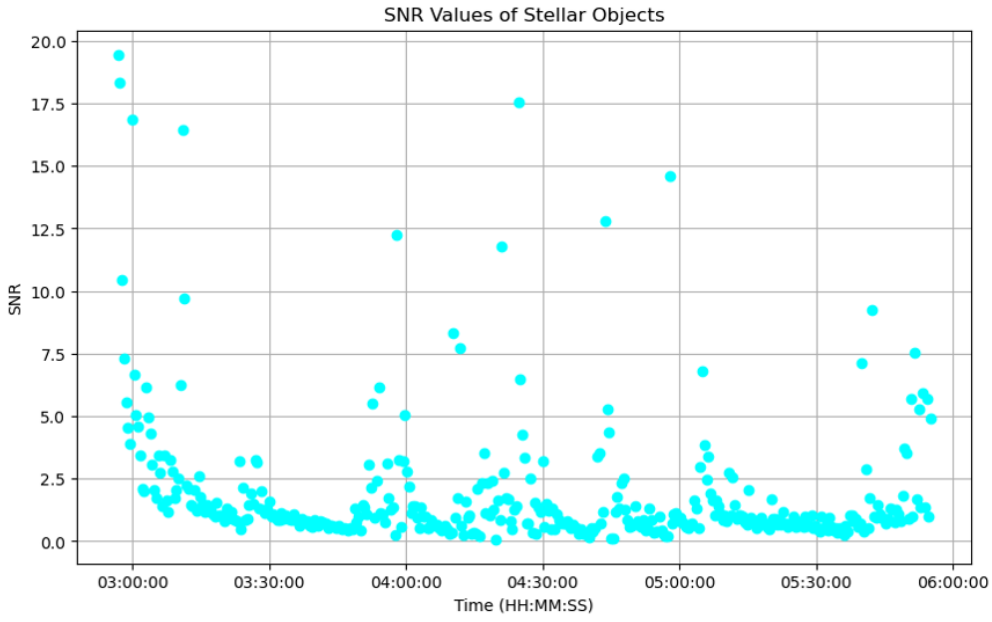

Figure 20: Plots represent the Signal-to-Noise Ratio of the observed stellar objects. The SNR is a measure of the strength of the signal (from the stars) relative to the background noise.

Table 8 presents 14 distinct RSOs monitored over a 6-minute interval starting at 04:26 am. The table provides details of the duration of observation, angular velocities, mean SNR, and FWHM

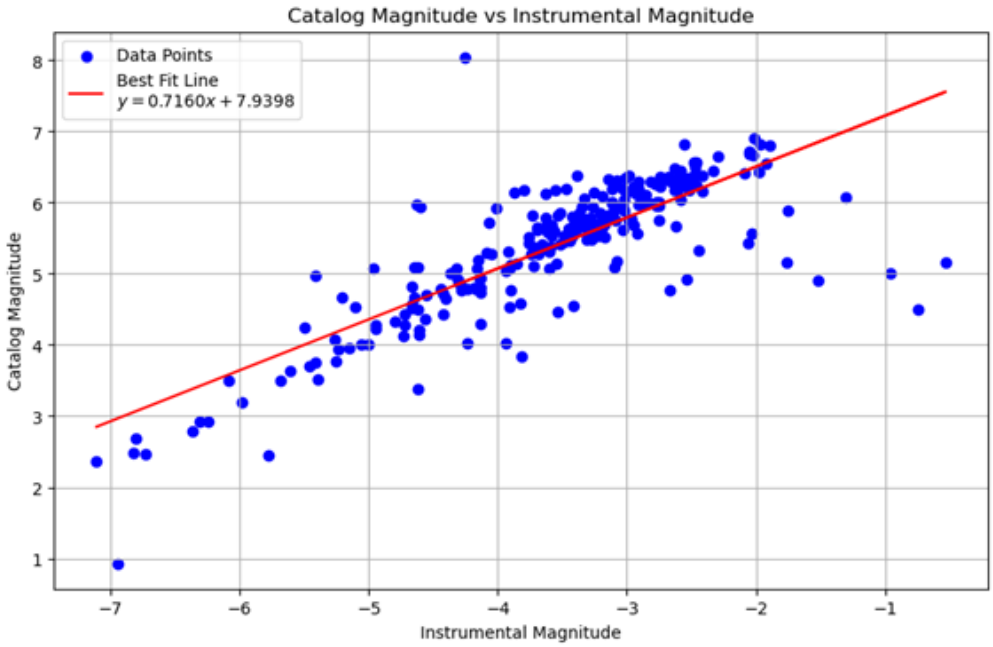

Figure 21: Plots V magnitude from the TYCHO-2 Catalogue against instrumental magnitude with data points in blue and the best fit line in red. The best-fit line's equation, y = 0.7160x + 7.9398, relates V magnitude to instrumental magnitude derived from aperture photometry.

values for each RSO. The angular velocity among the RSOs varied substantially, with a range from 886.48 to 2345.24 arcseconds per second. The duration of observation for individual RSOs spanned from a minimum of 10 seconds (RSOs 5 and 9) to a maximum of 105 seconds (RSO 4), a factor influenced by each RSO's velocity, trajectory, and the observer's FOV. In particular, RSOs 11 and 13 exhibited high mean SNR values (21.48 and 17.13, respectively), validating the presence of strong and highly detectable RSOs. In contrast, RSOs 3, 5, and 9 presented lower SNR values (below 8), indicating less distinct observations. However, these observations still surpassed the SNR of most stars. FWHM values remained within a narrow range of 4.54 to 5.49, reflecting consistent image resolution throughout the observations. The manual observations also demonstrate that high angular velocities do not preclude high SNRs, indicating that swift RSOs can be detected clearly under appropriate conditions. Furthermore, RSO 14 is exceptional for its extremely high SNR, hinting at a variable intrinsic luminosity. For effective tracking and characterization of RSOs, a higher SNR is advantageous. Conversely, a lower FWHM is typically sought after for finer resolution, though it tends to be larger than that of fixed celestial sources. The astrometric and photometric

data provided by these RSO observations contribute valuable information for the analysis of RSO behaviour and observation quality, indicating that RSOs with higher SNR and lower FWHM would be prime candidates for precise monitoring and study.

Table 8: The 14 distinct RSOs imaged over a 6-minute period, with varying angular velocity, SNR, and FWHM.

RSO ID	Observed Period (Seconds)	Angular Velocity (Arcseconds / Seconds)	Mean SNR	Mean FWHM	Mean Corrected Magnitude
1	79	1256.87	20.8	4.97	10.95
2	63	1010.97	8.94	4.88	12.78
3	68	886.48	7.76	4.85	13.09
4	105	947.25	13.75	5.01	11.84
5	10	1205.71	6.47	4.54	13.84
6	11	1054.58	8.27	5.29	12.95
7	28	1918.13	13.96	5.23	11.81
8	20	1333.21	13.24	5.49	11.93
9	10	1027.28	5.17	4.61	13.97
10	26	2345.24	15.69	5.43	11.56
11	32	1782.20	21.48	4.69	10.88
12	22	1601.67	13.17	5.15	11.94
13	50	2234.27	17.13	5.11	11.37
14	12	1913.28	55.75	5.23	8.8

3.4.4 Attitude Determination

In Figure 22, the attitude values are expressed in degrees for a XYZ rotation in the Earth-Centered Inertial (ECI) frame and in accordance with the intrinsic, active, and right-hand rule (RHR) conventions for rotation, as determined by Astrometry.net. This figure pertains to the optical payload of the RSONAR. The yaw (blue), indicative of the optical payload's right ascension, exhibits a steady increase over time, signifying consistent azimuthal rotation and movement. This increment reflects deliberate adjustments to the sensor's orientation in the horizontal plane for stabilized imaging. The pitch (yellow), represented as the negative declination, shows relative stability with minimal fluctuations, indicating that the payload's elevation angle—its position above or below the celestial equator—remained constant. The observed variability arises from corrective pointing maneuvers and inherent gondola movements. The roll (green), which delineates the orientation east of north,

demonstrates greater variability, due to abrupt alterations in the payload's banking angle. These fluctuations in roll may be attributed to a range of operational factors, including stabilization adjustments or external disturbances such as wind speeds. Consequently, we were able to demonstrate the primary objective of attitude determination with the images acquired from a dual-purpose star tracker for SSA.

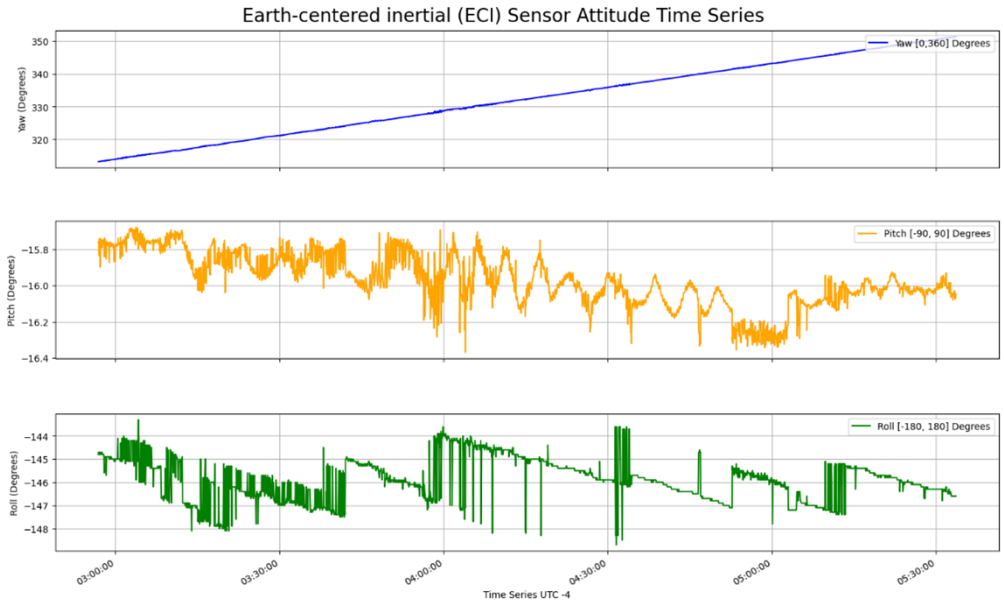

Figure 22: A time series of the Euler angles—yaw (blue), pitch(yellow), and roll(green) —for RSONAR's optical payload throughout the stabilized pointing period of the flight.

3.4.5 RSO Detection

The observation period, spanning from 2:56 am to 3:26 am, yielded six sequences with RSO presences identified by the RSO image classifier. This was followed by a period from 3:26 am to 3:56 am where no RSO presences were recorded. The subsequent periods exhibited a significant increase in the number of sequences detected, with 28, 29, and 28 sequences of RSOs observed. The observable increase and consistent presence of RSOs can be attributed to the beginning of the astronomical dawn. In particular, during the brief span from 5:26 am to 5:33 am, 14 sequences were still discernible. Overall, across all observation periods, there were 105 sequences with RSO presences identified.

As detailed in Table 9, an overview of the detected streaks from the RSO streak detection algorithm is provided, with both the mean streak length in arcseconds and the mean signal-to-background ratio for the streaks identified throughout the observation intervals quantified. A total of 387 RSO streaks were observed. The least amount of streaks and shortest mean streak length were observed during the period between 3:26 am and 3:56 am. The number of streaks increased from the start of the astronomical dawn period, which also coincided with an increase in the mean streak length, rising to 4679.19 arcseconds between 4:56 am and 5:26 am. Concurrently, the mean signal-to-background ratio declined as the morning sky brightened, leading up to dawn, diminishing the contrast between the streaks and the celestial backdrop. This shift in the visibility of RSOs implies the necessity of implementing adaptive strategies to maintain the effectiveness of RSO tracking throughout varying light conditions.

Table 9: The detected RSOs streaks and their properties across the observation periods

Observation Period	Number of Streaks	Mean Streak Length (Arcseconds)	Mean SNR
2:56 am - 3:26 am	65	2036.47	18.51
3:26 am - 3:56 am	6	2981.9	18.74
3:56 am - 4:26 am	76	3413.58	18.4
4:26 am - 4:56 am	110	4215.95	18.76
4:56 am - 5:26 am	86	4679.19	17.44
5:26 am - 5:33 am	44	4265.96	17.57
Total RSO Detections	387	3781.81	18.22

As tabulated in Table 10, the object detection algorithms exhibited varying efficacy. PFT registered the highest number of RSOs, with a total of 22,036, which is greater than the 18,566 and 9,194 detections made by AFD and MFD, respectively. This aligns with PFT's superior F1 score of 82%. A substantial increase in RSO detections was observed across all methods between 3:56 am and the conclusion of the observation periods. Of particular note is the interval between 3:56 am and 4:26 am, wherein MFD and PFT detected a greater number of RSOs than AFD, with the latter's counts exhibiting a notable disparity. During this period of high density, the precision and recall advantages of MFD and PFT were particularly pronounced. As with previous detection methods,

the lowest number of detections was observed during the period from 3:26 am to 3:56 am.

Table 10: The number of RSO detections recorded by each object detection algorithm—(AFD), (MFD), and (PFT).

Observation Period	AFD	MFD	PFT
2:56 am - 3:26 am	1373	369	527
3:26 am - 3:56 am	1094	308	440
3:56 am - 4:26 am	2272	2557	3500
4:26 am - 4:56 am	5808	2866	7849
4:56 am - 5:26 am	6088	2431	7260
5:26 am - 5:33 am	1931	663	2460
Total RSO Detections	18566	9194	22036

The results of RSO detection indicate that as the observation period extends into the early dawn, the number of RSO detections increases. Consequently, the commencement of astronomical twilight emerges as an optimal window for RSO observation, offering optimal phase angles between the sun, RSOs, and the observer for maximum detection efficiency. The periods prior to astronomical twilight yielded lower RSO detections across all methods, with the lowest numbers observed between 3:26 am and 3:56 am. Consequently, the results from the detection methods successfully demonstrate the secondary aspect of RSO detection for a dual-purpose ST for SSA.

3.5 Conclusion

In conclusion, the concept of a dual-purpose ST for SSA has been successfully demonstrated using images from the 2022 RSONAR Stratos campaign. The performance of the low-cost, commercial off-the-shelf dual-purpose ST was evaluated for its ability in attitude determination and RSO imaging. Photometric assessments of stars and RSOs were conducted utilizing FWHM and SNR as metrics. Astrometric assessment was conducted using Astrometry.net to extract the attitude of stars from the image and to determine residuals in RA and Dec of the stars. Through manual inspection, we identified a diverse array of over 500 RSOs, including the sample of 14 distinct RSOs annotated within a six-minute period that displayed magnitudes and SNRs as low as 13.97 and 5.17, respectively. These results demonstrate that a commercial star tracker can be used as a dual-purpose SSA

payload. Secondly, 27,027 images were acquired, each with carefully annotated information, for the purpose of current and future SSA research. These images were used to develop SSA algorithms such as PFT, which detected 22,036 RSOs with high-performance values for the detection algorithms and streak detection, which identified 387 streaks from this dataset. Finally, we have demonstrated that stratospheric observation represents an alternative to space-based or ground-based SSA, stemming from the enriched nature of this dataset and the need for further exploration. The dataset features a high density of RSOs with diverse characteristics, which will significantly benefit the development and validation of RSO detection. Therefore, we intend to publish the SSA datasets obtained from the Stratospheric Platform, ensuring they are readily available for broader research and application.

3.5.1 Future Work

In order to enhance the use of the stratosphere as a platform for SSA observations, additional flights must be conducted with varying imagers. Moreover, to validate the observations for SSA, it is necessary to conduct multi-site observations, where the instruments capture the same celestial regions from both ground-based locations and stratospheric flight. These comparisons will enable the direct discrimination of observational data to discern the unique advantages or limitations presented by the stratospheric vantage point. Future studies will also focus on extracting light curves from RSOs of interest to gain information about their characteristics and orbital properties. Furthermore, we plan to identify the RSOs by correlating detections with the existing catalogue of RSO Two Line Elements (TLE). This cross-referencing can verify the accuracy of our observations and potentially contribute to the refinement of the TLE database.

4 RSO Streak Analysis in Wide Field of View Imager Stratospheric Dataset

This chapter is on the study that explores several key aspects of RSO streak detection and analysis for SSA applications. The research presented herein focuses on the empirical characterization of Resident Space Objects (RSOs), utilizing data captured during a stratospheric flight campaign. The research contributions include the development of high-accuracy annotations for RSO streaks, bench-marking streak detection algorithms, and integrating image quality metrics to enhance the robustness of detection methods. Given the absence of publicly available annotated datasets in SSA, this study addresses a significant gap by providing manually curated annotations of satellite streaks, which will be made publicly available to support the broader SSA community. These annotations serve as a critical foundation for the validation and development of detection algorithms. The comparative analysis of the ASTRiDE and SD algorithms provides insights into their respective strengths and weaknesses, offering a basis for selecting or refining algorithms based on specific SSA applications.

This research also incorporates advanced image quality assessments using metrics such as the Structural Similarity Index Metric (SSIM), the Peak Signal-to-Noise Ratio (PSNR), and the Learned Perceptual Image Patch Similarity (LPSIS), ensuring that the detection algorithms are not only accurate but also resilient to various observational conditions. The findings contribute to a more nuanced understanding of RSO streak characteristics and offer data-driven insights that are essential for improving satellite path prediction, understanding orbital dynamics, and mitigating potential collisions.

I was responsible for conducting the analysis, developing the 544-streak image benchmark with annotations, and implementing the comparative study of the streak detection algorithms. I also integrated the image quality metrics into the study. I prepared all the figures and tables and wrote the manuscript. Regina Lee provided invaluable guidance throughout the research process, and all coauthors contributed with feedback and revisions to the manuscript.

4.1 Introduction

The identification of streaks in astronomical imagery has historically focused on detecting asteroids and meteoroids using ground-based telescopes with narrow fields of view. However, the exponential growth of the Resident Space Objects (RSOs) population, driven by the commercialization and miniaturization of space technology, has introduced new challenges in Space Situational Awareness (SSA). Satellite launches have become significantly more frequent due to the affordability and availability of services provided by launch providers such as SpaceX and Rocket Lab. Additionally, the deployment of commercial mega-constellations, along with satellite fragmentations from collisions and anti-satellite tests, has further exacerbated the growth of the RSO population.

The increasing number of RSOs elevates the risk of collisions, potentially leading to a catastrophic cascade effect known as the Kessler Syndrome, where collisions between objects trigger a chain reaction of further collisions. Consequently, continuous monitoring, analysis, and cataloging of RSOs are critical for effective Space Situational Awareness (SSA). SSA is driven by several factors, including national security, international diplomacy, commercial interests, and strategic competition in space. However, the sensitivity of SSA data has limited the availability of publicly annotated datasets, leading most research to rely on simulated or synthetic data, which hinders the replication and democratization of SSA applications. This chapter addresses these challenges by analyzing RSO streaks captured in wide-field-of-view imager datasets from a stratospheric flight campaign [54]. The analysis focuses on enhancing SSA through the characterization of streak properties such as length, orientation, Signal-to-Noise Ratio (SNR), and Full Width Half Maximum (FWHM). Additionally, the chapter explores clustering techniques, image quality assessment metrics, and the performance of streak detection algorithms.

The subsequent sections of this chapter are organized as follows: Section 4.2 introduces the dataset, emphasizing the importance of accurate manual annotations. Section 4.3 details the methodology of obtaining streak properties and the application of clustering and image quality metrics. In addition to introducing and comparing the ASTRiDE and the Streak Detection (SD) algorithms for

streak detection. Section 4.4 presents the results of the descriptive statistics, temporal analysis, and algorithm performance evaluations. Finally, Section 4.5 summarizes the key findings, discusses their implications for SSA, and offers recommendations for future research, including the potential for cluster-based classification and the refinement of detection algorithms.

4.1.1 Research Contributions

This chapter makes significant contributions to the field of SSA through the comprehensive analysis of RSO streaks captured during a stratospheric flight. The primary contributions include:

1. **RSO Streak Characterization :** A detailed empirical analysis was conducted on 544 manually annotated streaks from 66,049 images (257 stacked image sequences). The study examined properties such as length, orientation, SNR, and FWHM, providing essential insights into RSO streak behavior. These insights aid in distinguishing between different types of RSOs and developing RSO identification.

2. **RSO Streak Annotations:** This work provides 544 RSO streak annotations, serving as a ground truth for algorithm development and validation. These annotations are crucial for understanding streak properties and training detection algorithms. To further support the SSA community and address data limitations, these annotations will be made publicly available upon request, offering a valuable resource for the development and refinement of SSA technologies.

3. **Benchmarking Streak Detection:** Another key contribution is the comparative analysis between the open-source ASTRiDE algorithm, a widely recognized benchmark in streak detection, and the SD algorithm. By identifying the relative merits and shortcomings of each algorithm, this research contributes to the development of more accurate and effective detection methods, which are vital for SSA applications.

4. **Variability with RSO Streaks:** The integration of image quality metrics (SSIM, PSNR, LPIPS) adds a nuanced understanding of RSO streaks dataset, ensuring that the developed

algorithms are robust and capable of handling various observational scenarios.

4.2 Dataset

4.2.1 Literature Review

A variety of observations have been conducted by researchers to acquire datasets for SSA. The internally curated datasets exhibit significant variability due to the diverse range of instrumental configurations. Table 11 presents selected studies that have utilized streaks from datasets obtained through ground-based optical telescopes with narrow fields of view (FOVs). Additionally, simulated streak datasets have been used in studies such as [74], where the SkyMaker application was employed. Some studies have utilized semi-synthetic datasets, combining authentic ground-based images with simulated streaks, as seen in [75, 44], to assess algorithms under more realistic conditions. Moreover, real datasets from the Space-Based Telescopes for Actionable Refinement of Ephemeris (STARE), an SSA nanosatellite project, were employed in [76].The stratospheric-based wide-field-of-view dataset presented in this study is novel within the SSA field and warrants further assessment to understand the RSOs present and explore new alternatives for SSA data acquisition.

Table 11: Ground-Based Observational Sites and Exposure Rates

Location	**Exposure Rate (seconds)**	
New Mexico, United States of America	0.10	[77]
Kiso, Japan	0.50	[78]
Stuttgart, Germany	1.00	[79]
Australia Remote Observatory (ARO), Australia	3.00	[80]
Feleacu and Marisel, Portugal	5.00	[81]
Nantou County, Taiwan & Adelaide, Australia	5.90 & 5.00	[82]

Citizen science initiatives, such as NASA's Satellite Streak Watcher and Hubble Asteroid Hunters, have provided publicly accessible datasets to which volunteers contribute by uploading images and providing annotations [83, 84]. The Kelvins SpotGEO Challenge [85], created by the Advanced Concepts Team of the European Space Agency and the University of Adelaide, was designed with the specific objective of exploring the detectability of GEO satellites from low-cost ground-based

imagery. The training and test datasets were provided to participants for the purpose of developing and validating detection methods. Since that time, this dataset has served as a catalyst for the development of several algorithms [86, 87].

4.2.2 Dataset from 2022 RSONAR flight

A total of 6,939 images (257 stacked image sequences) were analyzed in this study. These images were captured between 4:56 am and 5:33 am during the RSONAR flight, with the solar elevation angle ranging from -1.75° to 3.00° in the region of Timmins, Ontario. The imaging covered celestial coordinates between Right Ascension 343.13° to 351.43° and Declination -16.33° to -15.92°.

The quality of these stacked images, which are essential for rendering streaks, was affected by turbulence experienced during the flight. This turbulence introduced noise into the data, potentially impacting the accuracy of the streaks. To address this, a Lomb-Scargle periodogram [88] was employed to identify and quantify periodic signals in the gondola's orientation, such as yaw, pitch, and roll. This frequency analysis method helps in understanding the impact of turbulence on the data by detecting dominant frequency components associated with flight oscillations.

As illustrated in Figure 23, the Lomb-Scargle periodograms of the Euler angles reveal peaks at 0.5×10^{-3} Hz, corresponding to the control system's maintenance of the flight's pointing accuracy. Additionally, peaks at approximately 0.1 Hz and $0.5 - 0.6$ Hz in the pitch and roll measurements suggest that wind or corrective maneuvers caused the gondola to oscillate. By identifying these frequencies, we can better assess the extent of turbulence and its effects on the dataset, enabling more accurate analysis of the streaks.

4.2.3 Annotation Procedure

The dataset was annotated using AstroImageJ [56], a software tool designed for astronomical image processing based on ImageJ. AstroImageJ facilitates the display of astronomical images and provides tools for image calibration and annotation. The sequence of images for annotation was

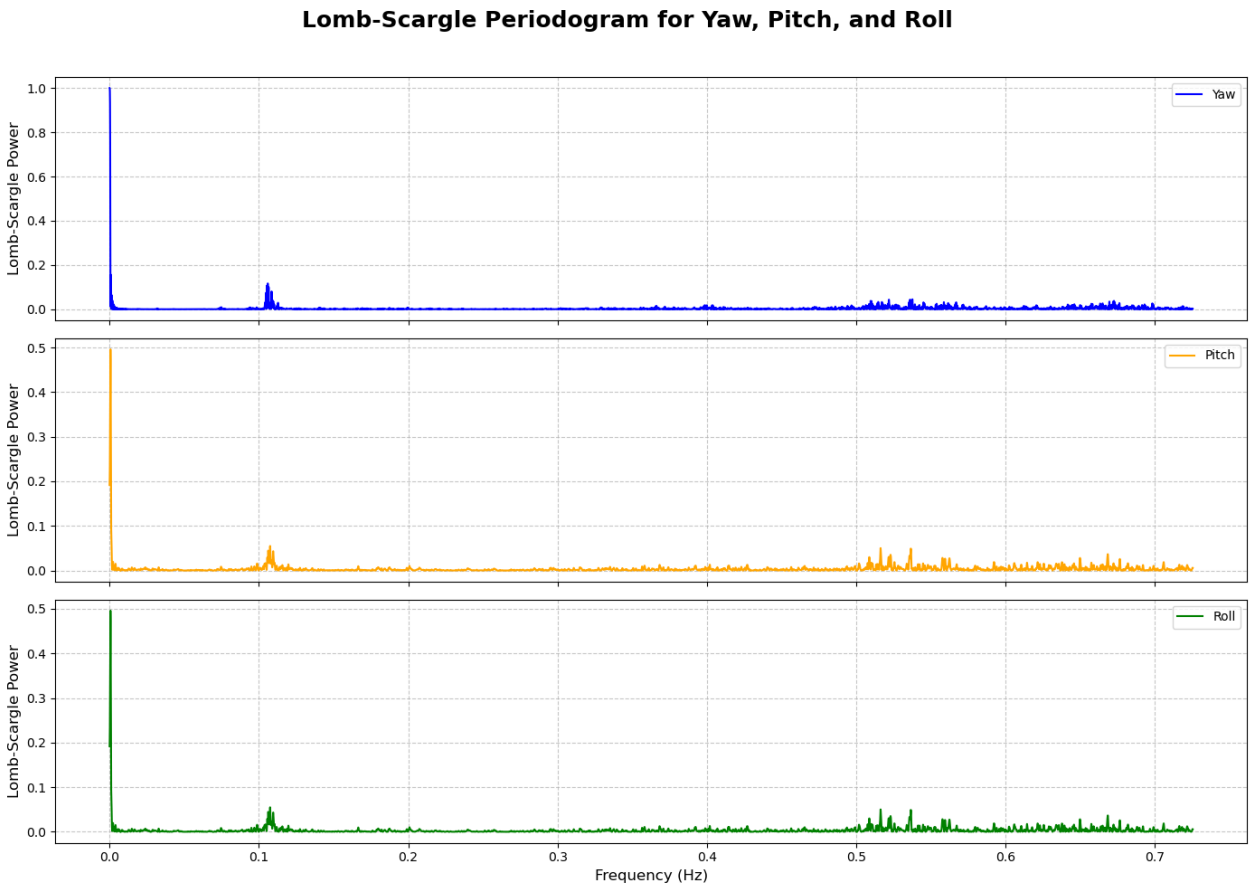

Figure 23: Lomb-Scargle Periodogram for Yaw, Pitch, and Roll showing the frequency components of each attitude parameter. The power spectrum highlights dominant frequencies corresponding to periodic oscillations in the yaw, pitch, and roll angles.

imported into AstroImageJ for processing. The annotation process was arduous and conducted with precision by a trained annotator well-versed in the dataset, capable of discerning RSO streaks from celestial elements and artifacts. Prior to commencing the annotation process, the annotator undertook a detailed examination of the trajectories of the RSOs within the dataset. Their task was to annotate the satellite streaks from the point of entry to the point of exit from the sensor's field of view.

To ensure precision, the adjustable histogram for thresholding images, as provided by AstroImageJ, was utilized in sequences where lighting conditions exhibited fluctuations. This approach facilitated the detection and annotation of streaks with lower signal-to-noise ratios (SNR). The annotation tool provided precise control over the pixel radius, with streaks annotated via a click-and-

drag function to create vectors based on the streak endpoints. These annotations were indispensable for subsequent analysis of the streak's properties, including length, orientation, signal-to-noise ratio (SNR), and full width at half maximum (FWHM) of the streaks. The quality of the streaks was evaluated using three metrics: the Structural Similarity Index Metric (SSIM), the Peak Signal-to-Noise Ratio (PSNR), and the Learned Perceptual Image Patch Similarity (LPSIS). A total of 544 streaks were annotated, thereby providing a basis for evaluating the performance of streak detection algorithms.

The annotated endpoints of the streaks represent the coordinates of two opposite corners of a rectangle that delineates the region of interest (ROI) in each image. To ensure that no portion of the pertinent feature is inadvertently excluded during cropping, a five-pixel margin is added around the ROI. Furthermore, this methodology accounts for potential human error that may have occurred during the annotation process. This is of particular significance when the feature in question is situated in close proximity to the periphery of the bounding box and may extend slightly beyond the initial ROI.The margin was meticulously calibrated to guarantee that the cropped region remained within the original image dimensions. Subsequently, the streaks are effectively isolated and saved as new image files.

4.3 Methodology

4.3.1 Streak properties

Length : The length of the streak was calculated by determining the Euclidean distance between its endpoints, as defined by the following equation 8 :

$$\text{Distance (pixels)} = \sqrt{(X_2 - X_1)^2 + (Y_2 - Y_1)^2} \tag{8}$$

where (X_1, Y_1) and (X_2, Y_2) represent the coordinates of the streak's endpoints in the image plane.

Orientation : The orientation of a Resident Space Object (RSO) is essential for identifying and characterizing its orbit. When the physical dimensions and mass of an RSO are known, changes

in its orientation over time can be analyzed to estimate its spin rate. This spin rate is a critical factor in assessing the RSO's stability and can be used to determine its object type, such as a rocket body, active satellite, tumbling satellite, or debris fragment. The orientation of the RSO streak was calculated using the following formula 9 :

$$\theta(degrees) = \arctan\left(\frac{Y_2 - Y_1}{X_2 - X_1}\right) \tag{9}$$

where θ represents the angle of orientation in degrees, and (X_1, Y_1) and (X_2, Y_2) are the coordinates of the streak's endpoints in the image plane. The angle θ was then converted from radians to degrees to facilitate analysis.

Signal-to-Noise Ratio (SNR) : The segmented streak images were evaluated for their signal-to-noise ratio (SNR) using the following equation 10 :

$$\text{SNR} = \frac{\mu}{\sigma} \tag{10}$$

where μ represents the mean signal of the image and σ represents the standard deviation of the pixel values in the image, which is used as a measure of noise.

Full Width Half Maximum (FWHM) : Binarized masks were created using adaptive thresholding, which isolated the brightest areas of the image as the features of interest. To ensure rigorous thresholding, the sensitivity of the binarization algorithm was deliberately reduced, capturing solely the brightest regions as the foreground. Element-wise multiplication of the binary mask with the original image isolated the pixels corresponding to the streak, effectively zeroing out all other pixels. Subsequently, the intensity profile of the streak was then computed by summing the pixel values along its length. The maximum intensity and its corresponding position were identified, followed by calculating the half-maximum level. The FWHM was determined by measuring the distance between the first and last indices where the intensity profile meets or exceeds this threshold.

Clustering : Clustering is a robust technique for organizing data points into groups based on their inherent similarities. In this study, K-Means clustering [89] was selected as the most appropriate

methodology for the analysis of RSO streak data. To ensure that each feature of the RSO streaks contributed equally to the distance calculations in K-Means clustering , the data was scaled prior to clustering. The optimal number of clusters was determined to be five based on the Silhouette Score [90], and this value was subsequently used to partition the data.

4.3.2 Image Quality Assessment Metrics

The perceptual quality of the streak was evaluated using a range of image quality assessment metrics, necessitating that all images be standardized to the same dimensions. To achieve this, the images were resized with padding, thereby preserving the intrinsic characteristics of the streaks. In this chapter, we employ full-reference approaches, where the quality of a given streak image is assessed relative to a reference streak image. The evaluation techniques include the Structural Similarity Index Measure (SSIM), the Peak Signal-to-Noise Ratio (PSNR), and the Learned Perceptual Image Patch Similarity (LPIPS) metric.

SSIM is an image quality assessment metric that quantifies the similarity between two images by evaluating luminance, contrast, and structural information [91]. PSNR, derived from the Mean Squared Error (MSE), measures the average of the squared differences between the images and is expressed in decibels (dB) [91]. Both SSIM and PSNR values were calculated using MATLAB's built-in ssim and psnr functions from the Image Processing Toolbox.

The LPIPS metric [92] evaluates perceptual similarity between images by leveraging the activations derived from pre-trained convolutional networks. In particular, architectures such as AlexNet, SqueezeNet, and VGG employed to extract features for this assessment. Consequently, LPIPS exhibits a high degree of alignment with human perception, even in the presence of complex environments like the streaks in our dataset.

4.3.3 ASTRiDE (Automated Streak Detection for Astronomical Images)

ASTRiDE is an open-source algorithm designed for detecting hypervelocity objects [93], and it has been widely adopted by researchers in SSA applications [94, 95, 96]. The algorithm begins by

eliminating the background from images, then applies morphological operations to the remaining objects to differentiate streaks. After processing, ASTRiDE outputs the endpoints, centroids, and areas of the streaks. Key morphological parameters used in this process include circularity, radius deviation, and area. In our dataset, stars, which are point-like sources with circular morphology, typically exhibit circularity and radius deviation values close to 1 and 0, respectively. Consequently, default thresholds of 0.2 for circularity and 0.5 for radius deviation are applied to distinguish streaks from these stellar objects. As discussed in 3, the mean FWHM value for the stars in our dataset is 3.67, corresponding to an estimated mean area of less than 10 pixels, which is below ASTRiDE's default area threshold that targets objects exceeding 10 pixels.

To evaluate ASTRiDE's performance, it is benchmarked against the streak detection algorithm described in Chapters 2 and 3 using the annotated RSO streaks. The effectiveness of these methodologies is assessed through mean squared error (MSE) and mean absolute error (MAE), calculated based on the coordinates of the streaks identified by each algorithm which turned out to be True positives. Additionally, the lengths of the detected streaks are compared with their corresponding annotated values.

4.4 Results

4.4.1 Streak Properties

Statistics of RSO Streaks

Table 12 summarize the descriptive statistics for the key parameters analyzed in the RSO streaks, including length (in pixels), orientation (in radians), SNR, and FWHM (in pixels). The streak length, measured as the Euclidean distance between annotated endpoints, has a mean of 50.27 pixels with a standard deviation of 23.76 pixels. There is a symmetric distribution within the streaks due median value of 49.23 pixels closely aligns with the mean. The Streak Lengths range from 6.94 to 115.10 pixels, with most streaks falling within the interquartile range (IQR) of 31.08 to 67.30 pixels. Outliers extending beyond 100 pixels represent high-speed Low Earth Orbit (LEO)

objects, further emphasizing the dataset's diversity.

Statistic	Length (Pixels)	Orientation (Radians)	SNR	FWHM (Pixels)
Mean	50.27	1.70	73.87	39.06
Std. Dev.	23.76	1.65	27.98	22.82
Min	6.94	-3.13	4.92	1.00
25th Percentile	31.08	1.69	60.82	22.00
Median (50th Percentile)	49.23	1.92	81.50	33.00
75th Percentile	67.30	2.97	92.24	54.00
Max	115.10	3.14	119.70	115.00

Table 12: Descriptive Statistics of Satellite Streaks

Streak orientation, calculated using the arctangent of the difference between the y and x coordinates of the endpoints, averages 1.70 radians with a standard deviation of 1.65 radians. The orientations span nearly the full range from -3.13 to 3.14 radians, reflecting RSOs entering the sensor's field of view (FOV) from all directions. The slight positive bias in orientation indicates a tendency for streaks to tilt rightward, which is crucial for analyzing the trajectories of RSOs in the dataset. These trajectories are primarily influenced by orbital characteristics rather than relative observer motion, given the relatively stationary observation angles.

The SNR analysis, performed on segmented images, reveals strong signal strength across the dataset, with an average of 73.87 and a standard deviation of 27.98. SNR values range from 4.92 to 119.70, with most streaks showing robust signals, as indicated by the IQR of 60.82 to 92.24, ensuring reliable detection. The FWHM, determined using binarized masks, shows considerable variability with a mean of 39.06 pixels and a standard deviation of 22.82 pixels. The FWHM ranges from 1 to 115 pixels, with most values falling within the IQR of 22 to 54 pixels. This variability reflects differences in the reflective properties of RSOs and their phase angles relative to the sun during imaging.

Temporal Analysis

Polynomial regression of degree 2 was applied to analyze trends in Length, SNR, and FWHM of the streaks over time, as illustrated in Figure 24. This regression effectively captures these trends

despite the dataset's high variability.

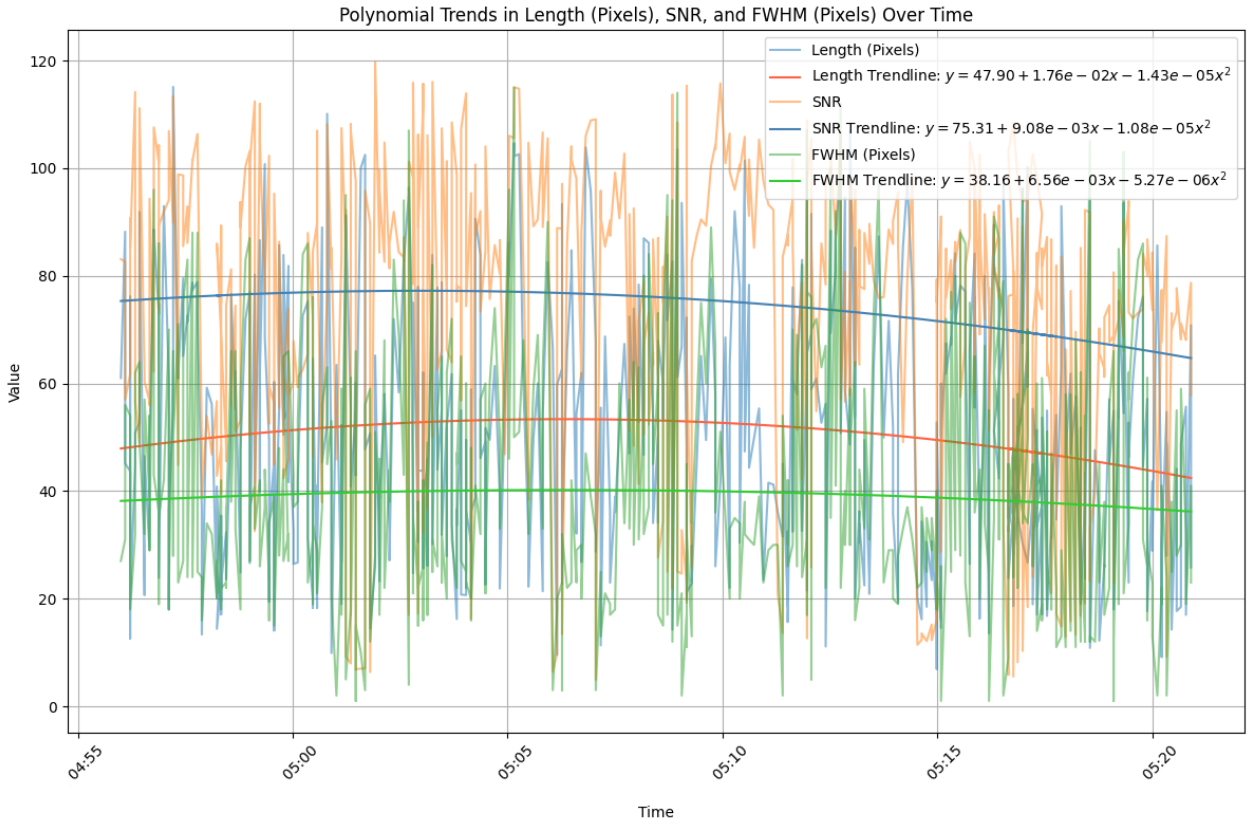

Figure 24: Trends in Length, SNR, and FWHM over time using degree-2 polynomial regression. The blue, orange, and green lines represent the trends for Length, SNR, and FWHM, respectively.

The temporal trends in length (blue line), SNR (orange line), FWHM (green line) are described by the following equations:

$$Length = 47.90 + 1.76 \times 10^{-2}x - 1.43 \times 10^{-5}x^2 \tag{11}$$

$$SNR = 75.31 + 9.08 \times 10^{-3}x - 1.08 \times 10^{-5}x^2 \tag{12}$$

$$FWHM = 38.16 + 6.56 \times 10^{-3}x - 5.27 \times 10^{-6}x^2 \tag{13}$$

This equation 11 indicates a minimal upward trend in streak length, with a slight downward bend

toward the end, implying consistent streak lengths throughout the observation period. The minor increase in length observed mid-period may result from improved observation conditions, such as rising solar elevation.The SNR (equation 12) shows a subtle increase over time, with a slight concave curvature, implying that RSOs became more visible as the observation period progressed, likely due to optimal phase angles. The plateau toward the end results from increased background sky noise as sunrise approached.This FWHM (equation 13) reveals a slight downward trend in FWHM over time, suggesting a nearly linear decrease in streak width as sunlight increased.

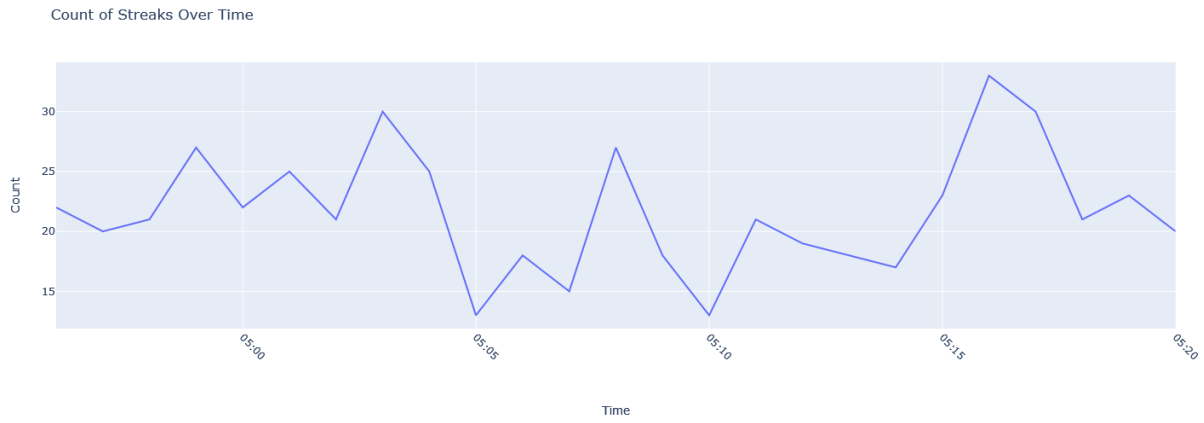

Figure 25: Temporal variation in the count of detected streaks. The plot illustrates fluctuations in the number of streaks over time, highlighting distinct peaks and troughs that correspond to changes in streaks.

The plot 25 illustrates the temporal variation in the presence of streak counts. The distinct peaks and troughs observed in the plot indicate periods of increased and decreased streak presence, due to variations in RSO density within the sensor's field of view (FOV). Peaks in streak count coincide with instances when multiple satellites are simultaneously visible. Subsequently, a reduction in the number of streaks is observed, resulting in a period of relative quiescence. The cyclical pattern of alternating peaks and troughs suggests that this periodic behavior may be associated with satellite orbital paths.

Correlation : Figure 26 presents a correlation matrix of streak features, depicting the relationships between Length, Orientation, SNR, and FWHM. The heatmap visually represents these relationships, with correlation coefficients indicating the strength and direction of the associations.

The strongest correlation is observed between Length and FWHM (0.42), indicating a moderate

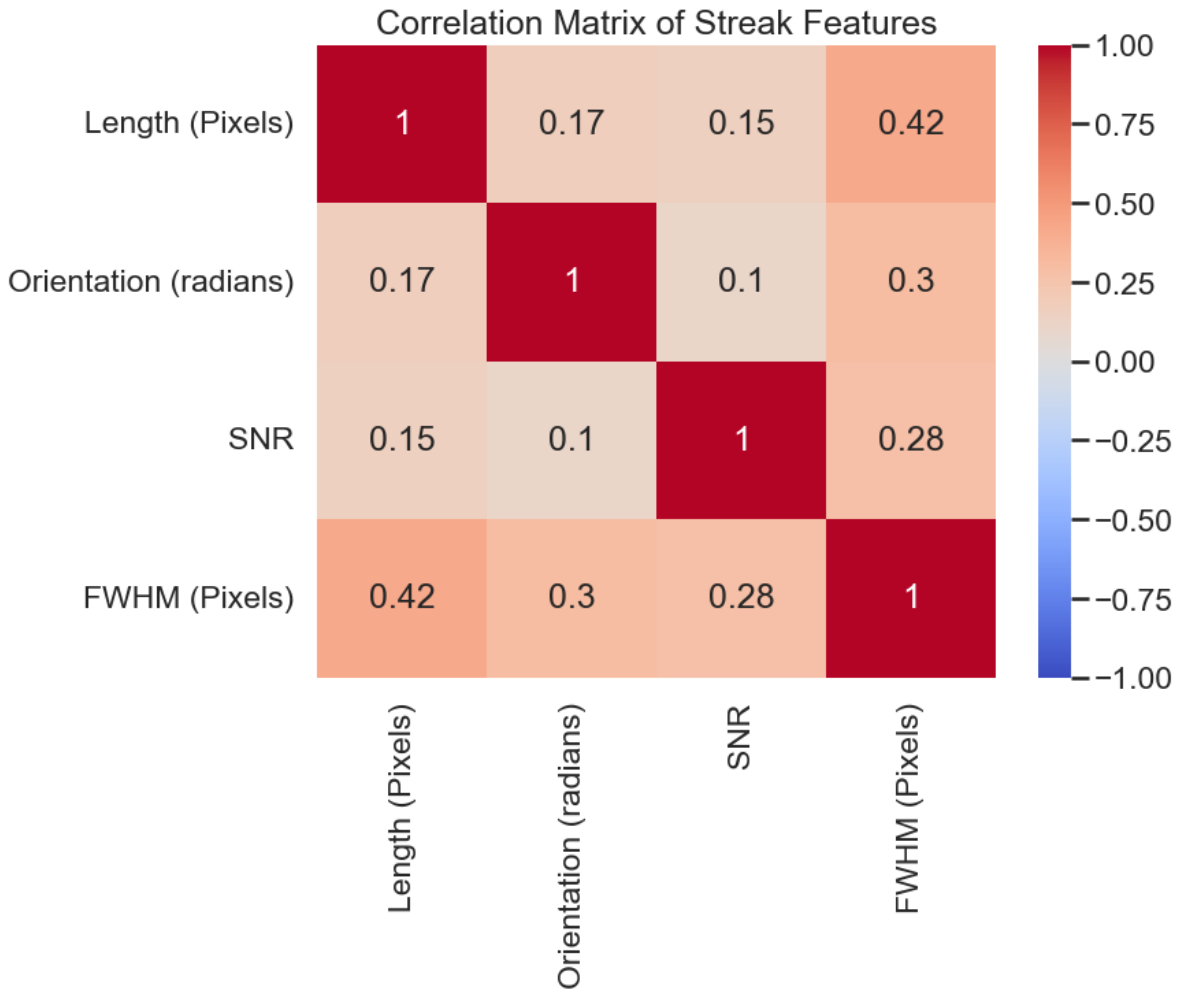

Figure 26: Correlation matrix of streak features, highlighting the relationships between Length, Orientation, SNR, and FWHM, with correlation coefficients indicating the strength and direction of these relationships.

positive relationship, as longer streaks generally correspond to larger FWHM values. A moderate correlation exists between FWHM and Orientation (0.3), suggesting that streaks with certain orientations tend to exhibit greater intensities. In contrast, the correlations between Length and Orientation (0.17) and between SNR and both Length (0.15) and FWHM (0.28) are relatively weak, showing that streak length is largely independent of orientation and that SNR has minimal influence on streak dimensions.The overall analysis of the correlation matrix reveals that most features in the dataset are relatively independent, highlighting the diverse range of RSO streaks present.

Cluster Analysis : Figure 27 visualizes the distinct patterns identified in the dataset through clustering based on streak properties. This analysis effectively differentiates between various groups of

RSO streaks, aiding in the classification of RSO types and their orbits.

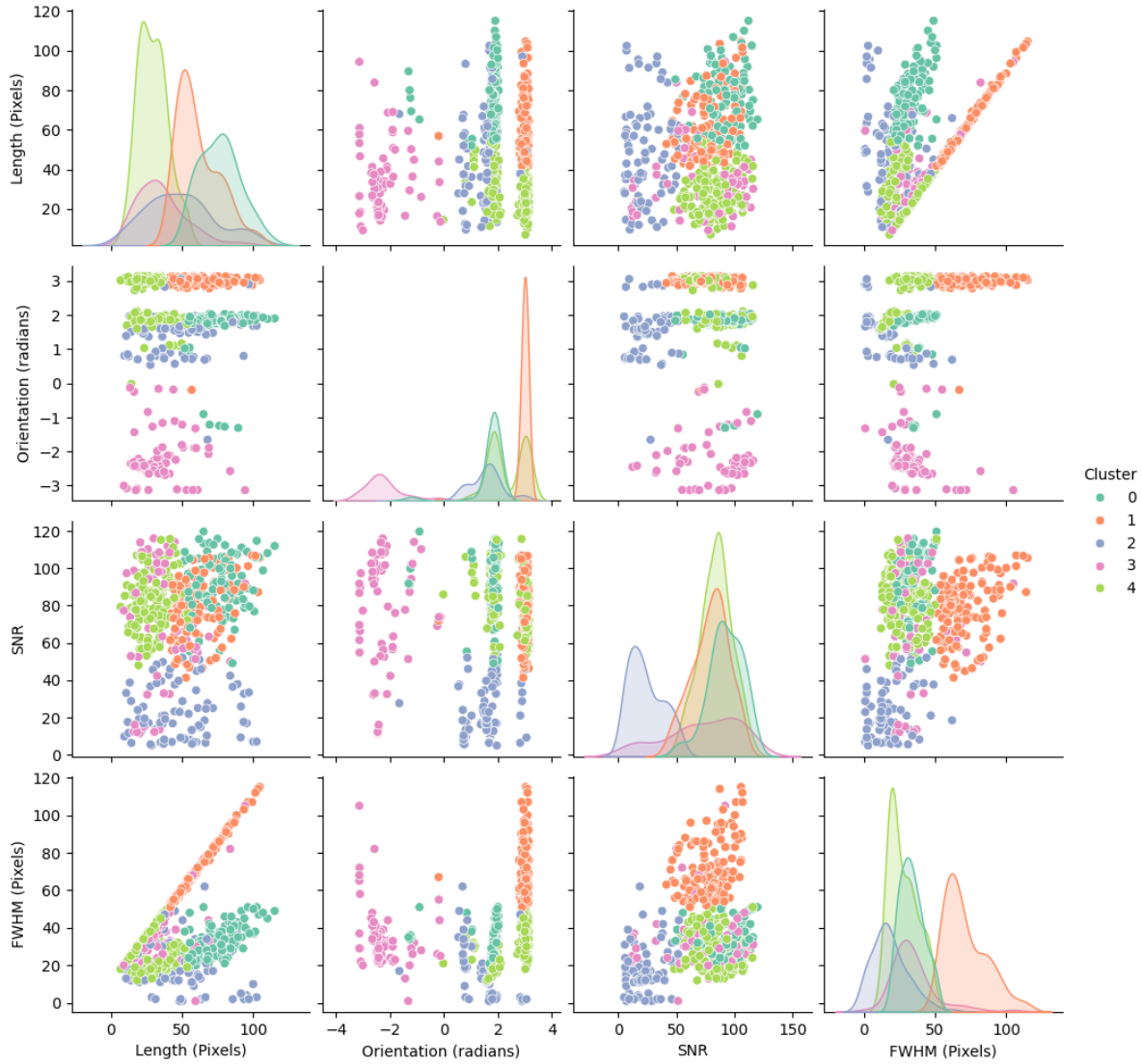

Figure 27: Clustering results visualized with the relationships between Length, Orientation, SNR, and FWHM. The colors represent the different clusters, highlighting distinct patterns in the dataset.

Cluster 0 (Teal/Green) contains long streaks with moderate orientation and high SNR, indicating well-detected but slightly diffuse streaks, likely due to low reflectivity of the RSO. Cluster 1 (Orange) also includes long streaks but with higher orientation angles, moderate SNR, and larger FWHM, suggesting closer or highly reflective RSOs with well-resolved streaks.Cluster 2 (Blue) is characterized by short, faint streaks with low SNR, likely representing smaller or more distant objects that are challenging to detect. Cluster 3 (Pink) features well-focused short streaks with

moderate visibility and a distinct leftward tilt, indicating RSOs are from similar orbits. Cluster 4 (Light Green) includes short streaks with high SNR, suggesting strong visibility despite their shorter lengths, likely from slow-moving, highly reflective RSOs.

4.4.2 Image Quality Assessment Metrics

SSIM, PSNR, and LPIPS models (Alex, Squeeze, VGG) were evaluated, with their key statistics presented in Table 13.

Table 13: Descriptive statistics for image quality metrics in the dataset.

Metric	Mean	Median	Std Dev	Min	Max	25th Percentile	75th Percentile
SSIM	0.618	0.543	0.202	0.096	1.000	0.465	0.820
PSNR (dB)	inf	3.747	NaN	0.526	inf	3.010	8.416
LPIPS (Alex)	0.391	0.466	0.146	0.000	0.610	0.294	0.500
LPIPS (Squeeze)	0.217	0.264	0.098	0.000	0.393	0.142	0.288
LPIPS (VGG)	0.284	0.339	0.124	0.000	0.537	0.185	0.374

The dataset exhibits a mean SSIM of 0.618, with values ranging between the 25th percentile (0.465) and the 75th percentile (0.820), indicating significant variation in structural quality. SSIM is particularly effective at identifying images with low structural integrity while also highlighting variability across the dataset. In contrast, PSNR shows a median of 3.747 dB with considerable variance and extreme outliers, suggesting that many images suffer from noise or degradation. PSNR's sensitivity to outliers and limited ability to capture perceptual quality makes it less reliable for this dataset.

For LPIPS models, AlexNet has a mean score of 0.391 and a median of 0.466, with tight clustering in the upper percentiles, indicating minimal perceptual differences once a certain quality level is achieved. LPIPS (Squeeze) exhibits a mean score of 0.217 and a median of 0.264,suggesting sensitivity to lower-quality images but less effectiveness in distinguishing higher-quality nuances. LPIPS (VGG) has a broader range of scores, making it more sensitive to perceptual differences across the dataset.

SSIM and LPIPS (VGG) provide the most consistent assessments, with SSIM excelling in evaluating structural integrity and LPIPS (VGG) offering a balanced view of perceptual quality. In

contrast, PSNR's sensitivity to outliers makes it less effective for diverse dataset like ours, suggesting SSIM and LPIPS (VGG) as the preferred metrics for applications requiring high structural and perceptual quality.

4.4.3 Performance Evaluation of Streak Detection Algorithms

Table 14 presents a comparative analysis of two streak detection algorithms, ASTRiDE and the SD algorithm, using various metrics across two streak length thresholds: $\geq$10 pixels and $\geq$ 17.5 pixels. The evaluation includes True Positives (TP), False Positives (FP), False Negatives (FN), Precision, Recall, F1 Score, and the number of detectable streaks. In this dataset, 32 streaks fall below the 17.5-pixel length threshold, and only 3 are below the 10-pixel threshold.

Table 14: Comparative analysis of ASTRiDE and SD streak detection algorithms at different length thresholds.

Metric	**ASTRiDE ($\geq$ 10 Pixels)**	**SD ($\geq$ 10 Pixels)**	**ASTRiDE ($\geq$ 17.5 Pixels)**	**SD ($\geq$ 17.5 Pixels)**
Detectable Streaks	541	541	512	512
True Positives (TP)	71	122	71	115
False Positives (FP)	14	193	14	13
False Negatives (FN)	470	419	441	397
Precision	84%	39%	84%	90%
Recall	13%	23%	14%	22%
F1 Score	23%	29%	24%	36%

The SD algorithm detects more true positives than ASTRiDE at both thresholds, indicating higher sensitivity, particularly at the 10-pixel threshold. However, this increased sensitivity also results in significantly more false positives at the 10-pixel threshold, suggesting that SD may over-detect non-existent streaks. This issue is reduced at the 17.5-pixel threshold, where SD's false positive rate drops considerably due to its area-based filtering. In contrast, ASTRiDE, which uses morphological filtering, maintains a consistent detection rate across both thresholds. Both algorithms exhibit high false negative rates, but SD consistently shows fewer false negatives than ASTRiDE, particularly at the higher threshold, indicating better overall detection. However, the persistent high false negative rates in both algorithms highlight potential limitations in handling complex sequences with multiple

streaks with varying SNR.

ASTRiDE maintains consistent precision across both thresholds. In contrast, SD's precision is lower at the 10-pixel threshold due to a higher false positive rate but improves significantly to 90% at the 17.5-pixel threshold, indicating more accurate detection of longer streaks. Recall, which measures the proportion of actual streaks correctly identified, is relatively low for both algorithms, though SD consistently outperforms ASTRiDE. The F1 Score, which balances precision and recall, is higher for SD at both thresholds, particularly at the 17.5-pixel threshold, indicating a better trade-off between detecting true streaks and minimizing false positives. ASTRiDE's lower but more stable F1 Score reflects its morphological approach, which reduces the likelihood of false positives but also results in fewer true positives.

Error Analysis in True Positives : Figure 28 compares the Mean Absolute Error (MAE) and Mean Squared Error (MSE) of two streak detection algorithms, ASTRiDE and the SD algorithm, across two streak length thresholds: $\geq$10 pixels and $\geq$17.5 pixels.

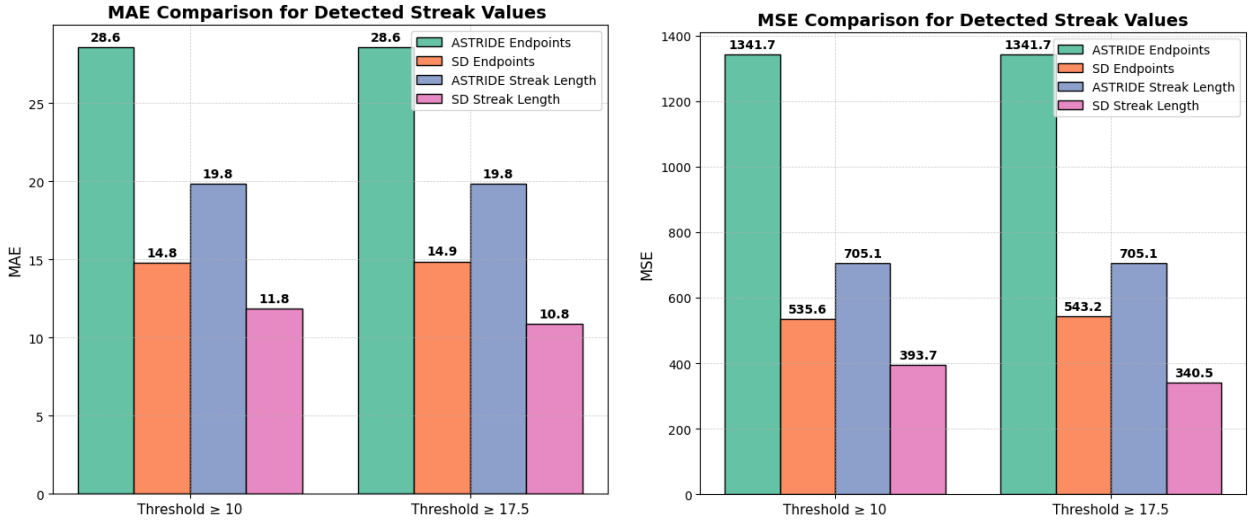

(a) MAE Comparison for Detected Streak Values

(b) MSE Comparison for Detected Streak Values

Figure 28: Comparative analysis of MAE and MSE for ASTRiDE and SD algorithms at different length thresholds.

ASTRiDE's MAE remains consistent across both thresholds, indicating a stable performance that is not influenced by streak length. In contrast, The SD algorithm demonstrates a slight increase in MAE for endpoints at the higher threshold, but its streak length MAE decreases to 10.8 , suggesting

better accuracy in detecting longer streaks. Similarly, ASTRiDE's MSE is unchanged across the thresholds, reflecting consistent performance. In contrastThe SD algorithm, however, shows a slight increase in MSE for endpoints but a decrease in streak length as the threshold increases, indicating improved accuracy in estimating longer streaks.

This analysis reveals significant discrepancies between the two algorithms. ASTRiDE excels in precision, making it suitable for applications where minimizing false positives is critical. However, its lower recall and F1 score suggest that it will miss a significant number of streaks, particularly those with low SNR. Conversely, the SD algorithm shows better overall performance in recall and F1 score, particularly at higher streak length thresholds, making it more effective for detecting fainter streaks, even at the cost of a higher false positive rate at lower thresholds. The choice of algorithm should depend on whether the priority is high precision or maximizing true streak detection. Notably, the SD algorithm consistently demonstrates lower MAE and MSE values, particularly for streak length, which reinforces its superior accuracy in detecting true positive streaks, especially when the statsical distribution of streaks are known.

4.5 Conclusion

In conclusion, this study conducted an in-depth analysis of 6,939 images from the RSONAR flight, resulting in the manual annotation of 544 RSO streaks. By examining streak properties such as length, orientation, SNR, and FWHM, we explored the characteristics of RSOs within the dataset. This analysis is significant because it addresses a critical gap in publicly available SSA datasets, offering ground truth data that can be used to benchmark and validate RSO detection algorithms. The observed diversity in streak properties and the cyclical pattern of streak counts over time underscore the need for detection algorithms that can accommodate the variability and periodic behavior of RSOs, which is essential for reliable RSO tracking.

Moreover, the integration of clustering techniques and image quality metrics provided a deeper understanding of the diversity of RSO streaks within the dataset. This analysis revealed distinct streak patterns and behaviors, which can aid in the classification of different types of RSOs. Such

distinctions are vital for improving trajectory predictions and enhancing overall SSA capabilities. The results of the streak detection algorithm comparison provide key insights into their respective performance. The SD algorithm, with higher recall and F1 scores, demonstrated better overall detection capabilities, especially for faint streaks, making it more suitable for scenarios where maximizing true streak detection is crucial. However, its higher false positive rate suggests that further refinement is necessary to improve precision. In contrast, ASTRiDE's lower but stable precision shows that it can effectively minimize false positives, but its lower recall means it misses many streaks, particularly those with lower SNR. This comparison suggests that the choice of algorithm depends on the specific requirements of an SSA application—whether the goal is high precision or maximizing true detection.

Ultimately, this research shows that streak detection offers a robust means of tracking faint and fast-moving objects that are challenging for conventional object detection methods. By contributing a curated and annotated dataset, as well as offering a comparison of streak detection algorithms, this study lays the groundwork for more accurate and effective SSA systems.

4.5.1 Future Work

Future research will focus on cluster-based classification to understand how specific clusters correspond to particular RSOs types by comparing cluster centers with known RSOs attributes. Outliers within clusters will also be examined to identify unique or anomalous objects. Additionally, the analysis will consider how varying lighting conditions influence streak patterns across different observation windows, aiming to improve predictions of streak characteristics. The SD algorithm will be refined to reduce its false positive rate while maintaining its strengths in recall and F1 score. Furthermore, exploring a hybrid approach that combines the strengths of both ASTRiDE and SD algorithms could lead to a more comprehensive and precise streak detection system.

5 Technology Demonstration of Space Situational Awareness (SSA) Mission on Stratospheric Balloon Platform

This chapter is an excerpt from a 2024 paper [67] describing RSONAR II, which details the development of a next-generation dual-purpose camera system integrated into a 4U-inspired CubeSat platform. The payload was successfully launched in August 2023. The primary objective of this mission was to demonstrate a dual-purpose star tracker capable of imaging and analyzing Resident Space Objects (RSOs) in a space-like environment, contributing to the field of Space Situational Awareness (SSA). Building on the experience from the 2022 campaign, RSONAR II is a real-time, multi-purpose imaging system consisting of two cameras with different cost and performance levels. The Sub-payload 1 can adjust imaging parameters in real-time, enabling the evaluation of various configurations for RSO imaging. Onboard RSO detection and attitude determination were performed to validate the algorithms. Downlink capabilities were implemented to monitor payload performance during the flight. Additionally, the resolution of one of the cameras (Sub-payload 1) was altered throughout the mission to diversify the dataset for algorithm testing.

This chapter focuses on two key areas: firstly, the sub-payload 1 section, and secondly, the comparison of the optics between sub-payload 1 and sub-payload 2. These are the two main areas in which I have made a significant contribution to the RSONAR 2 mission. I generated all figures and tables presented in this chapter. Sections related to electrical design, vacuum testing, mechanical structure, and simulation of RSONAR II are to be referenced in [67]. The development of Sub-payload 2 (STARDUST) by Perushan Kunalakantha and Gabriel Chianelli is excluded from this chapter, with detailed information available in [97]. Perushan Kunalakantha conducted the RSO detection analysis (section 5.6.3) by manually inspecting the Sub-payload 1 dataset and correlating the RSO detection results with images from Sub-payload 2. The theoretical evaluation of the limiting magnitude part of section for Sub-payload 1 and 2 was performed by Randa Qashoa, who also project managed, procured and acquired necessary materials, and aided in the testing and development of the payload and documentation. The aforementioned sections have been rewritten as

well as regenerated figures and tables.Regina S. K. Lee contributed by creating payload metrics, developing mission design documentation, providing feedback during testing and field campaigns, and offering supervision throughout the research project.

I redesigned the GPS-based image acquisition system from the previous flight into an autonomous closed-loop imaging system capable of operating at varying resolutions. I developed the software responsible for generating the health status of Sub-payload 1 and producing image files for downlink. I also performed the comparison between Sub-payload 1 and 2, evaluating the limiting magnitude of stars, field of view, and star detectability, all presented in this chapter. Additionally, I conducted the delay analysis for Sub-payload 1 and developed the thermal profile used for thermal testing to ensure compliance with Canadian Space Agency (CSA) standards. I analyzed thermal measurements recorded by both Sub-payloads. The optical performance of Sub-payload 1 was assessed based on images captured during field campaigns, leading to the development of the operational concept used during the flight. I acquired a substantial dataset from various locations under different lighting conditions, which was used for RSO algorithm development and will be applied in upcoming missions. I also calibrated Sub-payload 1 and collected data necessary for data reduction and distortion correction.

My involvement extended to assembling the payload, mission planning, thermal and vacuum testing, field campaigns, payload operation monitoring during the mission, and post-mission operations along with Randa Qashoa, Perushan Kunalakantha and Gabriel Chianelli . With the rest of the members, I successfully oversaw the launch of the RSONAR payload on a stratospheric balloon from Timmins, Ontario, in August 2023.

Beyond the technical contributions, I co-wrote and directed a series of presentations at the Ontario Science Centre called “SSA and Us,” aimed at educating the public on SSA and its significance. The program included an interactive component where audience members wrote messages that were later engraved onto the payload’s interface plate and custom-made PCB board for the Power Distribution Unit (PDU). Over 2000 messages were gathered during the presentations and were subsequently displayed at Western University’s McIntosh Gallery as part of the exhibit “The Life

Cycle of Celestial Objects Pts. 1 & 2" from September to December 2023, where I assisted in the setup. The exhibit featured the payload alongside a video documenting the development of RSONAR II, which featured images I captured during RSONAR II launch campaign.

5.1 Introduction

Space Situational Awareness (SSA) has been identified in the Canadian research community as a top priority for space activity, as it serves to detect, track, identify, and characterize resident space objects (RSOs). The convention on registration of objects launched into outer space obligates launching nations to supply the United Nations with information regarding the orbit of each space object [98]. However, there are objects in space that have not been identified yet. The uncatalogued elements are primarily composed of space debris resulting from numerous recorded collisions. For instance, the collision between Iridium 33 and Kosmos 2251 in 2009 caused significant telecommunication disruptions and produced thousands of fragments that linger in Earth's orbit [99]. According to NASA, there are over 25,000 objects larger than 10-cm in diameter orbiting today, and an estimated 500,000 objects under 10-cm [100]. To avoid disastrous collisions, it is imperative to enhance technologies and further develop capabilities to identify both foreground (satellites) and background objects (debris).

Ground-based observations of RSOs are constrained by weather conditions, atmospheric interference, limited access time, and visibility to RSOs. In contrast, space-based RSO observations, where imaging is conducted by satellites, enable multi-site simultaneous observations and improved imaging conditions. Hence, recognizing the need for space-based observation, the United States Space Force is already planning a satellite constellation, named "Space-Based Space Surveillance"(SBSS), to assist ground infrastructure [101].

5.1.1 Application Of Wide Field-Of-View (WFOV) Imagers For SSA

Considering the latest technologies available for space optical sensors, we have focused our efforts on the use of space-based, WFOV cameras including star trackers and similar low-resolution

imagers, for SSA applications. These commercial-grade cameras, such as the AURICAM™ star tracker by Sodern [102], and PCO scientific Complementary Metal–Oxide–Semiconductor (sCMOS) camera [52] are far less costly than dedicated imaging systems with custom telescopes. They are also readily available onboard satellites to provide attitude information. Additionally, WFOV cameras are capable of continuously monitoring large parts of the sky. These cameras can monitor multiple objects without actively tracking them which allows for quick detection capabilities used in rapid capture, detection, timely identification and tracking. Early warning of close approaches can also be implemented using full-sky coverage to respond to potential collisions and plan collision avoidance maneuvers if necessary. While the images obtained with WFOV cameras tend to have reduced resolution that lacks features for identification, simple detection in photometric analysis—with light curve extraction—provides sufficient information for astrometric analysis and object classification. [103], light curve extraction has been performed on images captured from WFOV cameras and in [41], object classification has been proven with light curves collected from ground-based telescopes.

5.1.2 Resident Space Object Near-space Astrometric Research II (RSONAR II)

The long-term objective is to develop low-cost wide-field-of-view (WFOV) optical systems for the detection of resident space objects (RSOs) suitable for nanosatellites. In order to achieve this objective, a dual-purpose camera system has been developed which is designed to function both as an attitude sensor and as an SSA payload [54]. The concept was initially demonstrated during the STRATO-SCIENCE 2022 mission, which was supported by the Canadian Space Agency (CSA) through the FAST Project # 19FAYORA12 [104]. Based on the findings of the aforementioned mission, we have refined image-processing algorithms [32, 18] and developed FPGA-based camera electronics. Furthermore, we have collaborated with Defence Research and Development Canada (DRDC), Magellan Aerospace, C-Core, and the University of Manitoba to explore potential future Canadian SSA mission concepts.

The second-generation mission, Resident Space Object Near-space Astrometric Research II (RSONAR

II), was designed to enhance the SSA dataset and demonstrate improved software capabilities during the 2023 flight. The stratospheric balloon platform provides a faster and more cost-effective alternative to space-based missions [104]. The project spanned 10 months, from the initial concept design to the actual flight. During this period, a substantial RSO image dataset was acquired through ground observations. The dataset was utilized for hardware testing, algorithm design, and the enhancement of our SSA algorithms in advance of a CubeSat launch to Low Earth Orbit (LEO). The mission included two imaging systems, which were designated as Sub-payload 1 and Sub-payload 2. Sub-payload 1 introduced in-flight resolution adjustments and downlink communication for real-time health monitoring and data acquisition. Moreover, discrepancies identified in the initial data set were rectified, resulting in a more reliable and comprehensive data collection. While Sub-payload 2 investigated real-time attitude determination (AD) and RSO detection with cost-effective alternative hardware concepts. This chapter primarily discusses Sub Payload 1 and its image acquisition process, while also providing preliminary analysis of the optical performance of both imaging systems. A more comprehensive examination of the data will be presented in a subsequent publication.

5.2 Hardware

5.2.1 Optics

The optical system comprised a scientific sCMOS sensor, the pco.panda 4.2 from PCO Imaging, based in Kelheim, Germany [52]. The ZEISS Dimension 2/25 lens from Carl Zeiss Industrielle Messtechnik GmbH, located in Oberkochen [53] was the lens of choice for subpayload 1. In comparison to the PCO imager onboard RSONAR II, two other imagers AURICAM™ and the Fast Auroral Imager (FAI) are also listed. AURICAM™ is a commercial star tracker [102], manufactured by Sodern. Various models of star trackers from different vendors have been flown on various satellites including DirecTV-15, One Web, Pléiades Neo, and Cygnus missions among others. The FAI is part of the e-POP Mission onboard the Cascade, Smallsat and Ionospheric Polar Explorer

(CASSIOPE) satellite, whose primary focus is on ionospheric and space weather studies. The FAI [39] features a WFOV of 26° and images aurora around the Earth in nadir pointing orientation under nominal conditions. FAI has an f/4 lens system that is combined with a fibre-optic taper which results in an effective f-number of f/0.8. While FAI is not a star tracker typically used for attitude determination like AURICAM™, we have used FAI images to examine spaceborne RSO images for feasibility [28], simulation analysis [105] and RSO observation prediction analysis. A feasibility study was conducted on the use of the IDS UI-3370CP-M-GL Rev.2 compact monochrome camera, coupled with a telephoto lens [106, 107], for Sub-payload 2. This low-cost optical system was found to be an economical alternative, costing approximately one-tenth of the PCO imaging system while offering comparable sensor specifications in a compact form factor. The key specifications of these four imaging systems are detailed in Table 15 are relatively similar. The FOV is directly proportional to the number of pixels in the sensor and the pixel size; conversely, it is inversely proportional to the focal length.

Table 15: Key specifications of four imagers (AURICAM™, PCO, FAI and IDS) are compared to illustrate the similarities in FOV and pixel size.

Characteristic	AURICAM™	PCO	FAI	IDS
Number Of Pixels	2048^2	2048^2	256^2	2048^2
Pixel size (μm)	5.5	6.5	26	5.5
Field-of-View (degrees)	35	29.6	26	41
Focal Length (mm)	25	25	6.89	16

5.2.2 Electronics

The Xilinx PYNQ-Z1 System on Chip (SoC) development board, acquired from Digilent, in Pullman, WA, [108] was chosen as the OBC for subpayload 1. The board is built around the Xilinx Zynq®-7000 SoC, which incorporates an FPGA and a dual-core ARM Cortex™-A9 processor. The communication subsystem for telemetry via the Ethernet IP network protocol is accomplished by implementing the FPGA fabric using Python. The development of the image acquisition application and the management of its drivers were handled by the processor, which operates on a

Linux-based system. The board is powered by the 12 V output line connected to its onboard power jack from the PDU. The OBC utilizes a USB-A to USB-C cable to connect to the optical system, powering the camera and facilitating the exchange of image data. Debugging was performed using the Secure Shell (SSH) and USB serial protocols.

To host the operating system and store images, hardware drivers, and sensor data, we reused an Innodisk industrial-grade 512 GB microSD card, which was sourced from Innodisk Corporation in New Taipei City 221, Taiwan [109]. Since it stores crucial data, the microSD is a vital component of the system. However, the microSD card is categorized under the Ultra-High Speed (UHS) class 1, featuring a minimum speed of 10 MB/s [110]. The team did not find any other microSD card capable of matching or exceeding this level of performance under similar operating temperatures of stratospheric flight. Additionally, the card's ability to withstand thermal requirements and its performance during the previous year's flight validated the decision to reuse it for the current mission. It should be noted that the other, sub-payload 2 of RSONAR II were tested with microSD cards with inferior ratings to prove the viability of using cheaper non-weather-rated microSD cards for future missions. Figure 29 outlines the connections between the components of the subpayload 1.

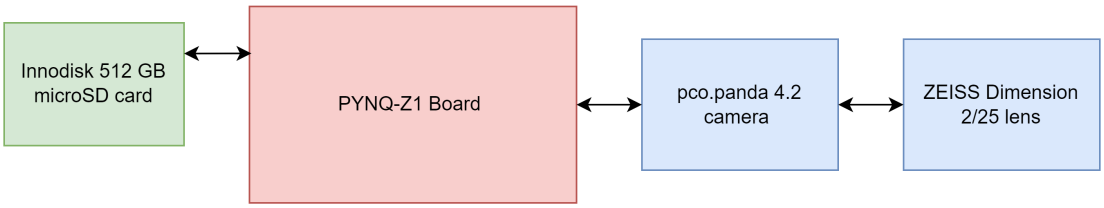

Figure 29: Diagram illustrating the connections among the electronics within the subpayload 1

5.3 Payload Development

5.3.1 Thermal Testing

Similar to RSONAR, RSONAR II used passive thermal control by covering the payload with aluminum polyamide. Based on measured temperatures recorded during previous flights, it was deter-

mined that internal payload components were likely to experience temperatures of approximately -20°C. As a result, a temperature profile was created for RSONAR II, with a minimum temperature of -20°C. The payload underwent a 16-hour operational assessment in a thermal chamber to evaluate any alterations in its performance. Following the thermal test, it was ascertained that all components were functioning properly with no performance degradation in the systems.

5.3.2 Long-Form Communication Testing

To test the payload's downlink capability over the duration of the mission and ensure robustness to connectivity issues, a 12-hour long-form functional test was conducted. Simultaneously, the payload acquired images. Subsequently, the image acquisition delays were subjected to analysis to determine the optimal manual delay values that could be implemented between images to mitigate any unanticipated system delays.

5.3.3 Field Campaigns

Multiple field campaigns were conducted to acquire starfield images with the optical systems. On some occasions, short component-level tests focusing on a particular imaging system took place, while on others, full end-to-end tests, including downlink capability, were carried out. These campaigns aimed to calibrate the optical system based on the brightest stars in view. Innisfil, Ontario, was the site of one of the system-level tests. The sky brightness in Innisfil was measured at 20.18 mag./arc sec², ranking it as 5 on the Bortle Dark Sky Scale [111], in contrast to a sky brightness of 17.80 mag./arc sec² that is in typical urban cities, ranking 9 on the same scale. Figure 30 illustrates a series of images captured by Sub-payload 1 during the Innisfil field campaign, featuring an RSO sequence. These images have been enhanced using the Zscale algorithm, which highlights images near the median [112]. Additionally, multiple system-level tests were conducted in Timmins, Ontario, with a sky brightness ranked as class 4 on the Bortle Dark Sky Scale prior to the launch window. These campaigns were essential in acquiring datasets from various locations, in addition to those from the proposed flight.

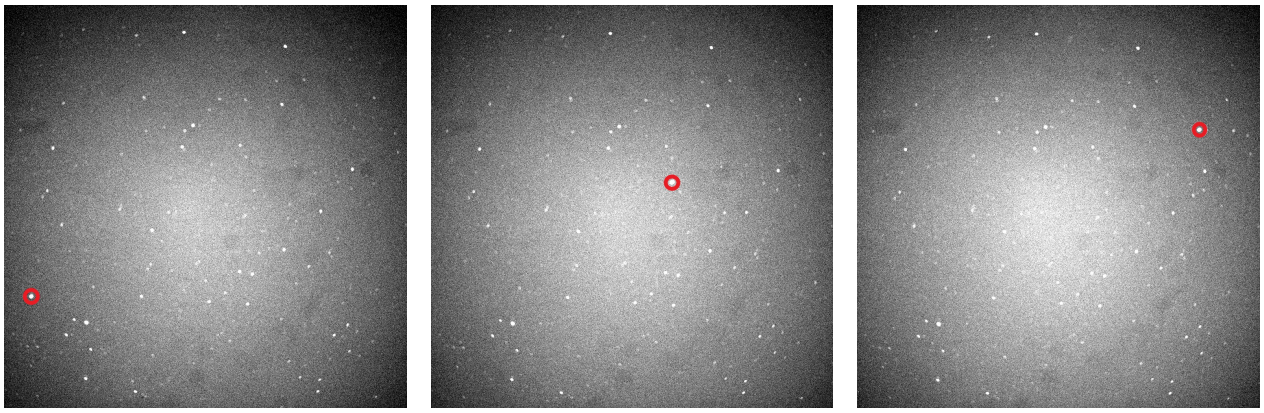

Figure 30: Example of a sequence of PCO camera images captured from a field campaign. The red circle shows the location of the RSO as it transits. These images have been enhanced with the use of the Zscale algorithm.

5.4 Software

5.4.1 Image Acquisition

The image acquisition application was developed in C++ using the header files and functions provided by the PCO camera. In the event of a power outage, the system was designed to reboot, to prevent any open drivers from causing interference with image acquisition. In the initial stages of the mission design, the GPS-based image acquisition system from the previous flight was modified to be an autonomous closed-loop imaging system only accounting for the PCO camera and the OBC. Therefore, the application was redesigned to enable continuous imaging at resolutions of 512×512 pixels, 1024×1024 pixels and 2048×2048 pixels upon startup. After boot-up, the system initialized into the low-resolution mode (low-res) with a resolution of 512×512 pixels to capture four images for downlink, each with an exposure time of 500 milliseconds. The next step involved imaging in medium resolution mode (med-res) at a resolution of 1024×1024 pixels with an exposure time of 100 milliseconds capturing 5100 images. Then the application was programmed to capture at a high resolution (high-res) of 2048×2048 pixels with an exposure time of 100 milliseconds acquiring 600 images. Afterwards, the application transitioned to low-resolution mode, then medium-resolution and back to high-resolution, operating as a closed-loop system until it was powered off.

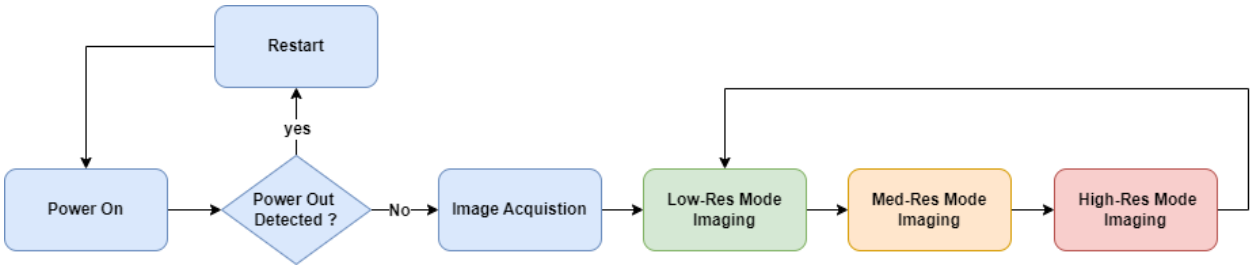

Figure 31: Block diagram outlining the closed-loop image acquisition application once the payload is powered on.

A system delay of 200 milliseconds was added between each image when imaging at med-res and high-res modes to account for the microSD write speed of 10 MB/s. The system health status comprises the exposure rate, resolution, and system delay at the current mode of acquisition, along with three temperature recordings of the PCO camera at various locations (sCMOS sensor, camera, and power supply). Low-resolution mode images are then downlinked to the ground station along with the sensor's health status. These modes are designed to enable continuous data acquisition for the planned flight duration of 12 hours, with an added 2-hour margin requiring the payload to be powered on prior to launch. Refer to Figure 31 for an overview of the image acquisition process from bootup.

5.4.2 Communications

In the first iteration of the mission, the payload's performance during the mission was assessed solely through current consumption during flight. Consequently, one of the significant upgrades to RSONAR II involved the inclusion of downlink functionality for Sub-payload 1. This new capability allowed for continuous real-time monitoring of subpayload 1's status throughout the mission. In order to adhere to the allocated rate of 350 kilobits per second, we downlinked four 512 x 512 pixel images captured from the PCO camera at 500-millisecond exposure intervals along with a CSV file that included subpayload 1's overall system health status. The CSV file comprised onboard time, mode of acquisition, imaging parameters, latest image count, and the PCO camera temperature. Due to the relatively high exposure rate used for these images, any RSO present in the downlinked images would appear as a streak, providing visual confirmation of RSO imaging

during flight. To ensure the allocated capacity was never exceeded, images were transferred in small, manageable packets, with multiple validations of downlink performance conducted prior to launch. Radio Frequency communications were handled from the CSA balloon. An Ethernet cable was used to connect the PYNQ Z1 board on Sub-payload 1 to the CSA's communications module.

5.5 Results

5.5.1 Flight Summary

RSONAR II was launched at 4:52 AM UTC on August 22, 2023, from Victor M. Power Airport located in Timmins, Ontario. The flight was shortened to approximately 5 hours due to adverse weather conditions, significantly shorter than the expected 9 to 12 hours. After the mission ended, the payload was recovered from Chapleau, Ontario.

5.5.2 Image Acquisition

A total of 65,951 images were captured and stored over 6.5 hours, resulting in 170 gigabytes of data. These images comprised of 6,600 at a resolution of 2048×2048 pixels, 60 at a resolution of 512×512 pixels, and 59,291 at a resolution of 1024×1024 pixels. The hourly image capture rate remained consistent with the previous year, but there were significant delays expected and observed during the imaging period (refer to section 5.5.4 for further delay analysis).

5.5.3 Data Telemetry

The payload effectively transmitted images and telemetry health files throughout the entire mission duration. A total of 160 files were downlinked over the course of the mission. Figure 32 shows a sample image that was downlinked.

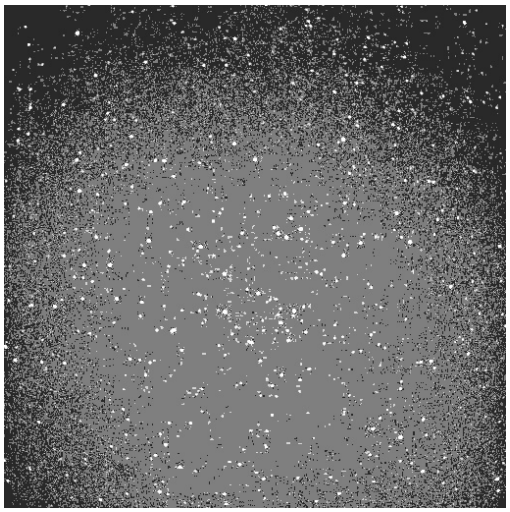

Figure 32: Sample Downlinked Image enhanced with Zscale algorithm.

5.5.4 Delay Analysis

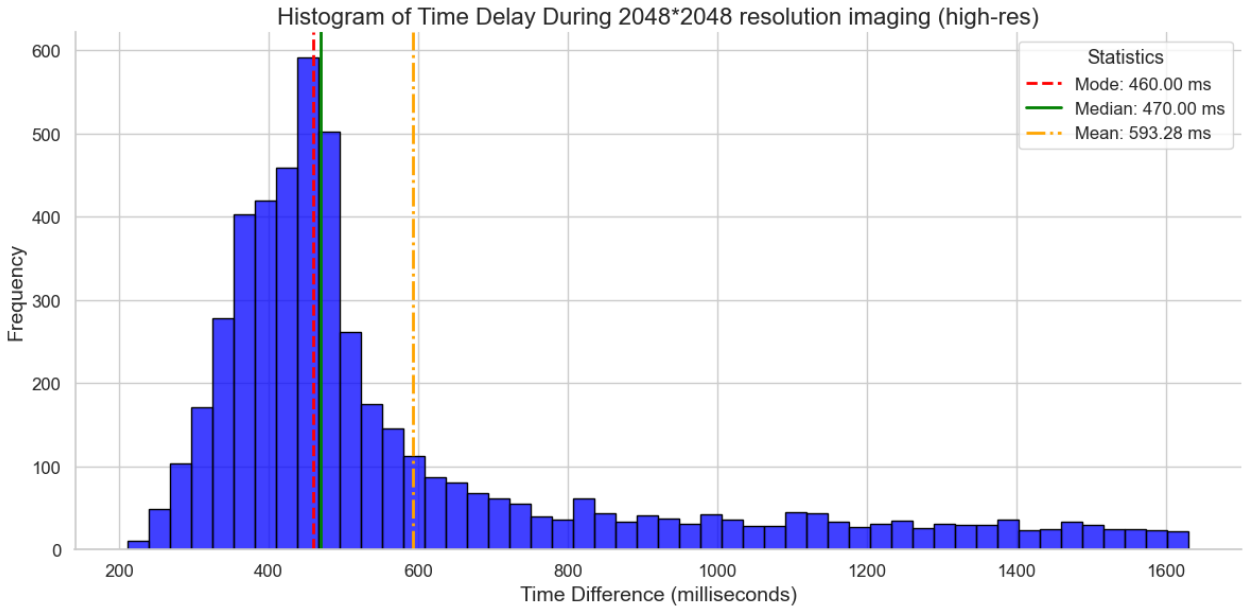

Figure 33: The distribution of time delays between images during high-resolution 2048x2048 imaging, with the frequency of occurrences on the y-axis and the time difference in milliseconds on the x-axis. The mode (460 ms), median (470 ms), and mean (593.28 ms) are indicated by the red dashed, green solid, and orange dash-dotted lines, respectively.

Due to the slow microSD card speed, a 200 ms delay was implemented after each image capture to prevent system delays. Time intervals between captures were measured using the board time in the image name, accounting for exposure and self-induced delays, with the name generated

before imaging begins. Significant delays during mode transitions were observed, likely caused by changes in imaging parameters. To address this, outliers in the delay dataset were removed using the Interquartile Range method (IQR), defining outliers as delay values outside $Q1 - 1.5 \times IQR$ or $Q3 + 1.5 \times IQR$. Figure 33 shows the distribution of delays for high-resolution 2048x2048 imaging. Except for a few anomalies, negligible or no delay was observed in both the low and medium-resolution modes.

5.5.5 Thermal Analysis

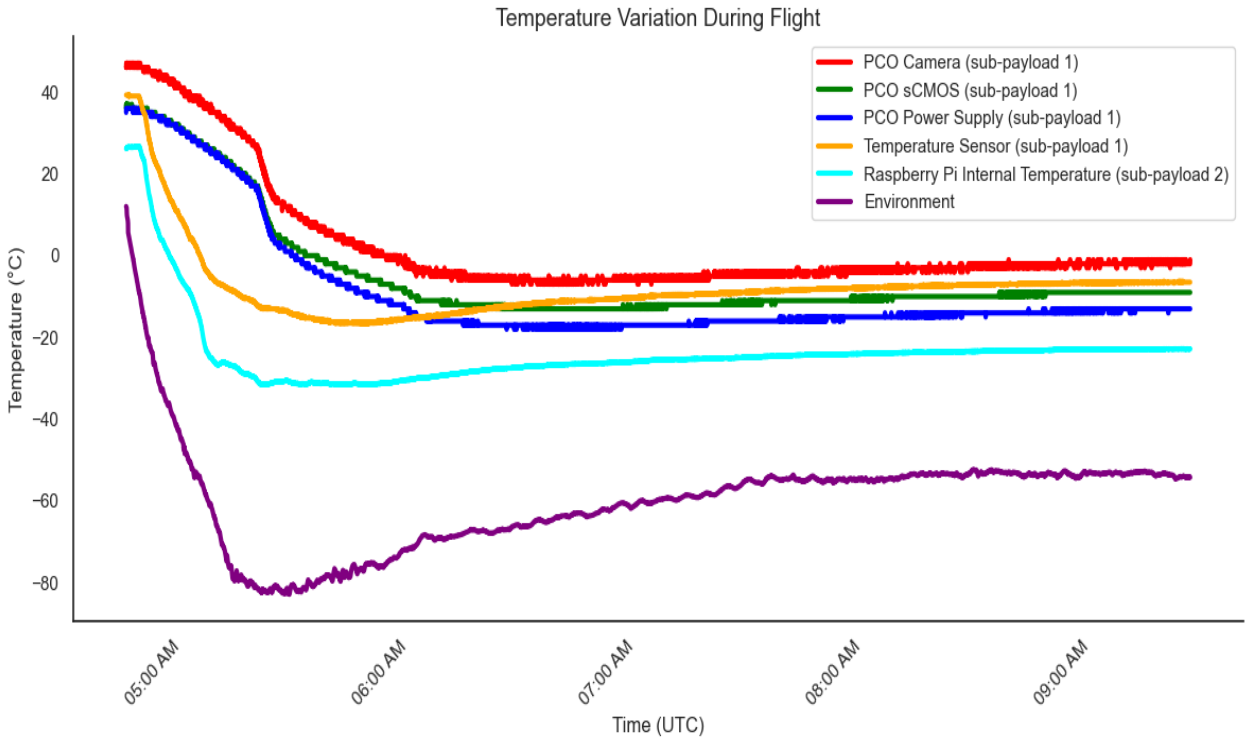

Figure 34: The graph illustrates temperature fluctuations of various components during the mission flight on August 22, 2023, from 4:52 am to 9:34 am (UTC). Notably, both the payload and the environment experienced significant temperature changes in the initial two hours. Subsequently, the temperature of all components stabilized as the flight coasted at the targeted altitudes, with only minor temperature fluctuations observed.

In subpayload 1, PCO gathered temperature data for the sCMOS, power supply, and camera during every image capture. A temperature sensor was fixed to the PCO body, and the readings were registered by subpayload 2's Raspberry Pi in addition to its own internal temperature. The operational

temperature of the payload components was a fundamental aspect of the payload design due to the expected ambient temperature of -80°C. Figure 34 displays temperature readings for different components of the payload and the external environment during the payload's operational phase of the flight. This work is based on observations with the CNES temperature sensor under a balloon operated by CNES, within STRATO-SCIENCE 2023 and in the framework of the CNES/CSA Agreement.

5.5.6 Sensor Comparison

Limiting Magnitude Cameras with different capabilities and price ranges were employed for RSO and star observations during this mission. Before the mission, the limiting magnitude for each sensor was estimated, representing the faintest star detectable by each system. The sensor's limiting magnitude is calculated by determining the magnitude of an object at which the Signal-to-Noise Ratio (SNR) is at the minimum level necessary for detectability. The limiting magnitude for an RSO can be calculated using the following equation:

$$m_{lim} = -2.5 \cdot \lg\left(\frac{25hc}{1.78 \times 10^{-8} Q_e A \lambda t}\right) \tag{14}$$

Where Q_e represents the sensor's quantum efficiency, λ is the wavelength, h is Planck's constant, c is the speed of light, A is the aperture area, and t is the integration time.

Based on the analysis of RSOs from the RSONAR mission in Table 8, a minimum SNR of 5 was found to be sufficient for detection. The equation presented in 14 does not account for sensor noise, reinforcing the choice of this SNR threshold based on previous flight data. Furthermore, since detailed information on many commercial star trackers is not publicly available, this equation serves as a reliable approximation. Given that the acquisition mode was SSM, the motion of the RSO was not included in our analysis. This estimation provided an initial assessment of the sensor's performance.

Figure 35 displays a plot of limiting magnitudes for a range of integration times determined using Equation 14. The vertical line indicates an integration time of 100 milliseconds, which was the

value used during the mission.

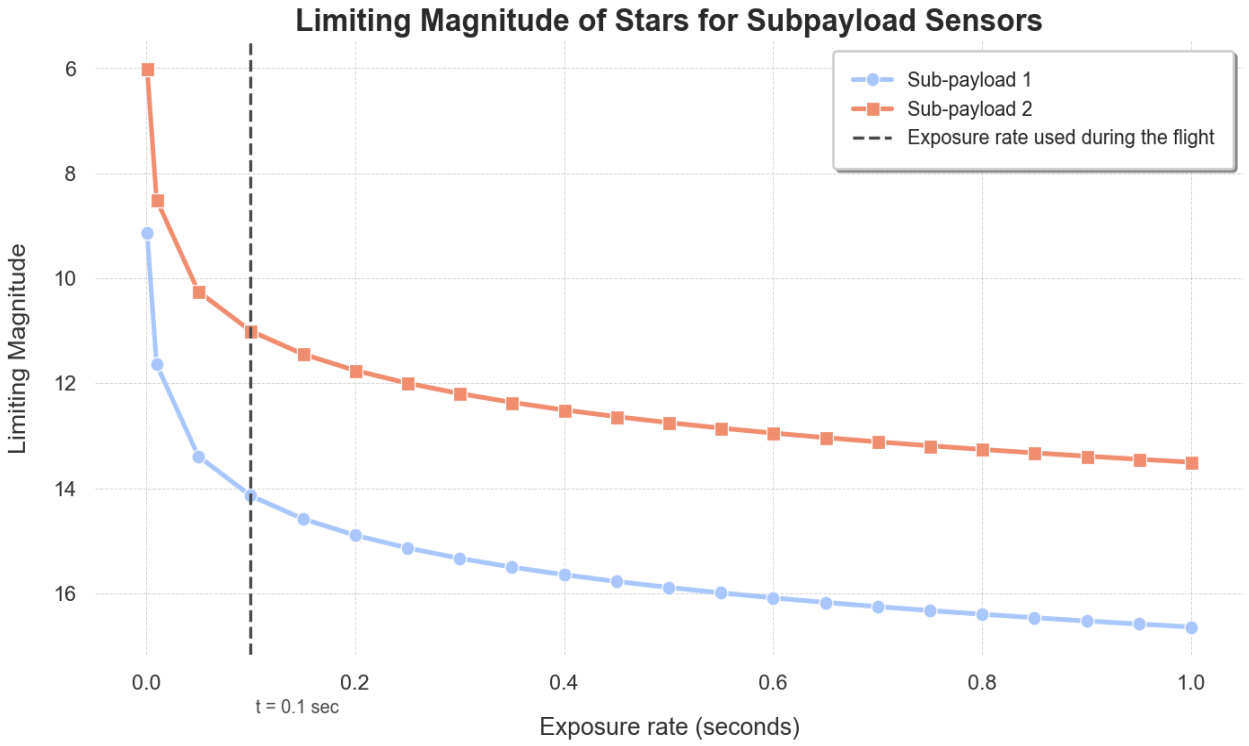

Figure 35: Plot of limiting magnitude over integration time for RSONAR II sensors.

Validation of Limiting Magnitude The images obtained at the end of the mission from subpayloads 1 and 2 were processed with Astrometry.net [43] to compute the World Coordinate System (WCS) and the field distortions present in them. The celestial sources within the images were detected using DAOStarFinder function from the photutils package in Astropy [113]. A Full Width at Half Maximum (FWHM) value of 3 and the threshold was set at 2.5 times the standard deviation of pixel intensities in the images for the source detection. After extracting the sources, their pixel coordinates were converted to Right Ascension (RA) and Declination (Dec) values using WCS. The sources detected were queried using the Hipparcos catalogue [114] from the VizieR database [115], with a search radius equivalent to the pixel scale of the respective images. Figure 36 depicts the frequency of detected star magnitudes in the Johnson V band from the subpayloads.

Field of View (FOV) Figure 37 shows segments of the Pisces constellation as captured by subpayloads 1 and 2 near the end of their operational phase in flight. The 2048×2048 resolution images

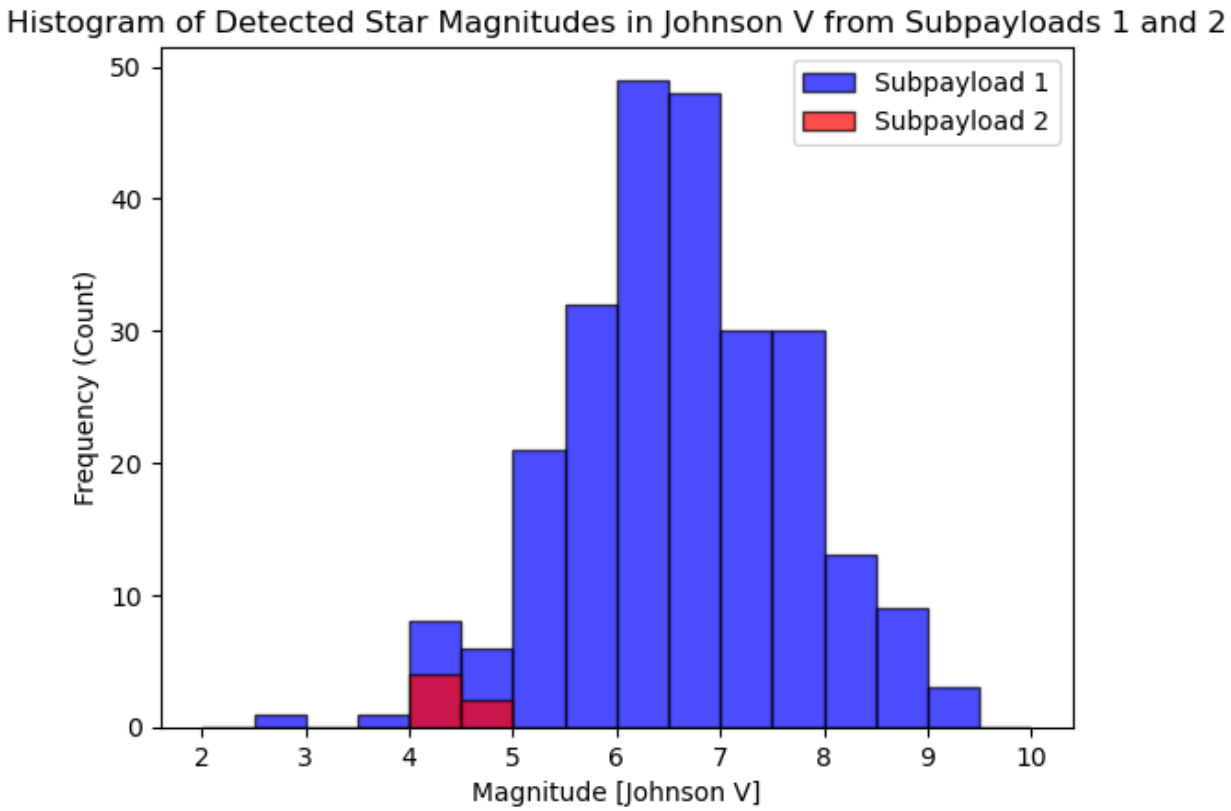

Figure 36: The histogram displays the frequency of stars detected at different magnitudes (brightness levels) in the Johnson V (visual) band, with two datasets represented: Subpayload 1 in blue and Subpayload 2 in red. The x-axis represents the Magnitude [Johnson V], a logarithmic scale used to measure the brightness of stars, while the y-axis indicates the frequency of stars at the detection's magnitude ranges.

were processed for celestial coordinates using astrometry.net [43] and labeled using the Tycho-2 catalog. Due to the optical sensors' similar FOV and placement within the payload, there was an expected overlap in starfield observations within regions of starfield imaging. Furthermore, Table 16 presents the calibration metrics alongside the right ascension and declination values from images presented in Figure 37.

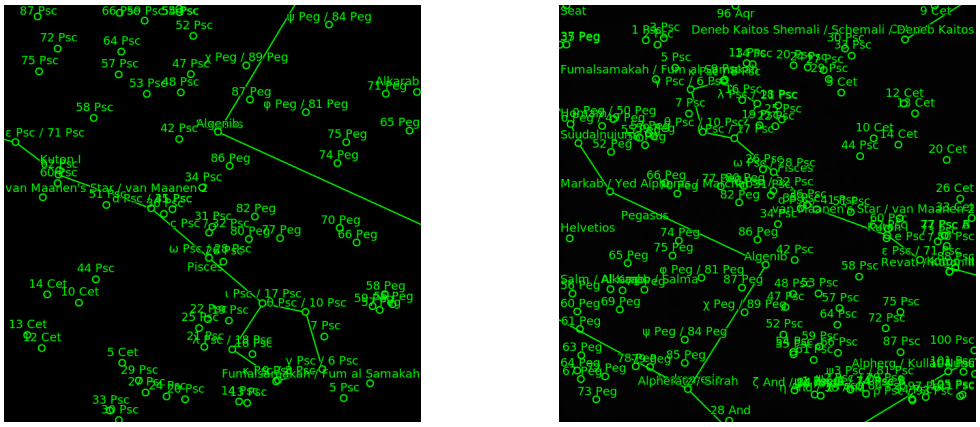

(a) (b)

Figure 37: (a) Subpayload 1; (b) Subpayload 2; displays parts of Pisces constellation captured by subpayloads 1 and 2 towards the end of their operational period during flight.

Table 16: A detailed comparison of two cameras, PCO and IDS, based on various characteristics relevant to stellar observations from 2048×2048 images.

Characteristic	PCO	IDS
Pixel Scale (arcsec/pixel)	52.3	72.1
Central Right Ascension (degrees)	1.012	1.170
Central Declination (degrees)	9.816	10.757
Orientation (East of North in degrees)	-153.6	153.4
Radius (degrees)	21.056	29.004

Star Detectability To assess the camera sensors' capacity to distinguish stars from the background sky, contrast maps are used in starfield imaging. A sliding window approach was employed to perform local contrast measurement within these images. This method calculates contrast over small, localized areas of the image and then moves this window across the entire image. Figure 38 displays the contrast maps of images from subpayload 1 and subpayload 2.

In starfield imaging, a histogram can visualize intensity distribution, with a characteristic peak at the lower intensities and some spikes at the high intensity end, as shown in Figure 39 using the minimum and maximum pixel values within the images.

RSO Detection

The RSO detection capability of Sub-payload 1 was achieved by manually identifying the RSOs in the captured images and distinguishing them from the background stars. However, the RSO

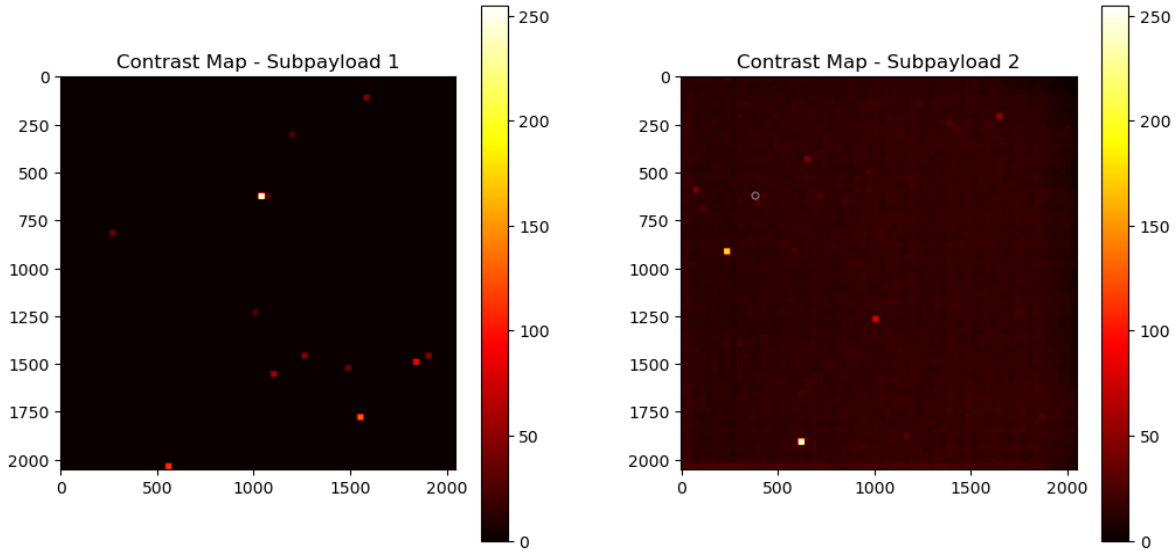

(a) (b)

Figure 38: Contrast maps for (a) Subpayload 1; (b) Subpayload 2 capturing the same starfield, which reveals the variations in local contrast across each sensor's image. Brighter squares indicate areas of higher contrast, likely corresponding to celestial bodies, against the darker background of space.

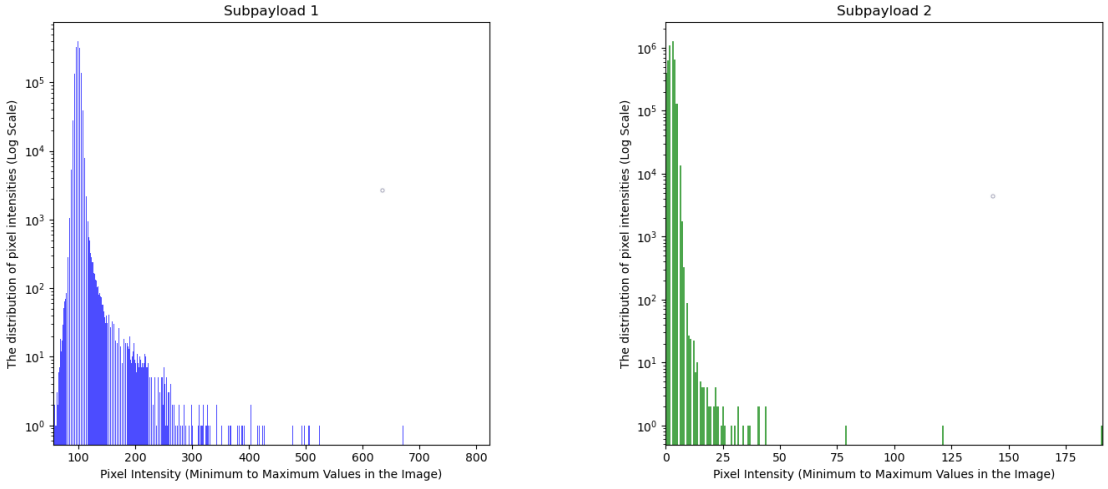

(a) (b)

Figure 39: Two histograms are presented, each in log scale, representing the distribution of pixel intensities from the minimum to maximum pixel values in the images: (a) a 16-bit image from Subpayload 1, and (b) an 8-bit image from Subpayload 2, respectively.

detection capability of the Sub-payload 2 was evaluated by comparing the detections made by the onboard algorithm with the images to validate the algorithm's findings [97]. Due to the brief flight profile, only the 92 minutes of data collected post-ascent were subjected to analysis. Furthermore, images captured by Sub-payload 1 for downlink were excluded from this analysis due to their lim-

ited quantity and discrepancies from the remainder of the dataset. Table 17 presents a comparison of the imagers across various metrics.

Table 17: Comparison between the Sub-payload imagers 1 and 2 on a variety of metrics.

Characteristic	Sub-payload 1	Sub-payload 2
Exposure Time (ms)	100	100
Resolution (pixels x pixels)	2048 x 2048, 1024 x 1024	2048 x 2048
Total Images	13477	21817
Total RSO Detections	30855	669
Unique RSOs Detected	245	11

5.6 Discussion

5.6.1 Delay Analysis

From Figure 33, the histogram displays an unimodal distribution with a prominent peak. The data are skewed towards the right, as evidenced by the tail extending towards longer time delays. The mode value of 460 ms is in proximity to the median value of 470 ms, suggesting that the most common time delay is close to the middle of the distribution. The mean value of 593.28 ms is higher than both the median and mode. This disparity is possibly due to a natural asymmetry in the delays, rather than extreme values. The continued presence of higher delays after the exclusion of outliers indicates issues with the imaging system that must be addressed to decrease the frequency of such high delays, which can be directly linked to the SD speed rate.

5.6.2 Thermal Analysis

The payload was powered on two hours before the balloon's launch, leading to an initial temperature higher than the surrounding environment which can be seen in Figure 34. The most significant temperature changes occurred between 5:00 AM and 6:00 AM UTC, possibly during the balloon's passage through different atmospheric layers, followed by stabilization post-ascent. The external high-altitude temperatures were substantially colder than the payload components. The Raspberry

Pi's internal temperature remained stable, indicating effective thermal regulation. Temperature readings recorded lows of -13°C, -18°C, -16.7°C, and -7°C for the PCO components, -82.78°C for the environment, and -31.6°C for the Raspberry Pi. The subpayloads' components were both warmer than their environment, most likely due to the passive heating and thermal blanket insulation. The PCO camera generated more heat compared to the Raspberry Pi in subpayload 2. The internal temperature of the Raspberry Pi is noticeably lower than what would be expected during standard operating conditions. Therefore, it appears feasible to consider overclocking the Raspberry Pi in these circumstances, as it could potentially produce added heat and enhance its performance. However, overclocking could still lead to system instability if implemented improperly. As such, overclocking should be approached cautiously, with thorough testing prior to deployment in future missions. The standard microSD card, rated at UHD speed class 3 and utilized in the Raspberry Pi of subpayload 2, which was not designed for stratospheric temperature ranges, functioned below its expected temperatures, indicating the potential for using faster microSD cards within these temperature ranges in future missions.

5.6.3 Sensor Comparison

Based on Figure 35, it can be estimated that the PCO camera has a limiting magnitude of approximately 14 at 100 milliseconds, while the IDS camera has a limiting magnitude of around 10 at the same exposure time. As a result, numerous stars and, by extension, RSOs should be detectable using both sensors. Despite the fact that the PCO camera is ten times more expensive than the IDS camera, both systems are capable of capturing enough stars and RSOs to support the attitude determination and RSO detection algorithms. This estimation was validated during the mission as both systems were able to capture stars and RSOs.

Figure 36 demonstrates that Subpayload 1 detects stars at a frequency ten times higher than Subpayload 2. The plot employs the Johnson V magnitude system, also known as visual magnitude, operating at an effective wavelength midpoint of 551 nm, a part of the UBV photometric system used for classifying stars. The histogram reveals that most stars detected by Subpayload 1 (repre-

sented in blue) have magnitudes ranging approximately from 5.5 to 7.5, with the peak frequency observed between magnitudes 6 and 7. In contrast, Subpayload 2 (depicted in red) shows fewer detections and a more limited magnitude range. Subpayload 1 demonstrates a higher sensitivity in star detection with a quantum efficiency of 90% and a spectral responsivity range of 350-800 nm. In contrast, Subpayload 2 exhibits a peak quantum efficiency of 64% within a wavelength range of 400-800 nm. The magnitudes of sources extracted from images were found to be significantly lower than those evaluated from Equation 6. This discrepancy can be attributed to the parameters used in source extraction and the correlation of celestial objects within the catalogue. However, the most significant factor reducing the detection of dimmer magnitudes is the noise present in the sensors. Furthermore, the images used for extraction were captured at the end of the mission, a time when the sun was 9 degrees below the horizon, further contributing to this reduction.

Figure 38 clearly illustrates Subpayload 1's sensor's ability to capture stars as bright, well-defined points against the dark sky, demonstrating high contrast. In comparison, Subpayload 2's sensor produces a contrast map with a more homogeneous appearance, with stars appearing less distinct against the background. This comparison is essential as it uncovers the relative constraints of Subpayload 2's sensor, potentially caused by increased noise levels, decreased dynamic range, or differences in ISO and overall imaging system quality. The contrast map for Subpayload 1, with its distinct and high contrast dots, is not only a confirmation that the sensor can detect stars but also a testament to its enhanced capabilities for photometric and astrometric analysis. High contrast is crucial for precise photometry, which depends on accurate measurements of object intensities, and for detecting faint Resident Space Objects (RSOs), which require clear distinction from background noise. The contrast map of Subpayload 1 provides evidence of functional sensors and indicates an imaging system that has the potential to significantly improve the quality and reliability of astronomical data.

In Figure 39, the pixel intensity distributions from the images captured by the subpayloads yields distinct insights. Subpayload 1 exhibits a higher dynamic range, as evidenced by the broader spread of pixel intensities, ranging from the minimum to the maximum values within the images. This

wide range is indicative of Subpayload 1's capacity to capture a full spectrum of brightness, from deep blacks to bright highlights. In addition, Subpayload 1 demonstrates a greater variation in the brightness of features within the images. This is characterized by distinct peaks at multiple intensity levels in the histogram. Such variation is indicative of the payload's ability to resolve differences in brightness with high fidelity. The pronounced peaks at the lower end of the intensity spectrum are characteristic of the dark background typical in starfield images. Moreover, the increased count of lower intensity values in Subpayload 1's histogram compared to that of Subpayload 2 conclusively shows Subpayload 1's superior sensitivity to subtle light features. Subpayload 1 is equipped with a more refined detection capability for capturing faint astronomical phenomena, as expected.

In terms of RSO detection, the PCO camera appeared to be far superior to the IDS camera. As per the results in Table 17, the PCO camera was able to capture over 20 times as many unique RSOs, while yielding more than 40 times as many RSO detections. This was despite the fact that the PCO camera had a narrower FOV and almost half as many images. However, this is expected, given that the PCO camera was selected for its low-light sensitivity and low-noise, and is an order of magnitude costlier than the IDS camera. It is important to note, however, that the RSOs detected by the IDS camera were determined by the onboard algorithm, rather than a comprehensive visual review of the original images, which is to be done. Therefore, it can be expected that the IDS camera may have captured more RSOs but was limited by the algorithm's performance.

5.6.4 Outreach

In addition to the primary objectives stated earlier, the secondary objective of the mission is to provide a platform for public outreach on SSA. Given that this is not a technical goal, it was not included in the main payload discussion earlier. In March 2023, we performed a series of presentations to children and their parents at the Ontario Science Centre. The program, called "SSA and Us", was intended to inform the general public about SSA and its importance. An interactive aspect of this endeavour involved asking the audience to write a message that will be sent on our payload to near-space. The payload's interface plate and custom-made PCB board for

the PDU were engraved with over 2000 messages gathered during the presentation. Following the mission, the messages are on display at Western University's McIntosh Gallery as part of "The Life Cycle of Celestial Objects Pts. 1 & 2" exhibit between September and December of 2023, where visitors can view these messages. Additionally, the exhibit features the payload staged with a video showcasing the development journey of RSONAR II shown in Figure 40 [116]

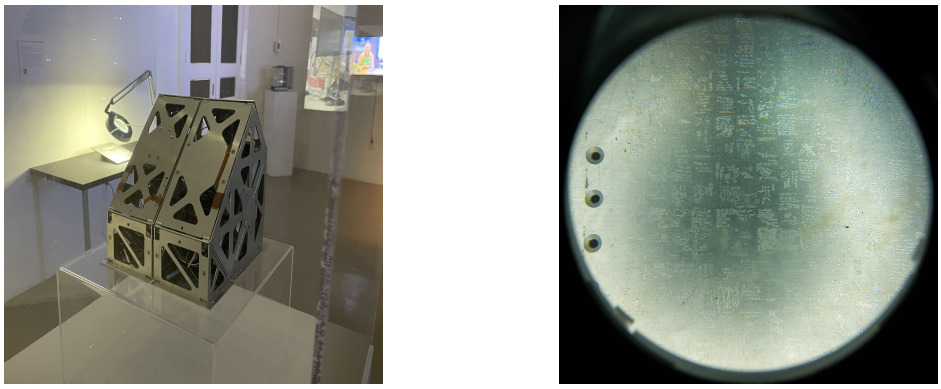

(a) (b)

Figure 40: The Life Cycle of Celestial Objects Pts. 1 & 2; (a) RSONAR II payload display, (b) Some of the etched messages seen through magnifying glass.

The initiative to develop and deliver a series of activities around SSA is in recognition of the need for public outreach for space programs. In this unprecedented time of access and democratization of tools, there is an urgent need for a reframing of space. It should not be viewed as a 'new frontier' for appropriation and extraction but as a critical site for considering how we, as a whole, can participate in pioneering explorations in the skies above us. Space-art has been recognized as a tool for public outreach for many years in its myriad representations of data, creative fiction and myth-making. These networks offer significant potential today, especially with the growing need for amateur space observations. Such efforts support the recording and identification of an increasing number of space objects, including satellites and debris.

Therefore, the objectives of the SSA outreach project are to (1) develop hybrid and synergistic strategies across space engineering, community practice, and visual arts to catalyze a collective imagination and envisioning of future worlds and (2) create access and accountability in the use of high-level data for public workshops around SSA data visualization and physical/virtual modes

of creative data visualization. Throughout the RSONAR II mission, we have collected qualitative and quantitative data around SSA, space exploration, and the commercialization of space through interviews with workshop participants, field specialists, and social media analyses. We adopted research-creation strategies around data visualization and public exhibition formats, constantly evaluating our methods for effective communication.

5.7 Conclusions

This chapter presented the second iteration of a dual-purpose star tracker system deployed on a stratospheric balloon. A key achievement was the successful demonstration of real-time image downlink, which allowed us to monitor the payload's performance throughout the mission. This capability is essential for long-duration stratospheric missions, where real-time data access is critical for mission success.

A comparison of the limiting magnitudes of the two main sensors, the PCO and IDS cameras, was carried out, and detailed calculations demonstrated that both systems are capable of star detection. In addition, a comprehensive analysis of the captured data was conducted, including delay analysis, thermal behavior, and sensor performance comparison. A key takeaway from this mission is that non-weatherized microSD cards proved more advantageous than weatherized alternatives, as the internal payload temperatures supported the operation of standard microSD cards. These cards offer faster write speeds at a lower cost, making them more suitable for future missions.

5.7.1 Future Work

Future work will focus on further post-processing of the acquired data. For future stratospheric missions, uplink capabilities will be explored in addition to the downlink, allowing us to make real-time adjustments to the onboard software based on the downlink data. In addition, an analysis will be performed to determine which RSOs were uniquely detected by Sub-payload 1 and 2 and which were detected by both systems.

6 Conclusion

In conclusion, this thesis addresses the critical and growing challenge associated with SSA as satellite launches increase rapidly, leading to a significant increase in RSOs within near-Earth space. The surge in RSOs highlights the necessity of effective monitoring and detection techniques to prevent collisions and enhance SSA. While optical imagery from spacecraft and ground-based telescopes plays a key role in RSO detection, the scarcity of publicly accessible datasets has constrained the development of SSA applications. In response, this dissertation introduces an internally curated dataset comprising annotated RSO images captured from a low-resolution, wide-field-of-view imager deployed on a stratospheric balloon.

In Chapter 3, a comparative analysis of four RSO detection techniques are described: Adjacent Frame Differencing (AFD), Median Frame Differencing (MFD), Proximity Filtering and Tracking (PFT), and Streak Detection (SD). Each technique exhibits distinct strengths suited to specific operational needs. MFD is optimal for onboard processing and FPGA implementation due to its effective balance between noise reduction and detection accuracy. PFT is the most effective for real-time processing, offering robust filtering of static objects while consistently tracking dynamic RSOs. Streak Detection (SD), although promising for minimizing false negatives and adapting to varying light conditions, is less effective for detecting faint RSOs. The algorithms demonstrated high precision scores ranging from 73% to 100% and F1 scores up to 82%, highlighting their practical applicability.The integration of these techniques enables comprehensive spatial detection, enhancing the prediction of RSO trajectories, which is crucial for collision prevention and safeguarding vital space assets. As RSO proliferates, this research underscores the urgent need to democratize RSO detection methods to protect Earth's orbital environment in the long term. The findings offer valuable insights into selecting the most appropriate detection techniques based on application requirements, thereby contributing to the sustainability of space operations through expanded access to reliable RSO detection and tracking technologies. The results emphasize the versatility of proximity filtering and tracking for real-time onboard processing, demonstrating its

potential for broader adoption in future space operations. I developed and validated the Streak Detection algorithm, carefully selecting image sequences based on their complexity after a thorough examination of the RSONAR dataset and implementing evaluation metrics to ensure a rigorous comparison.

The chapter 3 evaluates the 2022 RSONAR Star Tracker's (ST) capability in both attitude determination and RSO imaging, offering an innovative approach to overcoming the limitations of traditional ground-based and space-based SSA systems. Over a 157-minute imaging period, more than 500 unique RSOs were identified, demonstrating the ST's effectiveness in capturing RSOs while retrieving attitude information. The performance of three detection methods— AFD, MFD, and PFT—was assessed, resulting in the detection of 18,566, 9,194, and 22,036 RSOs, respectively. Additionally, 387 RSO streaks were identified using image stacking and the Streak Detection algorithm. Photometric and astrometric evaluations using FWHM, SNR, and Astrometry.net were conducted to assess both star and RSO imaging performance.The findings highlight the viability of using a dual-purpose Star Tracker for SSA during stratospheric flights, offering a cost-effective alternative to traditional SSA systems. The dataset's high density and diversity of RSOs provide valuable insights for developing and validating advanced SSA techniques. This research emphasizes the potential of stratospheric platforms in supporting space monitoring technologies. This enriched dataset aims to further advance RSO detection and SSA capabilities.I analyzed the RSONAR dataset, extending the annotations for RSOs presented in this chapter and characterizing them based on SNR, FWHM, angular velocity, and magnitude under varying lighting conditions.

Chapter 4 offers a comprehensive analysis of RSO streaks captured during the RSONAR flight, making significant contributions to SSA. The study involved a detailed examination of 544 manually annotated streaks from 66,049 images, providing essential insights into RSO streak behavior, such as length, orientation, SNR, and FWHM, which are vital for improving RSO identification.This chapter also addresses data limitations in SSA by providing 544 RSO streak annotations as ground truth for algorithm development and validation. These annotations will be made publicly available to support the SSA research community. A critical aspect of this chapter was the

benchmarking of streak detection algorithms, comparing the ASTRiDE algorithm with the newly developed SD algorithm. This analysis identified the strengths and weaknesses of each algorithm, guiding the development of more accurate detection methods for SSA applications.The integration of image quality metrics like SSIM, PSNR, and LPIPS further enhanced the understanding of the RSONAR dataset, ensuring the robustness of the developed algorithms under various observational conditions. The chapter's contributions provide valuable data-driven insights and resources for advancing SSA.

In chapter 5 introduces the Resident Space Object Near-space Astrometric Research II (RSONAR II) mission, launched in August 2023, successfully demonstrated the capabilities of a next-generation dual-purpose star tracker system integrated into a 4U CubeSat-inspired platform. The mission aimed to enhance the SSA dataset and validate improved software capabilities in a sub-orbital environment, utilizing a stratospheric balloon platform as a cost-effective alternative to traditional space-based missions. RSONAR II featured two imaging systems, Sub-payload 1 and Sub-payload 2. Sub-payload 1 enabled in-flight resolution adjustments and real-time downlink communication, facilitating continuous health monitoring and data acquisition. This system's real-time imaging adjustments allowed for the evaluation of various configurations for RSO imaging, contributing to a reliable dataset. Sub-payload 2 focused on real-time attitude determination and RSO detection using cost-effective hardware. The mission also included a detailed comparison of the optical performance of the two imaging systems, demonstrating their capability for star detection. A key achievement of this mission was the successful real-time image downlink, crucial for monitoring payload performance throughout the flight. The findings also highlighted the advantages of non-weatherized microSD cards, offering faster write speeds and cost efficiency. The mission's outcomes provide valuable insights for future SSA missions, particularly in the context of CubeSat launches to Low Earth Orbit (LEO). I played a key role in the design and implementation of various aspects of the RSONAR II mission, including the development of an autonomous image acquisition system, performance comparisons between different payloads, thermal profiling, and post-processing data calibration. These contributions were critical to the mission's success and will

inform future advancements in SSA technology.

The key contributions of this study include the development and validation of multiple RSO detection algorithms achieving F1 scores between 68% and 88%. The feasibility of dual-purpose star trackers for SSA was demonstrated by leveraging their wide field of view to detect and characterize RSOs, validated through the analysis of over 27,000 images, which provided insights into the astrometric and photometric properties of these objects. Additionally, 544 RSO streaks were characterized from the RSONAR dataset, with detailed analysis of parameters such as length, SNR, and orientation, contributing to a publicly available resource for the SSA community. The development and testing of RSONAR II, a next-generation imaging system, further enhanced the study, capturing over 65,000 images with improved optical performance and resolution, which were compared to subsystem. Lastly, this research advanced the understanding of stratospheric platforms as an intermediate observational tool between ground-based and space-based systems, providing an effective and reliable alternative for capturing high-quality RSO imagery.

6.1 Future Work

This dissertation has laid the groundwork for further advancements in Space Situational Awareness (SSA), presenting several opportunities for extending its contributions to the broader SSA community.

RSO Identification : RSOs detected within the RSONAR dataset need to be correlated with existing or new RSO catalog entries. While RSO identification and correlation have typically been achieved using narrow field-of-view (FOV) sensors, applying these processes to wide-FOV sensors, such as those used in the RSONAR mission, poses a significant challenge. However, this also presents a unique opportunity for improvement. Developing and validating RSO identification methods based on wide-FOV data could enhance the robustness and efficiency of future SSA systems.

Initial Orbit Determination : Initial orbits for RSOs detected within the dataset can be determined using angular data. However, traditional methods face degeneracy issues when extracting

Keplerian elements. The development of an improved Initial Orbit Determination (IOD) tool could mitigate these issues and enhance RSO identification systems. Furthermore, accurate orbit propagation and prediction rely on precise timekeeping. Both RSONAR II and its predecessor lacked dedicated, high-precision timekeeping equipment, leading to potential inaccuracies in temporal data. Incorporating resilient timekeeping units in future missions would improve the precision of orbit determination.

Multi-Site Observations : To further assess the effectiveness of stratospheric platforms for SSA, multi-site observations should be explored. Establishing ground-based systems to image the same regions of the celestial sphere observed from the stratospheric platform would allow for valuable comparisons between astrometric and photometric properties of RSOs. Additionally, multi-site data could be used to refine orbit determination and contribute to a more comprehensive understanding of uncatalogued RSOs.

Photometric Characterization : Future research should focus on photometric characterization of RSOs within the RSONAR dataset. Generating light curves, which measure RSO brightness over time, could be instrumental in determining an RSO's attitude, shape, and stability. This photometric analysis would offer a richer dimension to RSO characterization, further enhancing the dataset's value for future SSA research and applications.

Advanced Imaging Systems : Upcoming stratospheric missions should consider integrating advanced imaging technologies, such as multispectral, near-infrared, and neuromorphic cameras. These systems can capture different wavelengths and detect faster RSO movements, improving upon the dataset collected in previous missions.

AI-Based Detection Algorithms : AI-based detection algorithms, such as U-net and Convolutional Neural Networks (CNNs), hold significant promise as alternatives to traditional detection methods. However, the development of AI-based systems is often limited by the availability of high-quality annotated data. Leveraging the existing RSO annotations from this dissertation could address this limitation and potentially show improvement via performance metrics. Moreover, optimizing these algorithms for onboard use, especially utilizing FPGA fabrics, could enable real-time

RSO detection during future missions hindering image acquisition.

Open-Source Data and Ground System Server : To support broader SSA research, an open-source ground system server should be established. This platform would allow researchers to aggregate, process, and access SSA datasets from both stratospheric flights and ground-based campaigns. A web-based interface would enable users to upload datasets, analyze them using the SSA algorithms presented in this dissertation, and refine annotations through a graphical interface. By automating much of the annotation process, this platform could significantly reduce the time required for data labeling, while also empowering a wide range of users—including amateur researchers—to contribute to SSA research. Algorithms such as Proximity Filtering and Tracking (PFT) could serve as the backend for this annotation system, streamlining the development of new SSA applications.

Bibliography

[1] ESA Space Debris Office, "ESA's Annual Space Environment Report," LOG GEN-DB-LOG-00288-OPS-SD, European Space Agency, July 2024. Final version.

[2] H. Wright, A. Williams, A. Wilkinson, L. Harper, K. Savin, and A. M. Wilson, "An analysis of publicly available microgravity crystallization data: Emergent themes across crystal types," *Crystal Growth & Design*, vol. 22, no. 12, pp. 6849–6851, 2022.

[3] European Space Agency, "Space debris by the numbers." `https://www.esa.int/Space_Safety/Space_Debris/Space_debris_by_the_numbers` (accessed on 5 October 2023).

[4] J. McDowell, "General catalog of artificial space objects," 2020.

[5] CelesTrak, "Satcat: Satellite catalog search," 2024.

[6] A. Jones, "Can china challenge spacex's starlink? new spaceports and rockets will launch the qianfan megaconstellation," *IEEE Spectrum*, August 2024. News article. Accessed: 2024-09-16.

[7] LeoLabs Data Analytics Team, "What's up in leo? insights and analysis from 2022," January 2023. Accessed: 2024-09-16.

[8] N. L. Johnson, "The historical effectiveness of space debris mitigation measures," in *56th International Astronautical Congress of the International Astronautical Federation, the International Academy of Astronautics, and the International Institute of Space Law*, pp. B6–3.

[9] P. Wegener, J. Bendisch, and H. Krag, "Model population upgrades based on recent observations," in *Space Debris*, vol. 473, pp. 327–332, 2001.

[10] European Space Agency, "Fragmentation Event Database Statistics." https://fragmentation.esoc.esa.int/home/statistics (accessed 4 April 2024).

[11] D. Cerutti-Maori, C. Carloni, J. Rosebrock, and J. Siminski, "Observation of cosmos-1408 debris cloud with the tracking and imaging radar system," in *Proc. 2nd NEO and Debris Detection Conference*, 2023.

[12] P. Ravi, C. Frueh, and T. Schildknecht, "Investigation of three recent atlas v centaur upper stage fragmentation events," in *8th European Conference on Space Debris*, vol. 8, 2021.

[13] V. Braun, A. Horstmann, S. Lemmens, C. Wiedemann, and L. Böttcher, "Recent developments in space debris environment modelling, verification and validation with master," in *8th European Conference on Space Debris*, p. 18, ESA Space Debris Office Darmstadt, Germany, 2021.

[14] H. Krag, M. Serrano, V. Braun, P. Kuchynka, M. Catania, J. Siminski, M. Schimmerohn, X. Marc, D. Kuijper, I. Shurmer, *et al.*, "A 1 cm space debris impact onto the sentinel-1a solar array," *Acta Astronautica*, vol. 137, pp. 434–443, 2017.

[15] K. Noon, "Thousands of satellites are polluting australian skies and threatening ancient knowledge," April 2022. Australian National University.

[16] M. Kocifaj, F. Kundracik, J. C. Barentine, and S. Bará, "The proliferation of space objects is a rapidly increasing source of artificial night sky brightness," *Monthly Notices of the Royal Astronomical Society: Letters*, vol. 504, no. 1, pp. L40–L44, 2021.

[17] P. Martinez, "The development and implementation of international un guidelines for the long-term sustainability of outer space activities," *Advances in Space Research*, vol. 72, no. 7, pp. 2597–2606, 2023.

[18] V. Suthakar, A. A. Sanvido, R. Qashoa, and R. S. Lee, "Comparative analysis of resident space object (rso) detection methods," *Sensors*, vol. 23, no. 24, p. 9668, 2023.

[19] H. Hakima, B. Stoute, M. Fricker, J. Williams, P. Boone, M. Rey, A. Dupuis, S. Turbide, L. Desbiens, L. Marchese, P. Topart, and A. Bergeron, "Space-object identification satellite

(soisat) mission," in *Proceedings of the Advanced Maui Optical and Space Surveillance Technologies Conference (AMOS)*, (Maui, HI, USA).

[20] Y. Nakajima, T. Sasaki, N. Okada, and T. Yamamoto, "Development of lidar measurement simulator considering target surface reflection," in *Proceedings of the 8th European Conference on Space Debris*, vol. 8, (Darmstadt, Germany).

[21] L. Fuller, R. Karl, B. Anderson, and M. Lee-Roller, "Development of a versatile lidar point cloud simulation testbed for advanced rso algorithms," in *Proceedings of the Advanced Maui Optical and Space Surveillance Technologies Conference (AMOS)*, (Maui, HI, USA).

[22] S. Piedra, S. Rivo, and C. Morollón, "Orbit determination of space debris using radar, laser and optical measurements," in *Proceedings of the 2nd NEO and Debris Detection Conference*, (Darmstadt, Germany).

[23] L. Facchini, M. F. Montaruli, P. D. Lizia, M. Massari, G. Pupillo, and G. Bianchi, "Resident space object track reconstruction using a multireceiver radar system," in *Proceedings of the 8th European Conference on Space Debris*, vol. 8, (Darmstadt, Germany).

[24] H. Ma, "Initial orbits of leo objects using radar observations," in *Proceedings of the 8th European Conference on Space Debris*, vol. 8, (Darmstadt, Germany).

[25] J. Ender, L. Leushacke, A. Brenner, and H. Wilden, "Radar techniques for space situational awareness," in *Proceedings of the 2011 12th International Radar Symposium (IRS)*, (Leipzig, Germany), pp. 21–26.

[26] I. N. Network, "Challenges of space-based space situational awareness." Available online: `https://www.innovationnewsnetwork.com/challenges-of-space-based-space-situational-awareness/34979/` (accessed on 5 October 2023).

[27] A. Biria and B. Marchand, "Constellation design for space-based space situational awareness applications: An analytical approach," *J. Spacecr. Rocket.*, vol. 51, pp. 545–562, 2014.

[28] S. Clemens, R. Lee, P. Harrison, and W. Soh, "Feasibility of using commercial star trackers for on-orbit resident space object detection," in *Proceedings of the Advanced Maui Optical and Space Surveillance Technologies Conference*, 2018.

[29] T. Xu, X. Yang, Z. Fu, M. Wu, and S. Gao, "A staring tracking measurement method of resident space objects based on the star tacker," *Photonics*, vol. 10, no. 3, p. 288, 2023.

[30] D. Spiller, E. Magionami, V. Schiattarella, F. Curti, C. Facchinetti, L. Ansalone, and A. Tuozzi, "On-orbit recognition of resident space objects by using star trackers," *Acta Astronaut.*, vol. 177, pp. 478–496, 2020.

[31] S. Dave, R. Clark, C. Gabriel, and R. Lee, "Machine learning implementation for in-orbit rso orbit estimation using star tracker cameras," in *Proceedings of the Advanced Maui Optical and Space Surveillance Technologies Conference (AMOS)*, (Online), p. 15.

[32] S. Dave, R. Clark, and R. Lee, "Rsonet: An image-processing framework for a dual-purpose star tracker as an opportunistic space surveillance sensor," *Sensors*, vol. 22, p. 5688, 2022.

[33] K. Ragland and P. Tharcis, "A survey on object detection, classification and tracking methods," *Int. J. Eng. Res. Technol.*, vol. 3, pp. 622–628, 2014.

[34] L. Liu, W. Ouyang, X. Wang, P. Fieguth, J. Chen, X. Liu, and M. Pietikäinen, "Deep learning for generic object detection: A survey," *arXiv*, 2019. arXiv:1809.02165.

[35] Z. Zou, K. Chen, Z. Shi, Y. Guo, and J. Ye, "Object detection in 20 years: A survey," *arXiv*, 2023. arXiv:1905.05055.

[36] X. Wu, D. Sahoo, and S. C. H. Hoi, "Recent advances in deep learning for object detection," *arXiv*, 2019. arXiv:1908.03673.

[37] F. Massimi, P. Ferrara, and F. Benedetto, "Deep learning methods for space situational awareness in mega-constellations satellite-based internet of things networks," *Sensors*, vol. 23, p. 124, 2023.

[38] N. Cziranka-Crooks, T. Hrynyk, D. D. Balam, V. Abbasi, L. Scott, and S. Thorsteinson, "Neossat: Operational and scientific evolution of canada's resilient space telescope," in *Proceedings of the 2nd NEO and Debris Detection Conference*, (Darmstadt, Germany).

[39] L. Cogger, A. Howarth, A. Yau, A. White, G. Enno, T. Trondsen, D. Asquin, B. Gordon, P. Marchand, D. Ng, G. Burley, M. Lessard, and B. Sadler, "Fast auroral imager (fai) for the e-pop mission," *Space Sci. Rev.*, vol. 189, pp. 15–25, 2015.

[40] K. Abercromby, P. Seitzer, H. Cowardin, E. Barker, and M. Matney, "Michigan orbital debris survey telescope observations of the geosynchronous orbital debris environment observing years: 2007–2009," tech. rep., NASA Technical Report; National Aeronautics and Space Administration, Johnson Space Center, Houston, TX, USA, 2011.

[41] R. Qashoa and R. Lee, "Classification of low earth orbit (leo) resident space objects' (rso) light curves using a support vector machine (svm) and long short-term memory (lstm)," *Sensors*, vol. 23, p. 6539, 2023.

[42] R. Muthukrishnan and M. Radha, "Edge detection techniques for image segmentation," *Int. J. Comput. Sci. Inf. Technol.*, vol. 3, pp. 259–267, 2011.

[43] D. Lang, D. W. Hogg, K. Mierle, M. Blanton, and S. Roweis, "Astrometry.net: Blind astrometric calibration of arbitrary astronomical images," *Astron. J.*, vol. 139, p. 1782, 2010.

[44] R. Sara and V. Cvrcek, "Faint streak detection with certificate by adaptive multi-level bayesian inference," in *Proceedings of the 7th European Conference on Space Debris*, (Darmstadt, Germany).

[45] M. Musallam, K. Ismaeil, O. Oyedotun, M. Perez, M. Poucet, and D. Aouada, "Spark: Spacecraft recognition leveraging knowledge of space environment," *arXiv*, 2021. arXiv:2104.05978.

[46] G. Meng, Z. Jiang, Z. Liu, H. Zhang, and D. Zhao, "Full-viewpoint 3d space object recognition based on kernel locality preserving projections," *Chin. J. Aeronaut.*, vol. 23, pp. 563–572, 2010.

[47] S. Afshar, A. P. Nicholson, A. Van Schaik, and G. Cohen, "Event-based object detection and tracking for space situational awareness," *IEEE Sensors Journal*, vol. 20, no. 24, pp. 15117–15132, 2020.

[48] Z. Chen, Y. Yang, A. Bettens, Y. Eun, and X. Wu, "A simulation-augmented benchmarking framework for automatic rso streak detection in single-frame space images," *arXiv*, 2023. arXiv:2305.00412.

[49] A. V. Dentamaro, P. D. Dao, and K. R. Knobel, "Test of neural network techniques using simulated dual-band data of leo satellites," in *Proceedings of the Advanced Maui Optical and Space Surveillance Technologies Conference (AMOS)*, (Maui, HI, USA).

[50] A. M. Antón, K. Mcnally, D. Ramirez, D. Smith, and J. Dick, "Artificial intelligence for space resident objects characterisation with lightcurves," in *Proceedings of the 8th European Conference on Space Debris*, (Online).

[51] M. Cordts, M. Omran, S. Ramos, T. Rehfeld, M. Enzweiler, R. Benenson, U. Franke, S. Roth, and B. Schiele, "The cityscapes dataset for semantic urban scene understanding," *arXiv*, 2016. arXiv:1604.01685.

[52] "pco.panda 4.2 Ultra Compact SCMOS Camera; Excelitas PCO GmbH. pp. 1–7." `https://www.excelitas.com/product-category/pco?referer=pco`.

[53] Carl Zeiss AG, "Zeiss dimension 2/25," 2018. Available online: `https://www.zeiss.com/content/dam/consumer-products/downloads/industrial-lenses/datasheets/en/dimension-lenses/datasheet-zeiss-dimension-225.pdf` (accessed on 6 October 2023).

[54] P. Kunalakantha, A. Baires, S. Dave, R. Clark, G. Chianelli, and R. Lee, "Stratospheric night sky imaging payload for space situational awareness (ssa)," *Sensors*, vol. 23, p. 6595, 2023.

[55] Strato-Science, "Strato-science 2022 campaign." Available online: https://www.asc-csa.gc.ca/eng/sciences/balloons/campaign-2022.asp (accessed on 6 October 2023).

[56] K. A. Collins, J. F. Kielkopf, K. G. Stassun, and F. V. Hessman, "Astroimagej: Image processing and photometric extraction for ultra-precise astronomical light curves," *Astron. J.*, vol. 153, p. 77, 2017.

[57] "Space situational awareness dod should evaluate how it can use commercial data report to congressional committees united states government accountability office," 2023.

[58] M. R. Ackermann, D. D. Cox, R. R. Kiziah, P. C. Zimmer, and J. T. McGraw, "A systematic examination of ground-based and space-based approaches to optical detection and tracking of artificial satellites.," tech. rep., Sandia National Lab.(SNL-NM), Albuquerque, NM (United States), 2015.

[59] S. Dave and R. Lee, "Feasibility of a virtual constellation using small aperture, wide field of view optical systems for space domain awareness and applications," in *AMOS Conference*, 2022.

[60] J. Nishimura, "Scientific ballooning in the 20th century; a historical perspective," *Advances in Space Research*, vol. 30, no. 5, pp. 1071–1085, 2002.

[61] H. Ford, L. Petro, C. Burrows, C. Ftaclas, M. Roggemann, and J. Trauger, "Artemis: a stratospheric planet finder," *Advances in Space Research*, vol. 30, no. 5, pp. 1283–1288, 2002.

[62] T. Kremic, A. F. Cheng, K. Hibbitts, E. F. Young, R. R. Ansari, M. D. Dolloff, and R. R. Landis, "Stratospheric balloons for planetary science and the balloon observation platform for

planetary science (bopps) mission summary," in *2015 IEEE Aerospace Conference*, pp. 1–10, IEEE, 2015.

[63] M. Lewis, J. Juergens, E. Aretskin-Hariton, and R. Woodruff, "Image guider subsystem analysis for the ghaps project," in *Ground-based and Airborne Instrumentation for Astronomy VII*, vol. 10702, pp. 1572–1591, SPIE, 2018.

[64] P. Maier, J. Wolf, A. Krabbe, T. Keilig, A. Pahler, S. Bougueroua, T. Müller, R. Duffard, J.-L. Ortiz, S. Klinkner, M. Lengowski, C. Krokstedt, C. Lockowandt, N. Kappelmann, B. Stelzer, K. Werner, S. Geier, C. Kalkuhl, T. Rauch, T. Schanz, J. Barnstedt, L. Conti, L. Hanke, and M. Kaźmierczak-Barthel, "Stratospheric balloons as a platform for the next large far infrared observatory," 2022.

[65] J. McKaig, T. Caro, A. Hyer, E. D. Talburt, S. Verma, K. Cui, A.-S. Boguraev, M. Heit, A. Johnson, E. Johnson, *et al.*, "A high-altitude balloon platform for space life sciences education," *Gravitational and Space Research*, vol. 7, no. 1, pp. 62–69, 2019.

[66] W. V. Jones, "Evolution of scientific ballooning and its impact on astrophysics research," *Advances in Space Research*, vol. 53, no. 10, pp. 1405–1414, 2014.

[67] R. Qashoa, V. Suthakar, G. Chianelli, P. Kunalakantha, and R. S. Lee, "Technology demonstration of space situational awareness (ssa) mission on stratospheric balloon platform," *Remote Sensing*, vol. 16, no. 5, p. 749, 2024.

[68] L. Bradley, B. SipHocz, T. Robitaille, E. Tollerud, Z. Vin´icius, C. Deil, K. Barbary, T. J. Wilson, I. Busko, H. M. Günther, *et al.*, "astropy/photutils: 1.0. 2," *Zenodo*, 2020.

[69] H. P. Gavin, "The levenberg-marquardt algorithm for nonlinear least squares curve-fitting problems," *Department of civil and environmental engineering, Duke University*, vol. 19, 2019.

[70] Y.-J. Zhang, "Camera calibration," in *3-D Computer Vision: Principles, Algorithms and Applications*, pp. 37–65, Springer, 2023.

[71] D. Lang, D. W. Hogg, K. Mierle, M. Blanton, and S. Roweis, "Astrometry. net: Blind astrometric calibration of arbitrary astronomical images," *The astronomical journal*, vol. 139, no. 5, p. 1782, 2010.

[72] J. R. Shell, "Optimizing orbital debris monitoring with optical telescopes," in *Advanced Maui Optical and Space Surveillance Technologies Conference*, p. E42, 2010.

[73] G. Bradski, A. Kaehler, *et al.*, "Opencv," *Dr. Dobb's journal of software tools*, vol. 3, no. 2, 2000.

[74] A. Elhakiem, T. Ghoniemy, and G. Salama, "Streak detection in astronomical images based on convolutional neural network," in *International Conference on Aerospace Sciences and Aviation Technology*, vol. 20, pp. 1–9, The Military Technical College, 2023.

[75] O. Parisot and M. Jaziri, "Impact of satellites streaks for observational astronomy: a study on data captured during one year from luxembourg greater region,"

[76] W. A. Dawson, M. D. Schneider, and C. Kamath, "Blind detection of ultra-faint streaks with a maximum likelihood method," *arXiv preprint arXiv:1609.07158*, 2016.

[77] P. Zimmer, J. T. McGraw, and M. R. Ackermann, "Real-time optical space situational awareness of low-earth orbit with small telescopes," in *Advanced Maui Optical and Space Surveillance Technologies Conference*, 2018.

[78] M. Cegarra Polo, T. Yanagisawa, and H. Kurosaki, "Real-time processing pipeline for automatic streak detection in astronomical images implemented in a multi-gpu system," *Publications of the Astronomical Society of Japan*, vol. 74, no. 4, pp. 777–790, 2022.

[79] R. Haussmann, P. Wagner, and T. Clausen, "Streak detection of space debris by a passive optical sensor," in *Proc. of 8th European conference on space debris*, 2021.

[80] H. Oda, H. Kurosaki, T. Yanagisawa, and M. Tagawa, "Optical observation, image-processing, and detection of space debris in geosynchronous earth orbit," *40th COSPAR Scientific Assembly*, vol. 40, pp. PEDAS–1, 2014.

[81] R. Danescu, A. Ciurte, and V. Turcu, "A low cost automatic detection and ranging system for space surveillance in the medium earth orbit region and beyond," *Sensors*, vol. 14, no. 2, pp. 2703–2731, 2014.

[82] H. N. Do, T.-J. Chin, N. Moretti, M. K. Jah, and M. Tetlow, "Robust foreground segmentation and image registration for optical detection of geo objects," *Advances in Space Research*, vol. 64, no. 3, pp. 733–746, 2019.

[83] "Nasa satellite streak watcher project." `https://www.anecdata.org/explore?project_id=687`, n.d. [Online; accessed 19-August-2024].

[84] S. Kruk, P. Garc´ia-Mart´in, M. Popescu, B. Aussel, S. Dillmann, M. E. Perks, T. Lund, B. Mer´in, R. Thomson, S. Karadag, *et al.*, "The impact of satellite trails on hubble space telescope observations," *Nature Astronomy*, vol. 7, no. 3, pp. 262–268, 2023.

[85] B. Chen, D. Liu, T.-J. Chin, M. Rutten, D. Derksen, M. Martens, M. von Looz, G. Lecuyer, and D. Izzo, "Spot the geo satellites: From dataset to kelvins spotgeo challenge," in *Proceedings of the IEEE/CVF Conference on Computer Vision and Pattern Recognition (CVPR) Workshops*, pp. 2086–2094, June 2021.

[86] Y. Dai, T. Zheng, C. Xue, and L. Zhou, "Effective multi-frame optical detection algorithm for geo space objects," *Applied Sciences*, vol. 12, no. 9, 2022.

[87] R. Abay and K. Gupta, "Geo-fpn: A convolutional neural network for detecting geo and near-geo space objects from optical images," in *Proceedings of the 8th European Conference on Space Debris (virtual)*, 2021.

[88] J. T. VanderPlas, "Understanding the lomb–scargle periodogram," *The Astrophysical Journal Supplement Series*, vol. 236, p. 16, may 2018.

[89] K. P. Sinaga and M.-S. Yang, "Unsupervised k-means clustering algorithm," *IEEE access*, vol. 8, pp. 80716–80727, 2020.

[90] K. R. Shahapure and C. Nicholas, "Cluster quality analysis using silhouette score," in *2020 IEEE 7th international conference on data science and advanced analytics (DSAA)*, pp. 747–748, IEEE, 2020.

[91] U. Sara, M. Akter, and M. S. Uddin, "Image quality assessment through fsim, ssim, mse and psnr—a comparative study," *Journal of Computer and Communications*, vol. 7, no. 3, pp. 8–18, 2019.

[92] R. Zhang, P. Isola, A. A. Efros, E. Shechtman, and O. Wang, "The unreasonable effectiveness of deep features as a perceptual metric," in *Proceedings of the IEEE conference on computer vision and pattern recognition*, pp. 586–595, 2018.

[93] D.-W. Kim, "Astride: Automated streak detection for astronomical images," *Astrophysics Source Code Library*, pp. ascl–1605, 2016.

[94] C. Jeffries and R. Acuña, "Detection of streaks in astronomical images using machine learning," *Journal of Artificial Intelligence and Technology*, vol. 4, no. 1, pp. 1–8, 2024.

[95] B. Lin, L. Zhong, S. Zhuge, X. Yang, Y. Yang, K. Wang, and X. Zhang, "A new pattern for detection of streak-like space target from single optical images," *IEEE Transactions on Geoscience and Remote Sensing*, vol. 60, pp. 1–13, 2021.

[96] P. Duarte, P. Gordo, N. Peixinho, R. Melicio, D. Valério, R. Gafeira, *et al.*, "Space surveillance payload camera breadboard: Star tracking and debris detection algorithms," *Advances in Space Research*, vol. 72, no. 10, pp. 4215–4228, 2023.

[97] G. Chianelli, P. Kunalakantha, M. Myhre, and R. S. K. Lee, "A dual-purpose camera for attitude determination and resident space object detection on a stratospheric balloon," *Sensors*, vol. 24, no. 1, 2024.

[98] "United Nations Office for Outer Space Affairs. Convention on Registration of Objects Launched into Outer Space," 1974. https://www.unoosa.org/oosa/en/ourwork/spacelaw/treaties/registration-convention.html.

[99] N. Johnson, "The Collision of Iridium 33 and Cosmos 2251: The Shape of Things to Come," in *60th International Astronautical Congress, Daejeon, Republic of Korea*, 2009. https://ntrs.nasa.gov/citations/20100002023.

[100] "Astromaterials Research Exploration Science. NASA Orbital Debris Program Office." https://orbitaldebris.jsc.nasa.gov/faq/.

[101] "Space Based Space Surveillance. Space Operations Command (SpOC)." https://www.spoc.spaceforce.mil/About-Us/Fact-Sheets/Display/Article/2381700/space-based-space-surveillance.

[102] "AURICAM Monitoring Camera. Sodern." https://sodern.com/wp-content/uploads/2021/12/Auricam.pdf.

[103] R. J. Oelkers and K. G. Stassun, "Precision Light Curves from TESS Full-frame Images: A Different Imaging Approach," *The Astronomical Journal*, vol. 156, p. 132, 2018.

[104] "Strato-Science 2023 campaign. Canadian Space Agency." https://www.asc-csa.gc.ca/eng/sciences/balloons/campaign-2023.asp.

[105] R. Clark, Y. Fu, S. Dave, and R. Lee, "Simulation of RSO images for space situation awareness (SSA) using parallel processing," *Sensors*, vol. 21, no. 23, 2021.

[106] "IDS UI-3370CP Rev. 2 Camera. IDS Imaging Inc. Obersulm, Gernmany.." https://en.ids-imaging.com/store/ui-3370cp-rev-2.html.

[107] "Telephoto Lens for Raspberry Pi HQ Camera. Adafruit Industries." https://www.adafruit.com/product/4562.

[108] "PYNQ-Z1 Reference Manual. Digilent." https://digilent.com/reference/programmable-logic/pynq-z1/reference-manual?redirect=1.

[109] "Datasheet MicroSD Card 3TE4 Series. Innodisk. 2021, pp. 1–2." https://www.innodisk.com/en/products/flash-storage/sd-card-and-microsd-card/microsd-card-3te4.

[110] "A Guide to Speed Classes for SD and microSD Cards. Kingston Technology." https://www.kingston.com/en/blog/personal-storage/memory-card-speed-classes.

[111] F. F. Batin, R. A. Bautista, R.-A. Dela Cruz, J. Kalaw, F. K. Martinez, and P. Tucio, "Bortle scale: A way to assess and monitor the urban nightsky," 11 2021. https://www.researchgate.net/publication/360538981_Bortle_scale_A_way_to_assess_and_monitor_the_urban_nightsky.

[112] "IRAF zscale Scaling Algorithm. Center for Astrophysics." https://js9.si.edu/js9/plugins/help/scalecontrols.html.

[113] P. B. Stetson, "Daophot: A computer program for crowded-field stellar photometry," *Publications of the Astronomical Society of the Pacific*, vol. 99, p. 191, mar 1987.

[114] M. A. C. Perryman, L. Lindegren, J. Kovalevsky, E. Hoeg, U. Bastian, P. L. Bernacca, M. Crézé, F. Donati, M. Grenon, M. Grewing, F. van Leeuwen, H. van der Marel, F. Mignard, C. A. Murray, R. S. Le Poole, H. Schrijver, C. Turon, F. Arenou, M. Froeschlé, and C. S. Petersen, "The HIPPARCOS Catalogue," , vol. 323, pp. L49–L52, July 1997.

[115] Ochsenbein, F., Bauer, P., and Marcout, J., "The vizier database of astronomical catalogues," *Astron. Astrophys. Suppl. Ser.*, vol. 143, no. 1, pp. 23–32, 2000.

[116] "The Life Cycle of Celestial Objects Exhibit. McIntosh Gallery, Western University." https://www.events.westernu.ca/events/mcintosh-gallery/2023-09/opening-reception-the-life.html.